Optimization of Femtosecond Laser Plasma Kα Sources

Dissertation

zur Erlangung des akademischen Grades
doctor rerum naturalium (Dr. rer. nat.)

vorgelegt dem Rat der Physikalisch-Astronomischen Fakultät der
Friedrich-Schiller-Universität Jena

von Diplom-Physiker Christian Reich
geboren am 22. April 1968 in Berlin

Gutachter:

1. Prof. Dr. Eckhart Förster

2. Prof. Dr. Thomas Elsässer

3. Prof. Dr. Christoph Rose-Petruck

Tag der letzten Rigorosumsprüfung: 8. Januar 2003

Tag der öffentliche Verteidigung: 21. Januar 2003

Zusammenfassung

In der vorliegenden Arbeit wurden drei Eigenschaften der Kα-Röntgenstrahlung aus laserproduzierten Plasmen untersucht: die Kα-Ausbeute, die Quellgröße und die Dauer des Röntgenpulses. Dazu wurden ein neues Simualtionsmodell entwickelt und zweidimensionale Abbildungen der Kα-Emission von zwei Targetseiten gemacht.

Für die numerischen Studien wurde ein neues Monte-Carlo-Simulationsprogramm entwickelt, das die Streuung eines Elektronenstrahls in einem Festkörper berechnet. Der Code ermöglicht es erstmalig, für jede Targetseite die zeitliche und räumliche Struktur der Kα-Emission zu simulieren. Er wurde mit einem existierenden $1\frac{1}{2}$D Particel-In-Cell-Code zur Simulation der Wechselwirkung eines Laserstrahls mit einem Plasma kombiniert. Dieser Code liefert die Zeit- und Energieverteilung der vom Laser erzeugten heißen Elektronen.

Experimentell wurden zweidimensionale, vergrößerte Abbildungen der Kα-Emission von Titantargets aufgenommen, wobei toroidal gebogene Si(311)-Kristalle als abbildende Optik verwendet wurden. Für die experimentellen Bedingungen (Vergrösserung: 7, Auflösung: 6 μm, Azimuthfehler: 0.9°) wurde der Einfluß der Aberrationen an einer Röntgenröhre, am laserproduzierten Plasma und mittels Strahlverfolgung untersucht. Es ergab sich eine Kanteschärfe der Abbildung von ~ 10 μm. Eine gaußförmige Röntgenquelle erscheint in der Abbildung in Richtung der Dispersionsebene verbreitert, wobei die Größe der Verbreiterung von der Quellgröße abhängt. Eine Halbwertsbreite von einigen zehn Mikrometern kann in dieser Richtung nicht mehr aufgelöst werden, da die scheinbare Ausdehnung in diesem Fall überwiegend durch Aberrationen verursacht wird. Senkrecht zur Dispersionsebene bleibt die Halbwertsbreite bei der Abbildung erhalten.

Die zeitliche Struktur des Laserpulses im Experiment wurde mit einem Autokorrelator dritter Ordnung aufgenommen und das zweidimensionale Strahlprofil wurde mit einer Dynamik von 10^3 bestimmt. Zusammen mit der Kenntnis der Abbildungseigenschaften der verwendeten gebogenen Kristalle war es damit möglich, Kα-Abbildungen für Parameter zu berechnen, die denen im Experiment sehr ähnlich waren.

Die experimentelle Beobachtung, daß die Kα-Ausbeute für einen defokussierten Laser maximal wird, d.h. bei einer Laserintensität, die niedriger ist, als die maximal erreichbare, wurde in den Simulationen reproduziert. Ein analytisches Modell der Kα-Ausbeute wurde abgeleitet, das die Existenz einer optimalen Laserintensität mit der Reabsorption erzeugter

Kα-Photonen innerhalb des Targets erklärt. Mit zunehmender Laserintensität dringen die heißen Elektronen tiefer in das Target ein, und der Bruchteil der erzeugten Kα-Photonen, der die Targetoberfläche erreicht und emittiert wird, nimmt ab. Dieser Bruchteil zeigt ein universelles Verhalten bezüglich der Energie der einfallenden Elektronen normiert auf die Ionisierungsenergie der K-Schale des Targets, woraus sich eine universelle optimale Elektronentemperatur für die Konversion der Energie heißer Elektronen in Energie emittierter Kα-Photonen ergibt: $kT_{opt} = 6.4\,E_K$. Daraus folgt eine überraschend einfache Skalierung der optimalen Laserintensität mit der Ordnungszahl des Targetelements: $I_{opt} \propto Z^{4.4}$ [69].

Im besten Fokus ($I \approx 7 \times 10^{18}$ W/cm^2) beträgt die gemessene vertikale Halbwertsbreite der Kα-Emission $\sim$ 70 μm, was 28 mal mehr ist als die entsprechende Halbwertsbreite des Laserfokus. Durch die Streuung der heißen Elektronen im Festkörper kann nur eine Vergrößerung von $\lesssim 2$ erklärt werden. Der intensive Zentralbereich der Kα-Emission ist von einem weiten Bereich mit schwacher Emission umgeben, der einen Durchmesser von 400 μm hat. Mehr als die Hälfte der Kα-Emission stammt aus diesem Bereich. Die Halbwertsbreite der Emission ändert sich beim Defokussieren des Lasers bis zu einem Millimeter kaum. Wird der Laser stärker fokussiert, sagt das Simulationsmodell eine Zunahme der Spitzenemission voraus, die im Experiment nicht gefunden wird. Stattdessen nimmt nahe am besten Fokus die Spitzenemission sogar um einen Faktor zwei ab. Gleichzeitig ist die Gesamtausbeute, die bei größerer Defokussierung gut durch das numerische Modell beschrieben wird, um 60% größer als simuliert.

Eine Abschätzung der selbsterzeugten Felder im Experiment legt nahe, daß die intrinsischen Vorpulse des Lasersystems ein Magnetfeld erzeugen, dass einen Großteil der heißen Elektronen reflektiert. Ein Teil dieser Elektronen wird dann vom ponderomotorischen Feld des Lasers und weiteren Magnetfeldern über einen weiten Bereich der Targetoberfläche verteilt. Diese Effekte bieten eine qualitative Erklärung für die beobachtete räumliche Struktur der Kα-Emission.

Die Eindringtiefe der heißen Elektronen in das Target wurde aus der Kα-Emission von der Targetseite abgeschätzt. In diesen Messungen konnte eine Abweichung von den Vorhersagen des numerischen Modells nicht bestätigt werden. Dies könnte daran liegen, daß die selbsterzeugten Felder in diesen Messungen geringer waren, da der Laser dicht an die Targetkante fokussiert werden mußte, um ein optisch dünnes Target zu erhalten.

In einer numerischen Studie wurde die zeitliche Struktur der Kα-Pulse untersucht. Für Laserintensitäten unterhalb von 10^{16} W/cm^2 wird die Pulsdauer durch die Thermalisierungszeiten der heißen Elektronen bestimmt. Bei höheren Intensitäten dringen die Elektronen tiefer ein und die effektive Pulsdauer wird durch die Reabsorption erzeugter Kα-Photonen begrenzt. Die Halbwertsbreite der Kα-Emisson von Targetelementen von Si bis Cu, die mit einem 60 fs-Laserpuls bestrahlt werden, liegt dann zwischen hundert und hundertundachtzig Femtosekunden. Durch die langen Thermalisierungszeiten der heißesten Elektronen erfolgen die ersten 90% der Emission auf einer sehr viel längeren Zeitskala von einigen hundert Femtosekunden bis zu mehreren Picosekunden. Die oben erwähnte Abschätzung selbsterzeugter Felder läßt eine Verlängerung der Kα-Pulse erwarten. Diese beträgt weniger als 100 fs durch komplexe Elektronenbahnen in den Feldern und weniger als 1 ps durch ballistische Trajektorien, die die heißen Elektronen über eine Fläche der gemessenen Größe verteilen.

Die berechneten Halbwertsbreiten der Kα-Pulse stimmen gut mit den in Kreuzkorrelationsexperimenten gefundenen Werten überein, sind jedoch erheblich kürzer als die aus Messungen mit Schmierbildkameras. Der von einer anderen Gruppe an der Universität Jena in einem Kreuzkorrelationsexperiment gefundene zeitliche Abfall des Kα-Meßsignals wird von dem Simulationsmodell gut reproduziert [31].

Da die Studie der Kα-Emission von Volumentargets zeigte, daß diese Targets (außer für die leichtesten Elemente) relativ ungeeignet sind, um effiziente 100 fs Pulse zu erzeugen, wurde der Gebrauch von Folientargets untersucht, die von den heißesten Elektronen schnell durchquert werden. Diese Studien ergaben Designformeln für das Erzeugen von Kα-Pulsen mit wählbarer Dauer und hoher Ausbeute [69]. Angesichts der aktuellen Fortschritte in der Lasertechnologie, durch die Hochintensitätslaser mit Femtosekundenpulsdauern und hohen Repetitionsraten verfügbar werden, erscheint es als realistisch, daß in der nahen Zukunft Laserplasma-Kα-Quellen verfügbar sein werden, die hohe Photonenflüsse mit Pulsdauern $\leq$ 100 fs verbinden werden.

Contents

Introduction

Since the night when Conrad Röntgen first saw his hand's bones on a fluorescence screen [71] x rays have been one of the most important tools for revealing the inner structure of matter. Beside x-ray imaging for medical diagnosis, the study of x-ray diffraction patterns in chemistry and physics has become a major application of x rays, because it allows the structure of crystalline solids with atomic spatial resolution to be analyzed.

Processes which are determined by atomic motion, like chemical reactions and phase transitions, happen on a timescale comparable to the vibrational period of the atoms, which is typically 10^{-13} s or 100 fs [76]. The ideal tool to investigate such a process would simultaneously offer a temporal resolution smaller than this time scale *and* the ability to resolve the interatomic distances. Until recently, no such tool existed and the investigator had to choose between the femtosecond time resolution of optical spectroscopy with femtosecond lasers and the spatial resolving power of x-ray studies. The experimental method which came closest to the 'ideal tool' was time-resolved x-ray diffraction using a synchrotron radiation source. It was especially used to study biologically important processes like the photoinduced *trans-cis* isomerization of a part of the protein rhodopsin which forms the light detecting process in the human eye [64] or the binding of oxygen and carbon monoxide to myoglobin [94]. These experiments had a nanosecond time resolution which proved to be accurate for the processes under investigation, but all-optical experiments indicate that the initial structural changes, which precede the studied ones, happen much faster, within several ten or hundred femtoseconds [34, 35]. Moreover, optical measurements have revealed that femtosecond time scales are also relevant to processes in solid state physics, like the atomic rearrangement during transitions from one solid phase to another [84] and the disordering of semiconductors after strong electronic excitation by a laser pulse [85]. State-of-the-art synchrotron/streak camera setups achieve a time-resolution of about 1 ps [52].

The route to push x-ray diffraction into the femtosecond realm appeared only two decades ago with the invention of the chirped pulse amplification technique [90]. This technique has enabled the generation of laser pulses with both 'femtosecond' duration (≤ 100 fs) and intensities $\geq 10^{15}$ W/cm^2 high enough to produce characteristic x-ray radiation when the laser is focused onto a solid target. The electric field strength related to such intensities is orders of magnitude higher than the field strength binding the electrons to the nucleus of an atom. Thus, the target surface is rapidly ionized and transformed into a high density plasma which then expands with its sound speed (~ 0.5 μm/ps) into the surrounding vacuum [20]. In the interaction of the high-intensity laser pulse with the plasma, numerous novel phenomena occur like the generation of intense higher harmonics of the laser light [63], hole-boring into the plasma [67, 99], magnetic fields in the megagauss range [55, 82], emission of heavy ions with energies up to hundreds of MeV [19] and photoinduced nuclear fission [80]. A number of collective absorption mechanisms like resonance absorption [51], vacuum heating [13] and wakefield acceleration [58, 95] accelerate plasma electrons to kinetic energies of many keV or even MeV. The accelerated electrons are called 'hot electrons' because their kinetic energy is much higher than the plasma temperature. They penetrate into the solid behind the plasma where they produce both characteristic x-ray radiation and bremsstrahlung. The short time of several 10 to 100 fs in which the hot electrons lose their energy to the solid (their thermalisation time) limits the duration of the emitted Kα pulse [73]. Together with the femtosecond duration of the laser pulse, a hard x-ray pulse with a duration of several hundred femtoseconds results. This is much shorter than the x-ray emission due to the recombination of the plasma ions which lasts about 2 ps until the plasma has cooled down [61].

The processes involved in Kα generation show a complex interplay because they happen on comparable time and length scales. The lengths are several 1 to 100 μm and the times several 10 to 100 fs. To illustrate this, consider a hot electron with an energy of 50 keV, which is similar to the mean hot electron energy for a laser intensity of 5×10^{16} W/cm^2 [30], penetrating into solid Al has a stopping range of 21 μm [9]. If only minor lateral deflections would occur, the electron would penetrate to approximately that depth and maybe generate a Kα photon there. The penetration process would take 240 fs [73] and the photon would need another 70 fs to reach the target surface. The absorption length of Al for its own Kα radiation is 9 μm so that the probability that this photon reaches the surface and contributes to the Kα emission is only 10%.

In the present thesis a new simulation model was developed which takes this complex interplay into account. The model integrates two computer codes, the first one simulating the laser plasma interaction, the second one calculating the scattering of the hot electrons in the solid and the production of Kα radiation. As a whole, the model delivers the temporal and spatial structure of the Kα emission produced by a femtosecond laser pulse for any target side. Experimentally, the Kα emission was studied by taking images of the emission from two target sides. Three aspects of the emission were investigated: 1) the Kα yield, 2) the spatial structure and 3) the pulse duration.

The optimization of the yield is desirable because the Kα flux per laser shot is several orders of magnitude smaller than the x-ray flux from a single synchrotron bunch [76]. Thus, often special experimental efforts are required to achieve an x-ray diffraction pattern of sufficient quality [30]. One way to enhance the Kα yield for a given laser system is to adjust the plasma density gradient during the interaction with the laser via deliberately introduced prepulses [5, 93]. Another possibility to optimize the Kα yield is to defocus the laser to a distance where the yield shows a maximum [25, 60]. This experimental observation was reproduced by the simulation model. An analytical description of the Kα yield, derived from the simulation data, explains the existence of the yield maximum and shows how its position depends on the target element [69].

The spatial distribution of the Kα emission reflects the trajectories of the hot electrons and thus indicates the physical mechanisms which influence their dynamics. For monoenergetic electron beams the penetration behaviour into cold solids and the produced x-ray yield are well understood in the context of beam-matter interaction, x-ray tubes and electron microscopy [9, 21, 27, 39]. With the advent of laser-produced plasmas additional effects like the target preheat by the hot electrons were successfully integrated into the theoretical modelling [44, 73]. But for laser intensities $> 10^{17}$ W/cm^2 the 'classical' picture of hot electron generation and penetration regularly fails to explain the experimental observations. In particular, the hot electron penetration depth is sometimes much smaller than expected [47, 92] and the Kα source size much larger [66, 102]. The favoured explanation for these observations are self-generated electric and magnetic fields which inhibit the penetration of the electrons into the target [8] and spread them over the surface [28, 32]. The common experimental method to investigate the spatial characteristics of the Kα emission is one-dimensional x-ray shadowgraphy at a knife-edge [87]. Usually, the halfwidth of the observed emission is published [25, 98, 101]. In the present thesis the spatial structure of the emission was measured with a two-dimensional imaging technique [29], which gave a number of additional properties of the Kα emission. An estimate of the magnetic and electric fields in the experiment and how they influence the hot electron trajectories showed that these fields can qualitatively explain the observed behaviour. The penetration depth of the hot electrons is usually deduced from the Kα radiation from multilayer targets [74, 93]. In the present thesis the Kα emission from a target side perpendicular to the laser-irradiated surface was measured directly.

For the duration of the Kα pulses state-of-the-art experiments only give an upper limit in the range of several hundred femtoseconds [77, 86]. Simple estimates of the pulse duration, such as identifying it with either the laser pulse duration or the hot electron thermalisation time, are rather inaccurate as the numerical example above shows. By contrast, the new simulation model allows the temporal shape of the Kα pulse to be calculated for the first time. It was used to study the dependence of the pulse duration on laser intensity and target material, to simulate the Kα pulse shape in a recent experiment [31] and to investigate how the final goal of an x-ray pulse duration $\leq$ 100 fs can be achieved [69].

The following chapters of the present dissertation follow the order of the introduction. They start with the description of the simulation model in Chapter 1 and the imaging experiment in Chapter 2. Then, a seperate chapter is devoted to each of the source properties investigated: Kα yield, the spatial characteristics of the emission and pulse duration.

Chapter 1

Numerical Modelling of the Kα Emission

1.1 New Model with Temporal and Spatial Resolution

The generation of Kα radiation from fs laser-irradiated solids involves a number of processes like ionization, plasma expansion [20], several absorption mechanisms generating hot electrons [13, 51] and the scattering of these electrons in the solid [78]. Self-generated electric and magnetic fields can occur during the plasma expansion [20, 88] or by being induced by the laser pulse [14, 91].

In a simplified description which is widely used to study the Kα emission theoretically and to interpret experimental data, only the production of the hot electrons and their scattering in the solid are considered. Numerically [66, 79, 93], the laser-plasma interaction is usually simulated with a Particle-In-Cell (PIC) code[1] which can calculate how the absorbed laser energy is distributed over the accelerated plasma electrons and when the hot electrons are generated. The plasma density profile for the PIC simulation can be provided by a hydrodynamic simulation of the plasma expansion or by measurements. A Monte Carlo (MC) code[2] is used to calculate the scattering of the hot electrons in the solid and the production of x-rays. Both codes are coupled by using the energy distribution of the hot electrons calculated by the PIC code as an input for the Monte Carlo calculations. Alternatively, the PIC code can be omitted and replaced by a scaling law for the hot electron temperature [25, 65], e.g. the one given by Beg et al. [6].

The PIC code for the simulation of the laser absorption is usually $1\frac{1}{2}$-dimensional with one space and two velocity components (e.g. the code EUTERPE by Bonnaud [11]). Thus,

---

[1] Described in Section 1.3.

[2] Described in Section 1.2.

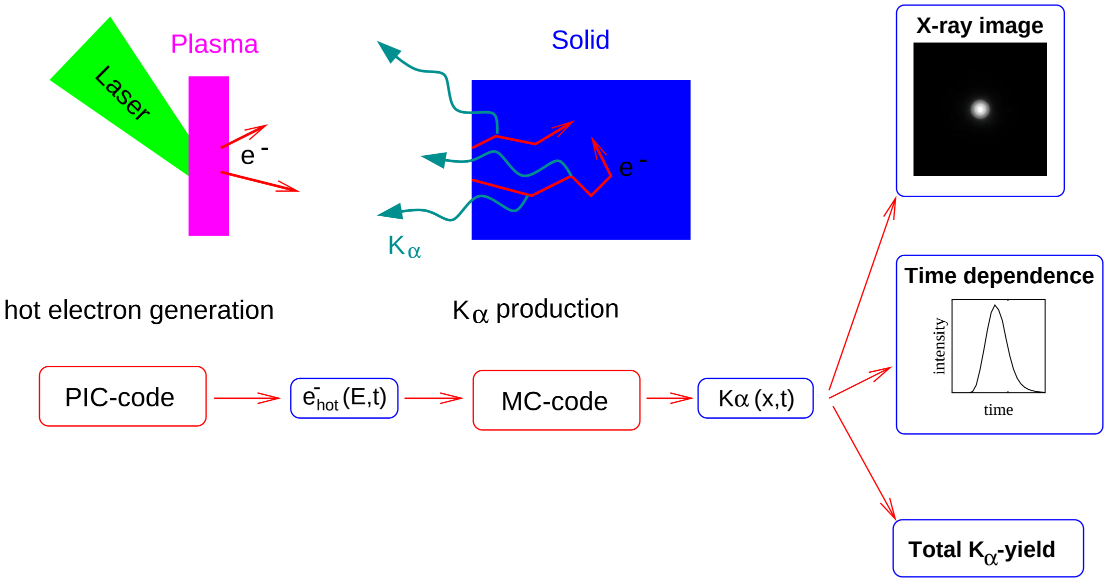

Figure 1.1: The combined PIC-Monte Carlo model for the time and space resolved calculation of Kα emission from femtosecond-laser plasmas. The PIC code simulates the generation of hot electrons during the laser plasma interaction, whereas the Monte Carlo code calculates the electron scattering in the solid behind the plasma and the generation of Kα x-rays.

no multi-dimensional effects like self-focusing of the laser [59], hole-boring into the plasma [99] or the deflection of electron trajectories by self-generated magnetic fields [55, 88] are included. Another limitation of this modelling is the assumed 'sandwich' structure of the target: a plasma with a temperature of several hundred eV ($T \approx 10^6$ K) is planely adjoined to a 'cold' solid at room temperature. In spite of the obvious limitations, this method for modelling the Kα radiation from laser plasma sources is widely used, for example to deduce the hot electron temperature from measurements of the Kα emission [66, 93].

In the present thesis a new numerical model (Fig. 1.1) is presented which is similar to the models described above, but for the first time makes it possible to calculate

1. the temporal development of the Kα emission, and
2. its spatial structure for laser intensity distributions close to experimental conditions.

Previous Monte Carlo codes, like for example ITS [43, 81], can only simulate the spatial distribution of the Kα emission for electron beams with axial symmetry, i.e. circular laser focii with homogenous intensity. Concerning the temporal structure of the emission, Rousse [73] only calculated the thermalisation time of the hot electrons with his Monte Carlo code and used it as an estimate of the pulse duration [73].

The heart of the new model is a newly developed Monte Carlo code, which calculates the three dimensional scattering of an electron beam in a solid and the Kα radiation which is generated during this process. It tracks the time going by, thus giving the temporal development of the emission, and calculates its spatial structure as seen from any side of the target. The code is combined with an existing $1\frac{1}{2}$D PIC code [36], which simulates the interaction of an oblique laser beam with the plasma and the generation of hot electrons. This code delivers not only the energy of each generated hot electron but also its generation time and entrance angle into the solid. These properties of the hot electrons are used as an input to the Monte Carlo code. Alternatively, analytical electron distributions can be used.

In the experiments described in Chapter 2 images of the Kα emission from laser-irradiated Ti targets were taken with the help of bent crystals as the imaging optics. To simulate spatially resolved Kα emissions which can be directly compared with the experimental images, post-processing is used which takes into account the laser intensity distribution in the experiment and the influences of aberrations during the imaging process via ray-tracing. The details of the post-processing are described in Section 1.4, Section 1.2 is dedicated to the Monte Carlo code, and Section 1.3 describes the PIC code.

1.2 The Monte Carlo Code

Each hot electron from a laser plasma that enters the solid behind the plasma experiences a series of individual elastic and inelastic sattering events which cannot be calculated because the exact scattering parameters are not known. Nevertheless, the macroscopic behaviour, which results from the scattering of $\sim 10^{10}$ electrons, can be reproduced by calculating a much smaller number of random electron trajectories ($\sim 10^2 - 10^4$). The calculation of these trajectories forms the inner loop of the Monte Carlo code. It is enclosed in a loop over the different electrons. The code starts with interfaces for reading electron and target data from files and ends with subroutines saving the results.

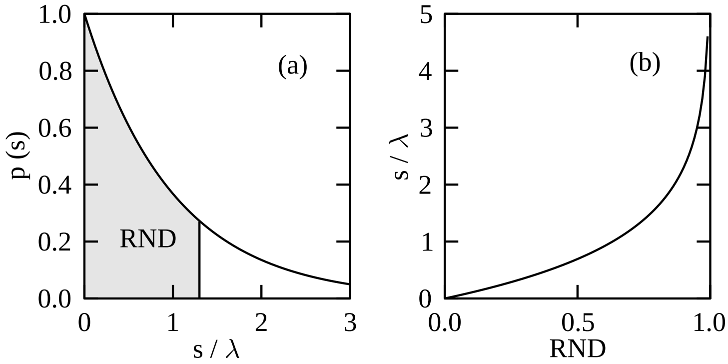

Figure 1.2: Principle of the Monte Carlo method.

1.2.1 The Monte Carlo Method

The principle of a Monte Carlo calculation is to reproduce a probability distribution resulting from a series of events by calculating stochastic results for a number of single events. For example, the probability $p(s)$, that an electron travels a distance s between two successive scattering events, is related to the mean free path λ,

$$p(s) = e^{-s/\lambda}, \tag{1.1}$$

which itself is related via the atomic density, $N_A\,\rho\,/A$, to the cross section σ (N_A: Avogadro's number, ρ: mass density, A: atomic mass),

$$\lambda = \frac{A}{N_A\,\rho\,\sigma}. \tag{1.2}$$

In a Monte Carlo calculation this relation is inverted by assigning values of s to equally distributed random numbers RND (as produced by a random number generator) in such a way that for a long enough series of RND the probability distribution $p(s)$ is reproduced. This is achieved by identifying the random numbers with the integral over $p(s)$ (Fig. 1.2a):

$$\begin{aligned} RND &= \frac{\int\limits_0^s p(s')\,ds'}{\int\limits_0^\infty p(s')\,ds'} \\ &= 1 - e^{-s/\lambda}. \end{aligned} \tag{1.3}$$

(The normalisation causes $RND \in [0;1]$.) Then, the free electron path between two successive scatters is given by (Fig. 1.2b)

$$s = -\lambda\,\ln(1 - RND). \tag{1.4}$$

The mean value of s is again λ.

1.2.2 Calculating an Electron Path

In the Monte Carlo code a single electron trajectory is described as a series of straight ‘free flights’ with an angular deflection at the end of each flight. The length of the flight and the deflection are defined by the the *elastic* scattering cross sections. *Inelastic* deflections are in the order of magnitude of the relative energy loss in the scattering, $\phi \approx \Delta E/E$, while the probability that a scattering angle ϕ occurs is reciprocal to the absolute energy loss, $p(\phi) \propto 1/\Delta E$. Thus, the influence of inelastic scattering on the direction of electron movement can be neglected. Inelastic collisions such as the generation of Bremsstrahlung, inner shell ionization of the target atoms, collective (plasmon) excitations and individual excitations of the conduction band cause the electron to lose energy and to slow down. To treat the energy losses the continuous slowing-down approximation (CSDA) [78] is applied which calculates an average rate of energy loss resulting from all types of inelastic scattering, called ‘the Bethe stopping power’.

The separation between elastic and inelastic scattering leads to a scheme for the calculation of an electron path as shown in Fig. 1.3. The first step in the loop is to calculate the distance s that the electron travels from its present position until the following elastic scattering event. Then, this pathlength enters as a linear factor into the calculation of the inelastic effects: the radiation produced on the way and the energy loss of the electron. Finally, the position and the energy of the electron are updated and its new direction, after the next elastic scattering, is calculated.

When the influence of inelastic scattering, as in this model, is neglected, the mean free path of the electron is determined by the screened Rutherford cross section

$$\sigma_E = 5.21 \times 10^{-21} \frac{Z^2}{E^2} \frac{4\pi}{\alpha(1+\alpha)} \left(\frac{E+511}{E+1024} \right)^2 \quad \mathrm{cm}^2/\mathrm{atom}. \tag{1.5}$$

E is the kinetic energy of the electron in keV and Z is the atomic number of the target element. α is the screening factor, which accounts for the screening of the core potential due to the electron cloud of the atom. It is approximated by

$$\alpha = 3.4 \times 10^{-3} \frac{Z^{2/3}}{E}. \tag{1.6}$$

The (stochastic) free pathlength to the next elastic scattering event is derived as described in the preceding section (Eqs. 1.2 and 1.4) applying the Rutherford cross section (1.5).

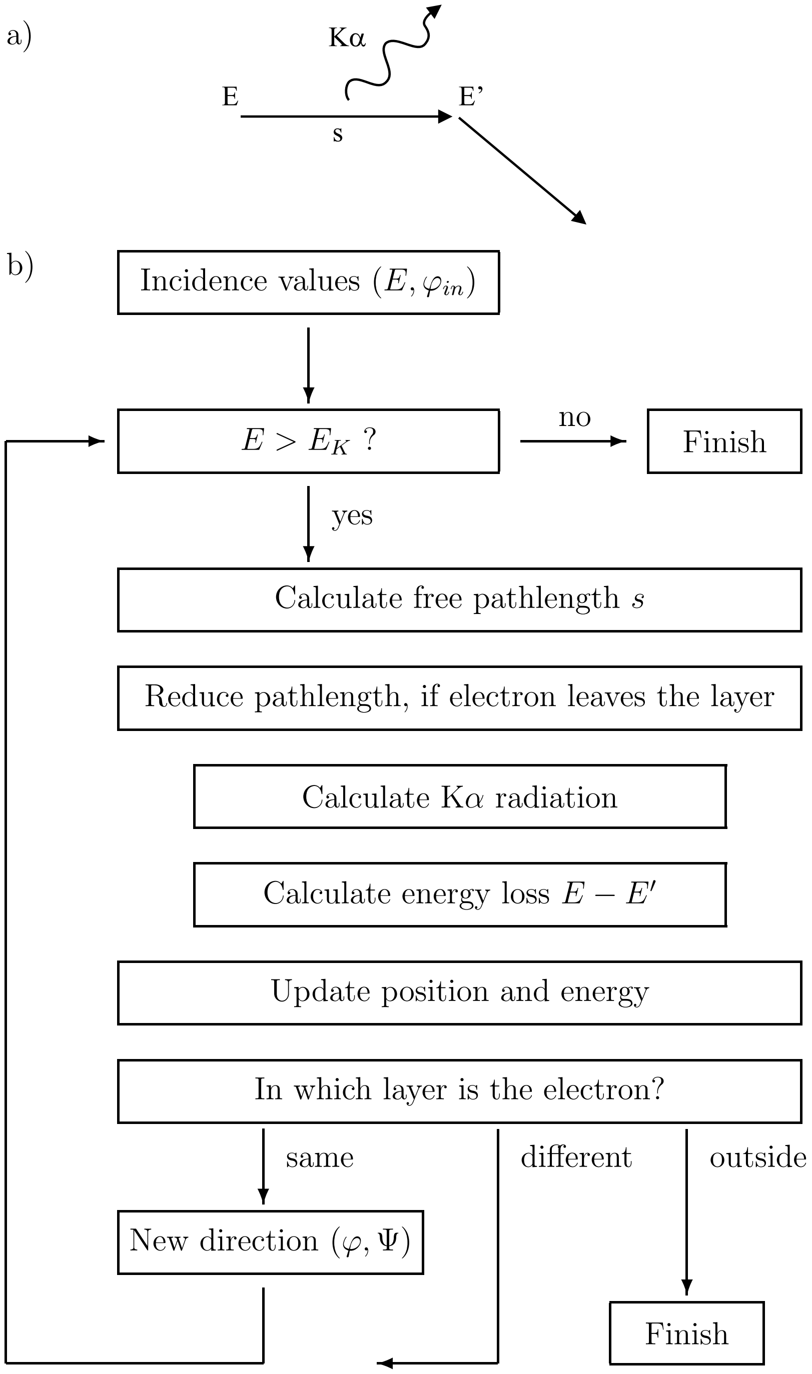

Figure 1.3: Scheme for calculating an electron's path. a) Illustration of the symbols. b) The algorithm. Elastic scattering events determine the free pathlength s and the direction of movement (φ, Ψ), while inelastic scattering causes the electron to lose energy, including the generation of Kα radiation. To handle multilayer targets, subroutines for adjusting the pathlength to the layer thickness and for switching between layers are included. The calculation of a scattering path stops when the electron leaves the target or when its energy E drops below the K-shell ionization energy E_K so that it can no longer produce Kα radiation.

The angular differential Rutherford cross section is given by

$$\sigma'_E = 5.21 \times 10^{-21} \frac{Z^2}{E^2} \left(\frac{E+511}{E+1024} \right)^2 \frac{1}{\left(\sin^2\left(\frac{\phi}{2}\right) + \alpha\right)^2}. \tag{1.7}$$

Then, the (stochastic) scattering angle ϕ is calculated as

$$\phi = arccos\left(1 - \frac{2\,\alpha\, RND}{1+\alpha - RND} \right). \tag{1.8}$$

The azimuth of the scattering Ψ is chosen randomly

$$\Psi = 2\,\pi\, RND. \tag{1.9}$$

All these expressions were taken from the book by Joy [48]. This book also gives a description of how to transform the scattering angles into the direction cosines of the electron movement in the 'laboratory' frame of the simulation.

On the pathlength s, the electron produces a number of K-shell vacancies in the target atoms. The cross section for the ionisation of the K-shell σ_K was taken from Casnati et al. [15]. The lengthy expression is given in Appendix A. Then, the number of Kα photons generated is the product of the number of created K-shell vacancies, the fluorescence yield ω and the relative line strength f of the Kα line $(I_{K\alpha}/I_K)$

$$I^0_{K\alpha} = s\, \frac{N_A\, \rho}{A}\, \sigma_K\, \omega\, f. \tag{1.10}$$

The values for ω and f were taken from Zschornack [104].

The generated radiation is isotropic and will be reabsorbed inside the target. The intensity which is finally emitted from the surface is then given by

$$I_{K\alpha} = I^0_{K\alpha}\, e^{-y/\lambda_{abs}}, \tag{1.11}$$

where y is the depth of the generation point inside the target[3], and λ_{abs} is the absorption length for the Kα radiation. In multilayer targets there is a seperate exponential factor for each layer which the photon has to pass.

In the continuous slowing-down approximation the energy loss of the electron ΔE on the pathlength s is the product of this pathlength and the 'stopping power', $-dE/ds$, which is the average energy loss per unit pathlength:

$$\Delta E = -\frac{dE}{ds}\, s. \tag{1.12}$$

---

[3] When the Kα emission is observed under an angle to the surface normal $\varphi_{obs} \neq 0$ the distance where reabsorption takes place prolongs to $y = y/\cos(\varphi_{obs})$.

The lengthy expression for the stopping power is given in Appendix B. It was taken from Berger and Seltzer [9].

If the final position of the electron as given by the free pathlength s is outside the actual target layer, the pathlength is reduced to the fraction inside this layer. This gives the correct values for the produced Kα radiation and the energy loss. When the electron enters into a different material in a multilayer target, it does not reach the calculated position of elastic scattering, so that its direction of movement does not change when entering the new layer. In the case that the electron leaves the target, the calculation of the trajectory stops. The calculation also stops when the electron's energy E drops below the lowest K-shell ionization energy E_K in the target.

1.2.3 Geometry

The Monte Carlo code can calculate the Kα emission for any side of the target: the front (where the electrons enter the target), the back (opposite the front) and one side perpendicular to the front.

The geometry corresponding to observation from the front is shown on the left in Fig. 1.4. The target can consist of up to four layers of different materials with different thicknesses and infinite lateral extension. The incidence angle of the impinging electrons, φ_{in}, and the observation angle of the Kα radiation , φ_{obs}, can be chosen. Both incidence and observation direction are restricted to the x-y plane.

For calculating the Kα emission from the back of foil targets, the same geometry is used. The only difference is that the reabsorption of Kα photons inside the target is now given by the distance of the generation point to the back instead of by the distance to the front.

The calculation of the Kα emission from the target side uses the same coordinate system as for the other sides, with the x-z plane corresponding to the target surface for which the radiation is calculated (Fig. 1.4, right). Thus, the algorithm remains the same, the only differences being:

1. The y-z plane defining an *additional* surface through which the electrons can leave the target.

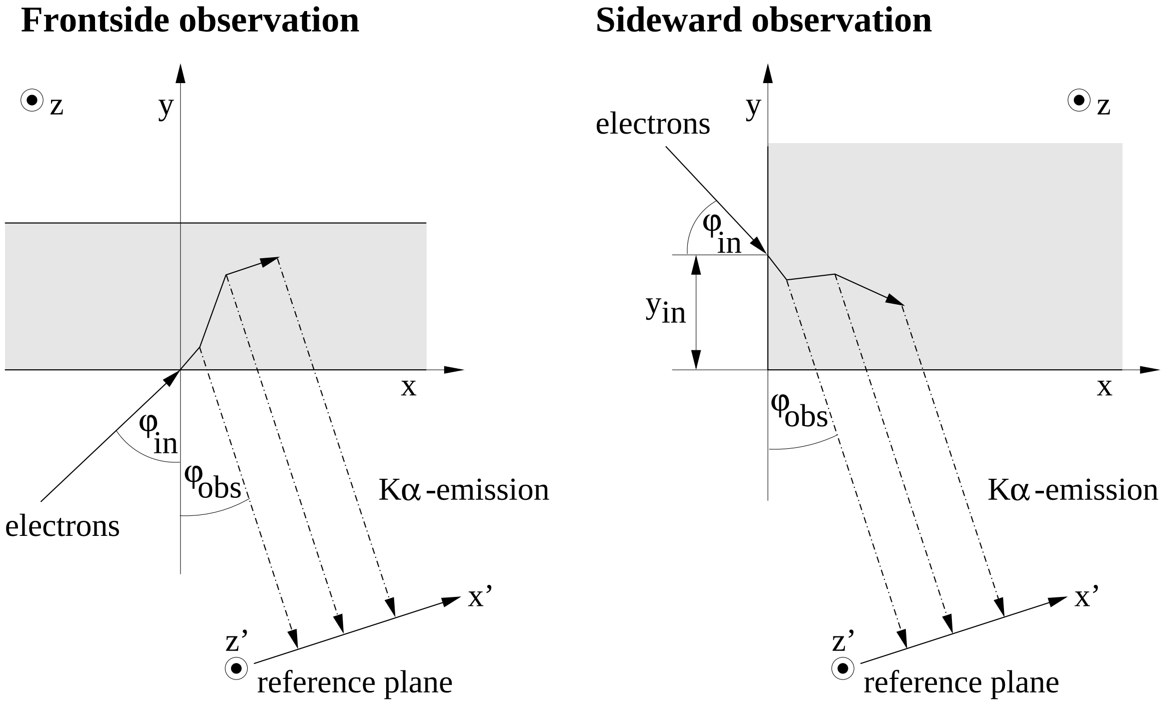
Frontside observation

Sideward observation

Figure 1.4: Geometry of the Monte Carlo code. The Kα emission can be calculated for any side of the target using two geometries. Left figure: Geometry for calculating the Kα emission from the target side where the electrons enter (‘frontside’). The same geometry is used for calculating the backside emission. The ‘reference plane’ is used for the calculation of space and time resolved emissions. Right figure: Geometry for Calculating the Kα emission from the sides perpendicular to the frontside. The coordinate system, and thus the main algorithm, is the same in both cases.

2. The electrons entering the target through this additional surface instead through the x-z plane. Their incidence angle now refers to the normal of the y-z plane.

3. The distance of the electron entrance point to the target edge, y_{in}, is an additional selectable parameter.

1.2.4 Diagnostics

Beside the total Kα yield, the Monte Carlo code can calculate the Kα emission temporally and spatially resolved. Then, the radiation hitting a planar detector is calculated. Numerically the detector is defined as a reference plane perpendicular to the observation direction, as indicated in Fig. 1.4.

For space-resolved calculations the reference plane has its own coordinate system $(\vec{e_x}', \vec{e_z}')$ which can be tilted against the main coordinate system $(\vec{e_x}, \vec{e_y}, \vec{e_z})$ when the observation angle φ_{obs} is different from zero. The coordinates (x', z') where an x ray hits the reference plane are derived from the electron's position (x, y, z) via

$$x' = y \sin(\varphi_{obs}) + x \cos(\varphi_{obs}), \tag{1.13}$$

$$z' = z. \tag{1.14}$$

The reference plane is divided into a grid, and for each grid point the Kα intensities hitting that point are summed up. The size of the plane and the size of the grid points are choosable.

The time at which a Kα photon reaches the reference plane is given by:[4]

1. The entry time of the electron into the solid t_0 (delivered by the PIC code).
2. The time it takes the electron to move through the target before the photon is created. For a single interval between two successive scattering events, the time Δt_s is given by the pathlength s and the relativistic velocity of the electron v which is derived from its kinetic energy

   $$E = \left(\frac{1}{\sqrt{1 - \frac{v^2}{c^2}}} - 1 \right) E_0. \tag{1.15}$$

   With the electron rest energy $E_0 = 511$ keV, the speed of light

   $$c = \frac{3 \times 10^8 \times 10^6 \, \mu\text{m}}{10^{15} \, \text{fs}} = 0.3 \, \frac{\mu\text{m}}{\text{fs}} \tag{1.16}$$

   and E in keV the electron velocity is

   $$v = \sqrt{1 - \left(\frac{511}{511 + E} \right)^2} \; 0.3 \, \frac{\mu\text{m}}{\text{fs}}, \tag{1.17}$$

   which gives (where s is in μm):

   $$\Delta t_s = s \, \frac{1}{0.3 \sqrt{1 - \left(\frac{511}{511+E} \right)^2}} \quad \text{fs}. \tag{1.18}$$

---

[4] The lifetime of the excited state of the target atom is a few femtoseconds or less [18] and can be neglected.

3. The time of flight of the photon to the detector is given by

$$\Delta t_d = (x \cos \varphi_{obs} - y \sin \varphi_{obs}) \frac{1}{0.3} \text{ fs} + \text{const}, \tag{1.19}$$

   where (x, y, z) is the position where the photon is generated (in μm).

The sum of the three terms gives the time t at which the photon is detected:

$$t = t_0 + \sum_s \Delta t_s + \Delta t_d. \tag{1.20}$$

The numerical detection time scale is divided into intervals of 5 fs, into which the 'detected photons' are sorted.

The code also includes several diagnostics to give deeper insight into the scattering of the electrons:

1. The electron trajectories are recorded. To reduce data, only an adjustable fraction of the trajectories is given out. Usually, plotting several tens of electron paths gives sufficient information on electron penetration in a given situation.

2. Analogous to the emitted Kα radiation the mean depth of all electrons $\langle y \rangle$ is calculated during time. For this, in each time interval t the depth y_i^t of all elastic scattering events i happening in this interval are summed up and then normalised by the number n^t of the scatterings:

$$\langle y \rangle^t = \frac{1}{n^t} \sum_{i=1}^{n} y_i^t \,. \tag{1.21}$$

   The time t when an elastic scattering takes place is given by:

$$t = t_0 + \sum_s \Delta t_s. \tag{1.22}$$

   The intervals were again chosen as 5 fs wide.

3. A time-integrated mean value of the electron depth $\langle y \rangle$ is calculated, i.e. the mean depth where the Kα photons are generated during the laser pulse.

4. For each initial electron energy the number of generated Kα photons is calculated as well as the mean pathlength and the mean excursion time of these electrons inside the target.

5. The numbers of reflected, transmitted and stuck electrons are counted.
6. For each 'reflected' electron (i.e. that leaves the target through the frontside) the energy and the exit angles φ and Ψ are given out, so that the angular distribution of the reflected electrons can be analyzed.

1.2.5 Electron Input Data

The initial data of the impinging electrons can be either taken from the results of a PIC simulation or from an analytical energy distribution (like a Maxwellian). The PIC code delivers a list of the individual hot electrons that are accelerated through the border of the PIC simulation-area into the direction of the solid, while an energy distribution gives for each electron energy E the number $f(E)$ of electrons with this energy.

To calculate the temporal development of the Kα emission from a laser plasma, the list of hot electrons delivered by the PIC code is transformed into a twodimensional electron distribution with one dimension being the entry time of the electrons and the other being their energy. The time and the energy dimension are both divided into intervals, with the central value of the interval taken as representative and being used for calculating a large number of electron paths (usually 100). The spacing of the energy intervals starts with the lowest K-shell excitation-energy in the target and is logarithmic with each interval covering $\pm 5\%$ of the central energy in the interval. E.g. the interval '100 keV' ranges from 95 – 105 keV. Then, all electrons with an energy within this interval are assigned the central energy 100 keV. This energy spacing reduces computational effort compared to a linear spacing (especially at high electron energies) without substantial loss in accuracy.[5] The time intervals are spaced linearly and are usually chosen as 5 fs wide.

In the same way, electron data from an analytical energy distribution is mapped into logarithmic energy intervals. As no information on individual entry times is provided, all electrons are given the same time. Because theoretical considerations (Eq. (1.32)) predict a functional relation between the energy of a hot electron and the direction in which it moves, each electron energy can be given its own entrance angle.

The hot electron data from PIC simulations also can be used for calculations with

---

[5] The deviations in Kα yield when using the logarithmic energy spacing instead of a linear one are less than 5 %.

electron-dependent entrance-angles. In this case, the electrons are not sorted into time and energy intervals, but for each hot electron the scattering path is calculated individually. Because the PIC simulation can yield much more hot electrons than are necessary for the Monte Carlo calculation (especially at high laser intensities), an upper limit can be set for the number of calculated electron paths (usually 10.000), so that only a fraction of the hot electrons from the PIC result is used.

1.2.6 Data of the Target Material

The properties of the target material are provided to the Monte Carlo code via a seperate data file which includes values for the atomic number Z, the atomic density n_A, the ionization energy of the K shell E_K, the properties of the Kα line: energy $E_{K\alpha}$, fluorescence yield ω and relative intensity f, and data to describe the x-ray absorption in the element.

To handle reabsorption in multilayer targets with a variety of material combinations in an easy way, for each element the absorption coefficient is parametrised in an energy range around the K-shell absorption edge of the element

$$\mu_{abs} = a\,\lambda^b \quad \mu\mathrm{m}^{-1}, \tag{1.23}$$

where the wavelength λ of the absorbed Kα radiation is derived from its energy (in keV),

$$\lambda = \frac{12.3969}{E_{K\alpha}} \quad \text{Å}. \tag{1.24}$$

Seperate values for the coefficients a and b are provided for the Kα energy being above or below the K-shell ionization energy. They were found by fits to the absorption data given in the book by Zschornack [104]. The fits are appropriate when the ionization energies E_K of the photon emitter and the absorber are not too different from each other (about half an order of magnitude).

Compound target materials can be treated by providing mean values for the atomic number $\langle Z\rangle$, atomic density $\langle n_A\rangle$ and the Kα absorption length $\langle \mu_{abs}\rangle$ weighted by the atomic densities of the different elements in the target material. This gives the correct average values for the mean free pathlength and the elastic scattering angles. The average stopping power can be calculated by applying an average value for the mean ionization potential $\langle J\rangle$. The calculation of these averages is explained in Appendix C. For all data

Material	⟨Z⟩	n_A	$\langle n_A \rangle$	$\langle J \rangle$	E_K	$E_{K\alpha}$	ω	f	$E_{K\alpha} < E_K$		$E_{K\alpha} > E_K$	
		(μm^{-3})	(μm^{-3})	(eV)	(keV)	(keV)			a (Å^{-1})	b	a (Å^{-1})	b
Ti	22	5.68×10^{10}			4.97	5.68	0.21	0.90	3.69×10^{-3}	2.63	2.89×10^{-2}	2.67
Cu	29	8.46×10^{10}			8.98	8.05	0.47	0.89	1.54×10^{-2}	2.66	0.11	2.72
Ag	47	5.83×10^{10}			25.5	21.2	0.83	0.84	6.95×10^{-2}	2.64	0.41	2.68
Ta	73	5.51×10^{10}			67.4	57.5	0.96	0.78	0.35	2.59	1.92	2.68
Si	14	4.99×10^{10}			1.84	1.74	0.04	0.95	4.20×10^{-4}	2.69	5.00×10^{-3}	2.70
SiO_2	10	2.66×10^{10}	7.97×10^{10}	140	1.84	1.74	0.04	0.95	1.91[6]	0	-	-
mylar ($C_5H_4O_2$)	4.54	4.32×10^{10}	9.52×10^{10}	76.9[7]	0.3[8]	0.28	0.003	1.00	-	-	2.64×10^{-4}	2.94

Table 1.1: Properties of target materials used by the Monte Carlo code.

---

[6] The absorption data is only valid for the Si Kα line.

[7] Value according to Eq. C.3. The value in the Berkeley tables is $\langle J \rangle = 78.7$ eV.

[8] Data for carbon.

concerning the generation of Kα radiation from one element in the target the values of this element (n_A, E_K, $E_{K\alpha}$, ω and f) must be used.

Table 1.1 gives the applied target data for a number of pure elements and compound materials.

1.2.7 Accuracy

The reproducibility of a Monte Carlo simulation becomes better when the statistics are increased, in the present case with the number of electron trajectories being calculated. On the other hand, computation time and thus the number of calculated paths should be kept low. To find an optimum value, series of simulations using monoenergetic electron beams were performed with the number of calculated paths varying between the series. For a number of 100 calculated paths, a reproducibilty of the Kα yield within ±5% was found, while the fraction of reflected electrons varied ±15%. Increasing the number of paths to 1000 decreases both variations to ±2%. In the simulations, usually 100 scattering paths were calculated per initial electron energy.

For monolayer targets, a faster algorithm was implemented. In these targets, all energy losses of the electron take place in the same material. Thus, for all scattering paths with the same initial energy, the energy and the cross sections only depend on the *length* of the path already covered by the electron. They can be calculated in advance if the distances between the elastic scattering events are chosen to be equal for all paths. In the faster algorithm, these distances are chosen as the mean free pathlength $\lambda(E)$. This results in typically several hundred to several thousand elastic scattering events per electron path. To check the accuracy of the algorithm, calculations with and without the approximation were compared. The differences in Kα yield and the numbers of reflected and transmitted electrons were less than 5%.

To check the validity of the calculated Kα yields, the simulation results were compared with the experimental data given by DICK et al. [21] (Fig. 1.5). In this work, the Kα yield from target elements ranging from C ($Z = 6$) to Au ($Z = 79$), which were bombarded with monoenergetic electron beams with energies from 10 keV to 3 MeV, was measured. A comparison of the experimental and simulated data is shown in Fig. 1.5. In general, they agree within 10 % or less. For medium Z elements like Cu, the difference is up to 25 %

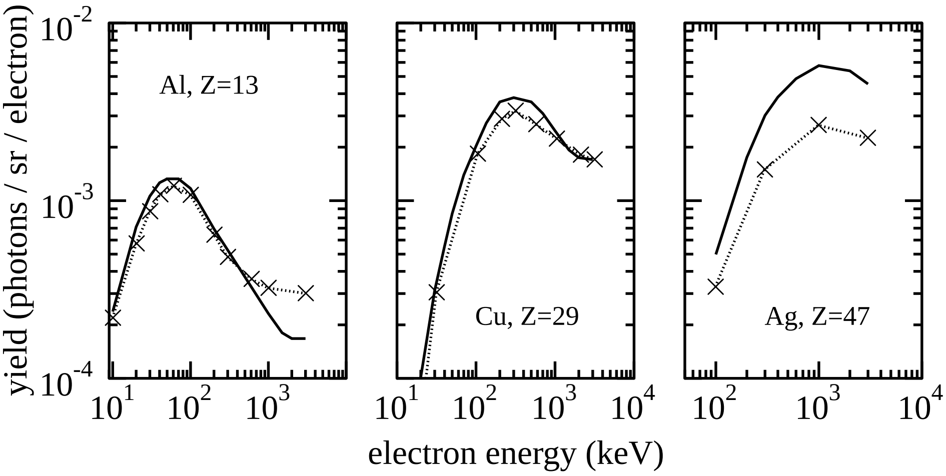

Figure 1.5: Comparison of Kα yields calculated with the Monte Carlo code (crosses) and experimental data (solid line) for different target elements. The experimental values are from Dick et al. [21].

in the energy range from 100 keV to 1 MeV. Deviations of a factor ~ 2 are found above 1 MeV for low Z elements (Al) and in the whole energy range for high Z targets (Ag).

To check wether the absorption coefficients μ_{abs} of the Kα radiation (Eq. (1.23)) are the reason for these discrepancies the absorption data given by Zschornack [104] were cross-checked with the database of NIST [62], giving practically the same absorption coefficients μ_{abs}. For the K-shell ionization cross sections σ_K the paper by Hombourger [46] gives an extensive comparison between experimentally determined values and (among others) the Casnati formula (Eq. (A.1)). For Ag and Au reasonable agreement is found for electron energies up to several MeV, though the uncertainty of the experimental data makes a definite statement about the validity of the formula under these conditions difficult. Another possible explanation for the discrepancies apparent in Fig. 1.5 can be the Rutherford cross sections for elastic scattering (Eqs. (1.5) and (1.7)). Errors in these cross sections can let the electrons penetrate deeper into the target in the simulation than they do in reality, resulting in too much reabsorption and too little emitted Kα radiation.

The discrepancy for low Z materials is not of great practical importance, as the combination of MeV electrons with low Z materials is rather unusual, but the deviations for high Z elements require special care when carrying out simulations with these materials. It should be pointed out, that in all cases, the Monte Carlo code reproduces the maximum in Kα yield and its position, which all elements show at medium electron energies.

1.3 The PIC Code

1.3.1 Principles

The microscopic behaviour of a plasma is described by the equations of motion of its particles i

$$\frac{d}{dt}\boldsymbol{x}_i = \boldsymbol{v}_i, \tag{1.25}$$

$$\frac{d}{dt}(m_i\boldsymbol{v}_i) = \boldsymbol{F}_i, \tag{1.26}$$

where $\boldsymbol{x}_i$, $\boldsymbol{v}_i$ and m_i are the position, the velocity and the mass of the particle respectively.

$$\boldsymbol{F}_i = q_i\,(\,\boldsymbol{E}(\boldsymbol{x}_i) + \boldsymbol{v}_i \times \boldsymbol{B}(\boldsymbol{x}_i)\,) \tag{1.27}$$

is the force acting on the particle with charge q_i. The electric field strength $\boldsymbol{E}$ and the magnetic induction $\boldsymbol{B}$ result both from the particles and from the field of the laser incident on the plasma. They are related to each other and to the charge and current density of the plasma particles, ρ and $\boldsymbol{j}$, via Maxwell's equations

$$\nabla\boldsymbol{E} = -\frac{1}{\varepsilon_0}\rho, \tag{1.28}$$

$$\nabla \times \boldsymbol{E} = -\dot{\boldsymbol{B}}, \tag{1.29}$$

$$\nabla \times \boldsymbol{B} = \mu_0\,\varepsilon_0\,\dot{\boldsymbol{E}} + \mu_0\,\boldsymbol{j}, \tag{1.30}$$

where ε_0 is the dielectric and μ_0 the permeability constant.

The equations of motion describe the behaviour of discrete particles (using single particle properties q_i, m_i, $\boldsymbol{x}_i$ and $\boldsymbol{v}_i$). The field equations instead apply quantities which are continuous in space ($\boldsymbol{E}$, $\boldsymbol{B}$, ρ, $\boldsymbol{j}$) though they partly originate from the properties of single particles (in our case q_i and $\boldsymbol{v}_{\boldsymbol{i}}$). [9]

In a Particle-In-Cell (PIC) code the continous quantities $\boldsymbol{E}$, $\boldsymbol{B}$, ρ and $\boldsymbol{j}$ are represented by their values on a regular array of mesh points [10, 45]. Within the computation cycle

---

[9] Instead of using the field equations Eqs. (1.28) – (1.30) the force acting on a particle can be also expressed as the sum of the forces originating from the other particles and an external force from the laser field: $\boldsymbol{F}_i = \sum_{j\neq i}\boldsymbol{F}_{ij} + \boldsymbol{F}^{ext}$. This is done in particle-particle codes. Compared to the particle-particle method the particle-mesh scheme applied in PIC codes results in a significant saving of computation time for larger numbers of simulation particles.

of a PIC code a transformation from particle to mesh point properties and vice versa is performed:

1. The charges and velocities of the simulation particles are mapped to nearby mesh points, giving the charge and current density distributions $\rho(\boldsymbol{x})$ and $\boldsymbol{j}(\boldsymbol{x})$.
2. The electric and magnetic fields $\boldsymbol{E}(\boldsymbol{x})$ and $\boldsymbol{B}(\boldsymbol{x})$ are derived by solving the field equations (1.28) – (1.30) on the mesh points.
3. The force acting on each simulation particle (Eq. 1.27) is obtained by interpolating between the mesh-defined values of $\boldsymbol{E}(\boldsymbol{x})$ and $\boldsymbol{B}(\boldsymbol{x})$.
4. The equations of motions, (1.25) and (1.26), are applied to update the particles' positions and velocities.

To simulate the interaction of an oblique laser beam with a plain target (i.e. periodic in two directions y and z) Gibbon and Bell [36] introduced the boost-frame technique to PIC codes. In this technique the calculations are performed in a reference frame which moves parallel to the target surface with a velocity $v_{0y} = c \sin\Theta$ (Θ is the incidence angle of the laser beam). In this 'boosted' reference frame the laser appears to be normally incident on the target surface, while the plasma streams at a velocity $-v_{0y}$. Thus, the calculations are reduced to only one spatial (the direction of the surface normal x) and two velocity coordinates (v_x and v_y) — with considerable savings in computation time compared to a two-dimensional simulation. A detailed discussion of the subtleties of the Lorentz transformations used for boosting to and from the simulation frame is given in Gibbon et al. [38].

1.3.2 Application of the PIC Code

In the present work the $1\frac{1}{2}$D, oblique incidence, Particle-In-Cell code BOPS [36] was used for the simulation of the laser interaction with the plasma and the generation of hot electrons.

The calculations were performed for a p-polarized[10] titanium:sapphire laser (λ_{Laser} = 800 nm) with an incidence angle of 45° as it was used in the experiments. $\sin^2$-pulses

---

[10] The electric vector of the laser light is in the plane of incidence and thus has a component perpendicular to the plasma surface.

with a pulse duration corresponding to Gaussian pulses with a full width at half maximum (FWHM) of either 60 or 90 fs were used.[11]

The plasma density in the simulations decreased exponentially with a normalised scale length $L/\lambda_{Laser} = 0.3$. This scale length is appropriate to interactions where a laser prepulse or pedestal generates a small amount of preformed plasma [5] and to the laser conditions in the experiment described in the following chapter (Section 2.3). The maximum plasma electron density was $n_e(max) = 10\, n_c$, with n_c being the critical density. At the critical density the frequency of the electron plasma oscillations, $\omega_{pe} \propto \sqrt{n_e}$, is equal to the laser frequency, defining an upper limit of the plasma density to which the oscillating laser field can penetrate before it is shielded out by the plasma electrons. The generation of the hot electrons happens at the critical density.

The simulation particles were initialized with Maxwellian energy distributions corresponding to a plasma temperature $kT = 200$ eV. Higher temperatures would include electrons with energies high enough to ionize the K-shell of Si, which was one of the investigated target materials. That would result in the generation of Kα photons even without a laser pulse. To have sufficient statistics at the critical density, 40.000 electron and 40.000 ion simulation particles were used. To keep the plasma electrically neutral, for each simulation particle leaving the simulation area (especially the generated hot electrons) another particle was reinjected with a velocity corresponding to the initial energy distribution. With these parameters, simulating the interaction of a 90 fs laser pulse with the plasma took about ten hours.

As the PIC code is one dimensional, each simulation particle corresponds to a charge sheet with infinite lateral extension. To derive the actual number of generated hot electrons, the number of absorbed simulation particles must be multiplied by a scaling factor, c_s, which is mainly the product of the normalised charge of a simulation particle, q_e, with the size of the laser irradiated area A (in μm^2)

$$c_s = 1.6 \times 10^8\, \lambda_{Laser}^{-1}\, A\, |q_e|. \tag{1.31}$$

For the simplifying assumption of a laser spot with a given homogeneous intensity, used in Chapters 3 and 5, the irradiated target area A is proportional to the laser energy, as are

---

[11] 'Corresponding' means that the energy in both pulses is the same. Then, the pulse duration must be chosen as $\tau_{\sin^2} = 2.13$ FWHM$_{Gauss}$.

the number of generated hot electrons and that of the produced Kα photons.

The PIC code produces two lists of the generated hot electrons which are used as an input to the Monte Carlo code. One list contains the kinetic energy of each hot electron and the time at which it leaves the PIC simulation area (i.e. the entrance time into the solid). These lists are used for calculating the temporal development of the Kα emission (Chapter 5) and were also applied for the investigation of the total Kα yield (Chapter 3).

Due to the conservation of energy and momentum between the absorbed laser photons and the accelerated electron a functional dependence of the entrance angle of the electron, φ_{in}, on the electron's normalised kinetic energy, $U = E/m_e c^2$, and the incidence angle of the laser, Θ, is expected [80, 83]:

$$\varphi_{in} = 2\pi - \arctan\left(\frac{U \sin\Theta}{\sqrt{2U + U^2 \cos^2\Theta}}\right). \tag{1.32}$$

Therefore, the second electron list delivered by the PIC code gives the kinetic energy and the entrance angle of each hot electron. These lists with individual entrance angles of the hot electrons are used for calculating the spatial distribution of the Kα emission (Chapter 4).

1.4 Calculating Spatial Kα Distributions

In the following Chapter an experiment is described in which images of the Kα emission from fs laser-irradiated Ti targets were taken. The spatial Kα distributions measured in this experiment were compared with the predictions of the simulation model. The calculation of the numerical images consisted of four steps:

1. Determination of the experimental laser beam profile. The procedure is described in Section 2.3 with example beam profiles shown in Fig. 2.3.

2. Combined PIC-MC calculations for the experimental laser parameters and a range of laser intensities giving the spatial Kα distributions resulting from point-like laser spots (Fig. 1.6,a). In the simulations shown in Chapters 2 and 4 the area A of these 'point-like' laser spots was chosen as 1 μm^2 corresponding to a distance of 1 μm between neighbouring points of the summation grid (see next point). The area A enters the number of calculated Kα photons via the scaling factor c_s in Eq. (1.31).

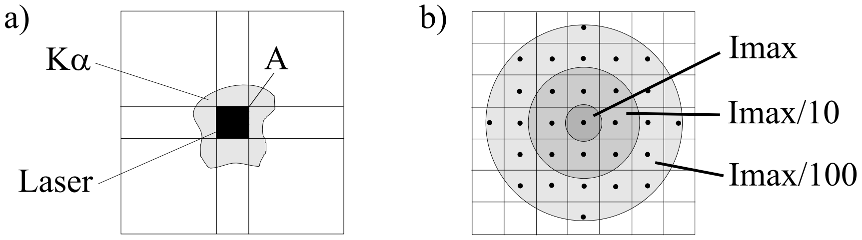

Figure 1.6: Calculating spatial Kα distributions: a) Kα emission for a ‘point-like’ laser spot with area A. b) Summation grid of points within the focal area irradiated with different laser intensities.

3. Summation of the Kα emissions, calculated for point-like laser spots, for a grid of irradiated points within the focal area (Fig. 1.6,b). The laser intensity for each grid point is chosen accordingly to the measured laser beam profile. This gives the numerical intensity distribution of the Kα source for the experimental laser conditions.

4. To derive a Kα image which can be directly compared with the experimental images, ray tracing [22, 23] was applied with the calculated x-ray source as an input.

Chapter 2

Two Dimensional Monochromatic Imaging of the Kα Emission

A common method to measure the size of the Kα emission from a laser-produced plasma is the knife-edge technique or one-dimensional x-ray shadowgraphy [87]. A razor blade is put between the target and a spatially resolving x-ray detector. The x-ray source illuminates the detector uniformly except for those parts which are partly covered by the razor blade. A deconvolution procedure yields the intensity profile of the x-ray source [1]. Though the x-ray intensity in this technique is spatially integrated parallel to the knife edge the 1/e-width of a Gaussian x-ray source is retained in the integration and so the method is widely used to estimate size of the x-ray source, or more precisely: its halfwidth [25, 66, 74, 98].

In the present thesis the spatial intensity distribution of the Kα emission from laser-irradiated Ti targets was resolved in two dimensions, using bent crystals which focus an image of the Kα source onto a CCD camera [29, 33]. The two-dimensional resolution of the imaging delivers a set of structural details which are smeared out in a knife-edge measurement. The laser parameters and the imaging properties of the crystals were carefully determined, so that the experimental situation could be reproduced with high accuracy by the numerical model presented in the preceding chapter. The comparison between the structural details of the Kα emission in the experiment and in the simulations gives a set of agreements and differences from which an estimate can be made of

1. how far the physics in the experiment is described by the numerical model, and

2. what effects outside the model could be responsible for the deviations.

Concerning the question wether numerical models like the presented one correctly predict the penetration depth of the hot electrons into the target [66, 93] or wether the penetration depth is much shorter [47, 92], there is a controversy in the literature. Usually, multilayer targets [16] are used to study the penetration depth, which is then deduced from the

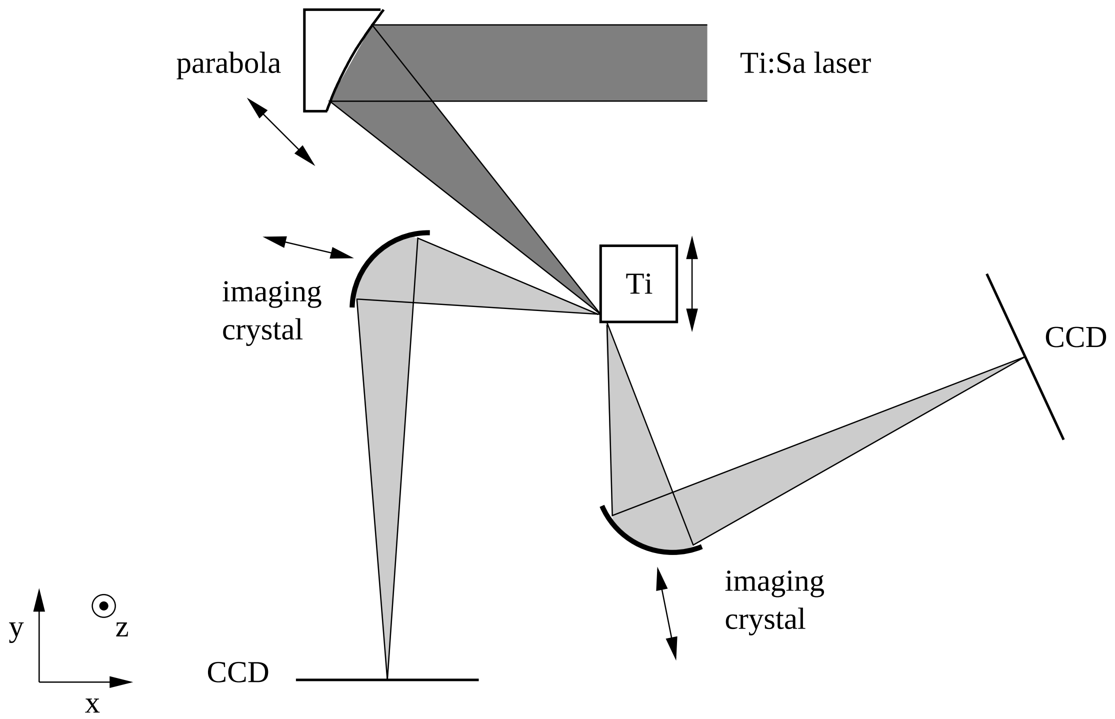

Figure 2.1: Scheme of the experimental setup. The indicated coordinate system is the same as used for the Monte Carlo code (Fig. 1.4).

change of the Kα yields, when the thickness of the top layer is varied. Instead of that, in the present thesis, the Kα emission from a target side perpendicular to the laser-irradiated side was imaged with a bent crystal onto a CCD camera, so that one coordinate of the resulting image corresponds to the target depth and the decrease of the Kα signal with depth indicates the electrons' penetration behaviour.

2.1 Experimental Setup

The experimental setup (Fig. 2.1) was arranged around the position of the Kα source, which was given by the intersection of the axis of the laser focus with the front side of the target. Two sides of each target were carefully prepared to form a well defined rectangular edge. In the measurements of the electron penetration depth the laser was focused close to this edge, so that the target was optically thin for the sideward Kα emission. In the studies of the spatial structure of the frontside emission the focus was 2 mm away from the edge. The laser could be defocused by moving the parabola along the focal axis toward the target or away from it. For each of the two sides a toroidally bent Si crystal delivered

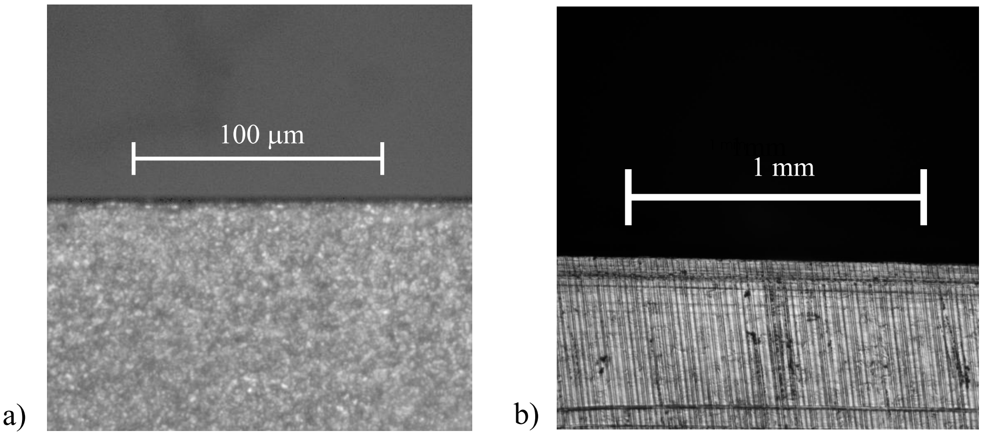

Figure 2.2: The edges of the Ti targets used in the experiment. a) Abraded and polished by hand. The curvature at the edge has a radius $\lesssim 5$ μm. b) Straightness of a target edge made with a diamond milling machine.

a two dimensional, magnified image (7×) of the Kα emission from this target side onto a CCD camera. For each imaging crystal the distance to the target could be optimzed during the experiment to focus the Kα image. All parts of the setup, the parabola, the laser focus, the imaging crystals and the cameras, were placed at the same height, in one horizontal plane. The prepared target edge was oriented perpendicular to this plane (i.e. vertically). After each shot, the target was moved along the edge (500 μm) to an unused part. To change the position of the laser focus relative to the target edge, the target was moved horizontally parallel to the target frontside.

2.2 The Target

The experiment required targets with an edge of high geometrical quality. The concept of the experiment is to image the Kα emission from two target sides, with one side defined as ‘the side hit by the laser’ and the other as ‘the side not hit by the laser and perpendicular to the first one’. To guarantee these definitions, it was necessary that the curved or otherwise misformed area at the target edge was small in comparison with the laser focus and the absorption length for Ti Kα radiation (19 μm). At best focus, the laser spot had a full width at half maximum (FWHM) of 3 μm. Another requirement was that the target edge had to be straight, so that its position would not change when the target was moved vertically from shot to shot. Additionally, it was necessary that the target side hit by the laser was polished, as it showed that otherwise the from-shot-to-shot reproducibility was too bad.

After many attempts, two suppliers for Ti targets of the required quality could be established. One of them was the company Kern Micro- und Feinwerktechnik GmbH & Co. KG in Murnau-Westried, using a diamond milling machine. The other one was the materials preparation laboratory of the physics department at the Humboldt University in Berlin, which worked with freehand polishing.

The radius of curvature of the target edges was determined with a contact needle and showed to be 5 μm or less. Also, each target was controlled under a microscope (Fig. 2.2). The biggest damaged regions found in these examinations (pieces broken away) were about 10 μm in size. These parts of the targets were not used in the experiment.

2.3 Laser Parameters And Focus Size

For the experiments the titanium:sapphire laser ($\lambda_{Laser} = 800$ nm) of the Institut für Optik und Quantenelektronik at the Jena University was used. It delivers an energy of 240 mJ onto the target and was focused with an off-axis parabola ($f = 120$ mm, 45°) to an intensity of up to 7×10^{18} W/cm^2. 85% of the energy were within a diameter of 50 μm [103]. The laser was p-polarized and the angle of incidence was 45°.

The temporal shape of the laser pulse was measured with a third order multi-shot autocorrelater. A pulse shape similar to that described by Ziener et al. [103] for the same laser was found with a pulse duration of 90 fs. The laser has two intrinsic prepulses with intensity contrast ratios of 3×10^{-4} and 3×10^{-3} at 4 ps and 600 fs before the main pulse, respectively. As discussed by Ziener et al., these prepulses create a preplasma with a density gradient similar to that used in the PIC simulations described in the preceding Chapter (Section 1.3).

The parabola was adjusted using a microscope and a CCD camera. Then, images of the laser focus were taken for defocus distances -400 μm $\leq f_p \leq$ +400 μm,[1] where the defocus distance f_p is defined as the difference between the actual parabola-to-target distance d

---

[1] The defocus range for which the focus could be measured was limited by the size of the CCD.

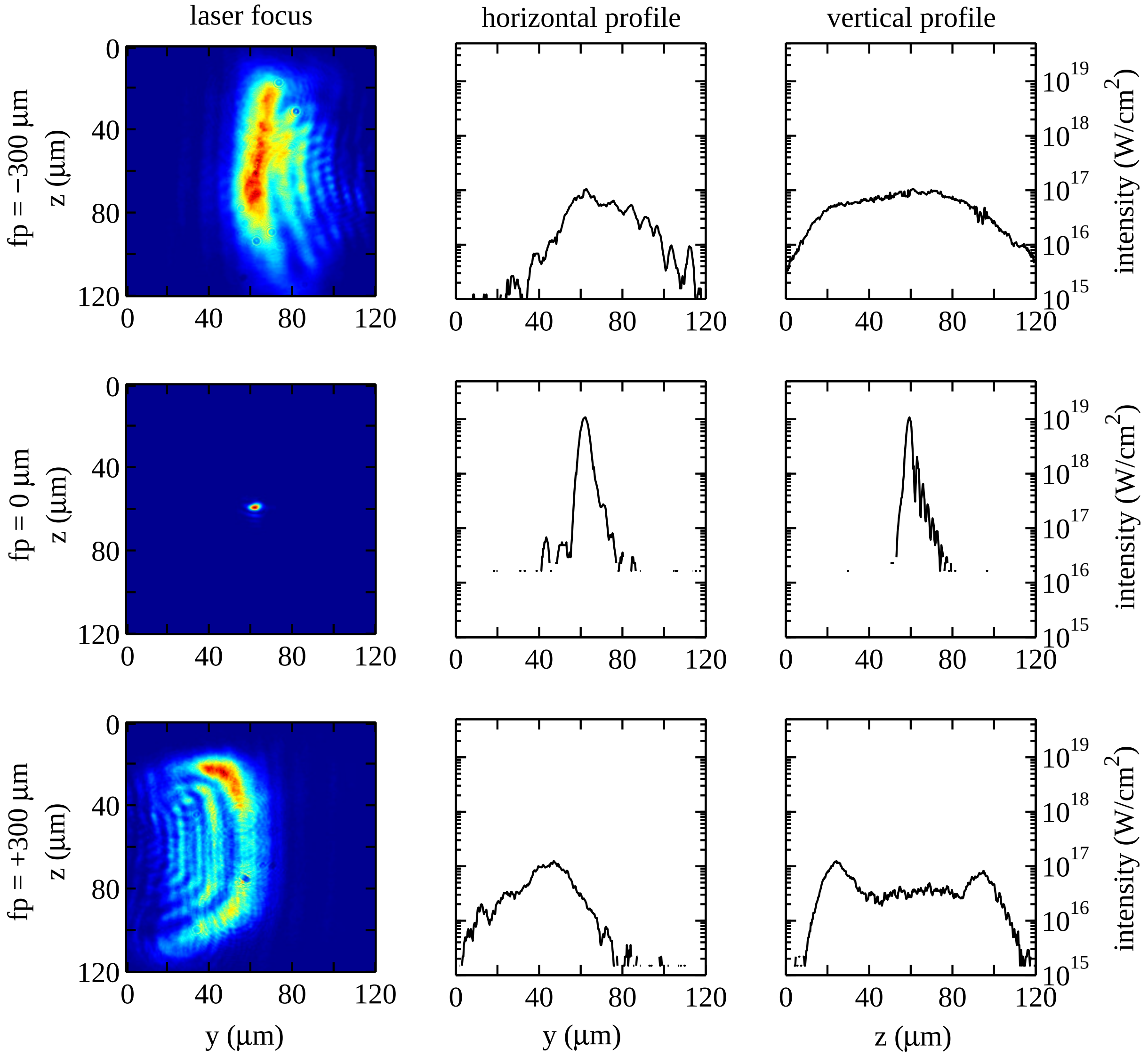

Figure 2.3: Intensity distribution of the laser focus for different defocus distances f_p.

and the focal length f of the parabola:

$$f_p \equiv d - f. \tag{2.1}$$

With the help of removable grey filters in front of the camera a total dynamic range of 10^3 was achieved. To estimate the intensity distribution in the focus, two CCD images taken with and without grey filter were superimposed. First, the background was subtracted and the signal without grey filter was multiplied by the transmission of the filter. Then, the overexposed parts of this image were substituted by data from the other image whereat the images were shifted interactively against each other to achieve optimum continuity of

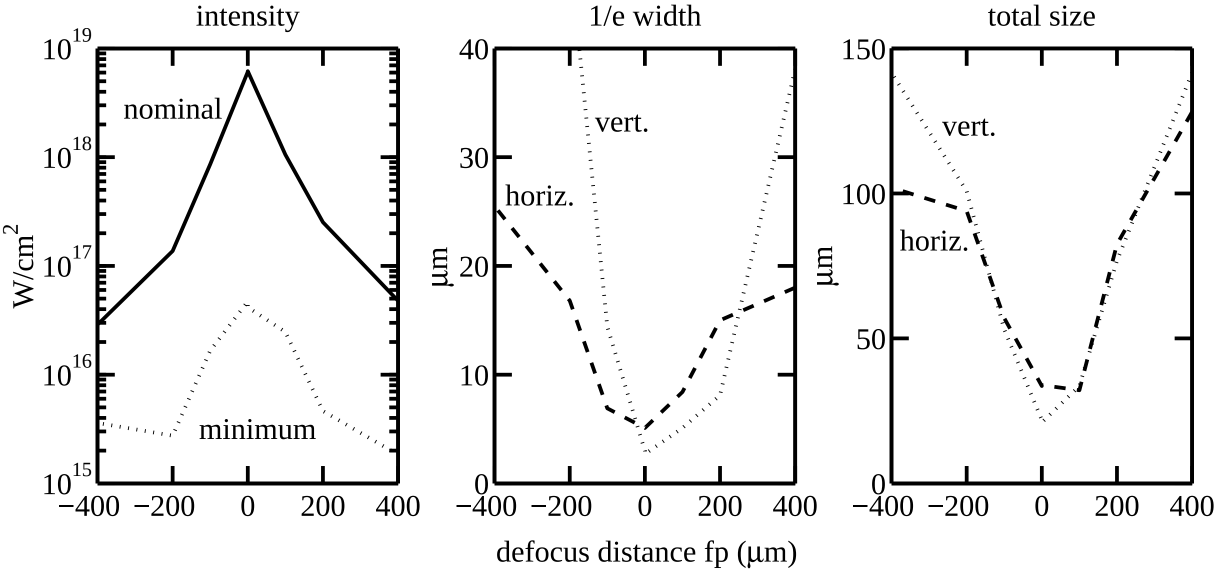

Figure 2.4: Intensity, peak width and total size of the laser focus. The 'nominal' intensity is the mean intensity within the 1/e width. The lowest intensity which could be measured is indicated by the dotted line labeled as 'minimum'; the corresponding maximum measured extension is shown in the 'total size' graph.

the resulting image. The CCD counts were conversed into laser intensity, I, by

$$\frac{\Delta I}{\text{count}} = \frac{1}{N_{tot}} \frac{E_{tot}}{\tau_l\,(dx/k)^2}, \tag{2.2}$$

where E_{tot} is the total laser energy on the CCD, N_{tot} is the sum of all counts in the image, τ_l is the duration of the laser pulse, dx the pixelsize of the CCD image, and k the magnification of the microscope. Fig. 2.3 gives examples of the resulting images and intensity profiles.

The nominal laser intensity was identified with the mean intensity in the 'peak', defined as the area, where the laser intensity was above 1/e of its maximum value. At best focus the nominal laser intensity was 7×10^{18} W/cm^2 and the maximum intensity was $\gtrsim 1 \times 10^{19}$ W/cm^2. The nominal peak diameter (1/e width) was 4 μm, corresponding to a peak area of $\sim$14 μm^2. It contained 47% of the laser energy on the target. The intensity fell off exponentially, and 90% of the energy was within a nominal diameter of 16 μm. Fig. 2.4 shows how the laser intensity and the focus size change when the defocus distance is varied. Comparison with an idealized laser focus shows that the peak intensity behaves similar to that of a Gaussian focus with a halfwidth of 3 μm.

2.4 The Imaging

2.4.1 Crystal Optics

The applied x-ray imaging with bent crystals works very much like the imaging with a concave mirror in the optical range but with the additional requirement that each reflected beam has to fulfill the Bragg law

$$2\,d_{hkl}\,\sin\Theta_0 = n\,\lambda, \tag{2.3}$$

where λ is the wavelength of the x rays, n the order of diffraction, Θ_0 the angle of incidence, the 'Bragg angle', and d_{hkl} the distance between the lattice planes of the crystal with Miller's indices hkl. The Bragg condition limits the range of reflected wavelengths to a maximum of two times the lattice spacing, which automatically excludes the longer wavelength plasma emissions from the imaging in the experiment.

The focal length, f, of a two-dimensionally bent crystal depends on the Bragg angle and the bending radii, $R_{h/v}$, and is different in the horizontal and in the vertical direction (where the dispersion plane is horizontally):

$$f_h = \frac{R_h\,\sin\Theta_0}{2}, \tag{2.4}$$

$$f_v = \frac{R_v}{2\,\sin\Theta_0}, \tag{2.5}$$

so that for a spherically bent crystal ($R_h = R_v$) the vertical and the horizontal focus are seperated. In contrast, a toroidally bent crystal with

$$\frac{R_v}{R_h} = \sin^2\Theta_0 \tag{2.6}$$

(as used in the experiments) only has one focal length.

The Bragg angle and thus the reflected wavelength vary along the crystal parallel to the dispersion plane. The total transmitted spectral bandwidth, $\Delta\lambda$, is thus limited by the horizontal aperture $\Delta s_{crystal}$ [57]:

$$\Delta\lambda \approx \lambda \left|\frac{k-1}{k+1}\right| \frac{\Delta s_{crystal}}{R_h\tan\Theta_0}, \tag{2.7}$$

where k is the magnification of the imaging. Or the other way around: For a narrow spectral line only a small stripe[2] $\Delta s_{crystal}$ of the crystal contributes to the imaging. The

---

[2] In the experiment a horizontal width of $\Delta s_{crystal} \approx 0.5$ mm contributed to the reflection of the Ti Kα doublet ($\Delta\lambda \approx 1$ Å).

total number of reflected photons, N_{ref}, is given by[3] [57]

$$N_{ref} = N_L \, \frac{(2k)^2}{k^2 - 1} \, \frac{\Delta h_{crystal} \, R_{int}}{\sin \Theta_0 \, R_h}. \tag{2.8}$$

N_L is the total number of photons emitted in 1 sr, R_{int} the integrated reflectivity of the crystal and $\Delta h_{crystal}$ its vertical height.

To produce a focused image the imaging equation

$$\frac{1}{l_a} + \frac{1}{l_b} = \frac{1}{f} \tag{2.9}$$

must be satisfied (l_a and l_b are the source-to-crystal and the crystal-to-image distance respectively). The magnification, k, is given by the ratio of l_b to l_a

$$k = \frac{l_b}{l_a}, \tag{2.10}$$

which results in

$$l_a = f \, \frac{k+1}{k}, \tag{2.11}$$

$$l_b = f \, (k+1) \tag{2.12}$$

for the distances needed to achieve a magnification of k.

Table 2.1 gives the properties of the two identical crystals in the experiment.

Crystal	Θ_0	R_h	R_v	R_{int}	$\Delta h_{crystal}$	k	l_a	l_b	N_L/N_{ref}
	degrees	mm	mm	μrad	mm		mm	mm	
Si (311)	57.01	149.79	106.39	28.95	5	7	72	504	2.1×10^5

Table 2.1: Data of the imaging crystals. N_L/N_{ref} is the number of Kα photons emitted in 1 sr for each photon on the image.

2.4.2 Influence of Aberrations on The Imaging of Extended Objects

This section examines how the crystal optics influences the experimental image of an x-ray source. To that purpose x-ray images of known sources with different shapes (pinhole

---

[3] Eq. 2.8 is only valid, if the x-ray source is not placed on the so-called Rowlandcircle, in which case k would be one.

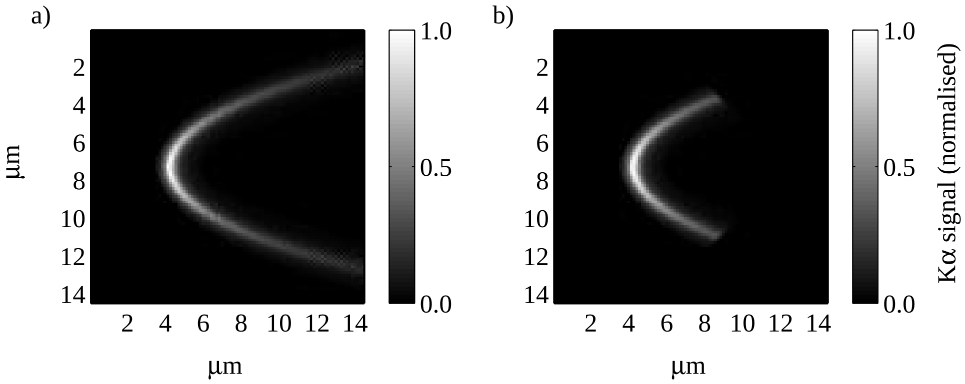

Figure 2.5: Aberrations of a Ti Kα point source for a magnification of 7, calculated with ray tracing. a) Full aperture. b) The vertical aperture is restricted to 3 mm. The distances refer to distances on the object.

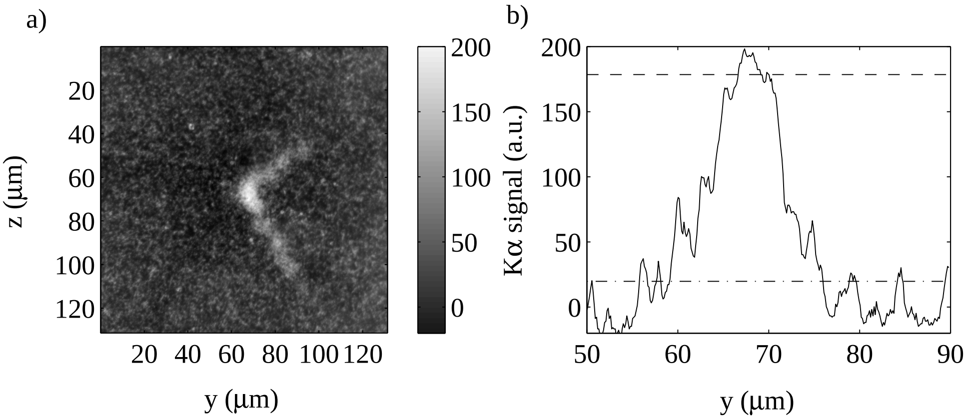

Figure 2.6: Measured aberrations of a 5 μm pinhole for a magnification of 5.3 and full aperture. a) X-ray image of the pinhole. b) Horizontal profile of a). The horizontal lines mark 10% and 90% of the maximum intensity. Distances refer to distances on the object.

and Gaussian) and different sizes are studied. Also, the necessary precision of the crystal adjustment is examined.

The deviation of the toroidal shape of the imaging crystals from the ideal ellipsoid results in an astigmatism which forms the dominating aberration of the imaging with these crystals [22]. For a point source the astigmatism results in two symmetrical tails stretching horizontally (parallel to the dispersion plane) into the direction of higher Bragg angles (Fig. 2.5,a). These tails are due to the dependence of the focal length on the vertical position on the imaging crystal, so that their length can be reduced by a diaphragm which restricts the vertical aperture (Fig. 2.5,b). In the experiments a Cu foil with a vertical

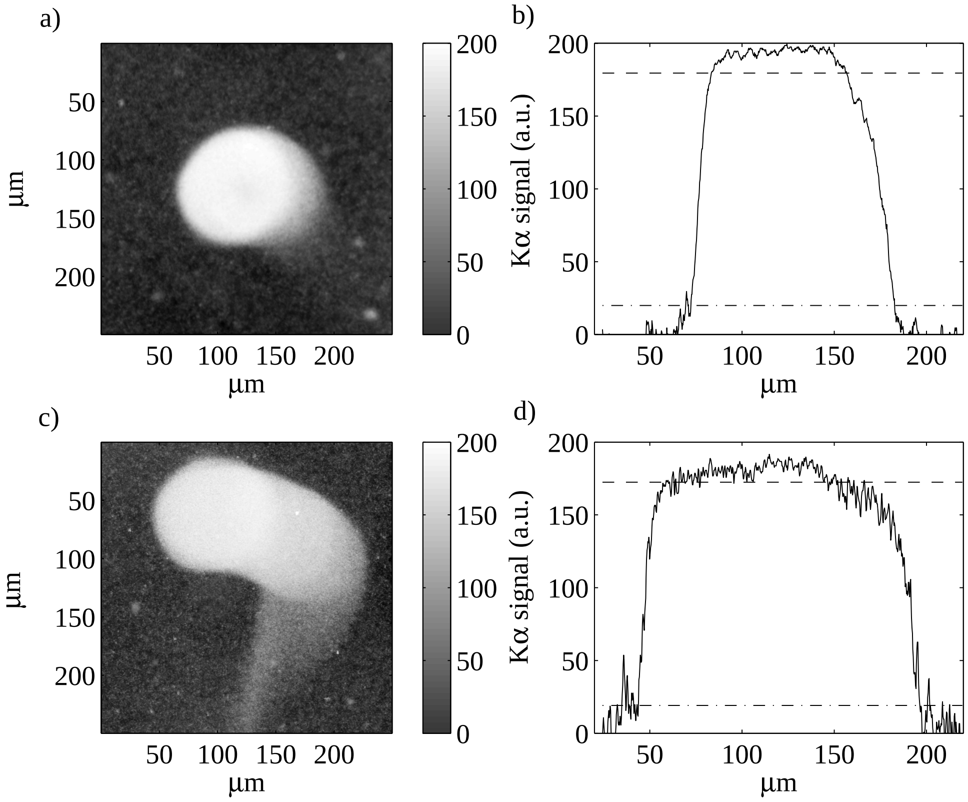

Figure 2.7: X-ray images of a 100 μm pinhole measured with a magnification of 5.7. a) Without azimuthal error. c) With an azimuth angle of 0.8° corresponding to the experimental situation for the imaging of the frontside emission from the plasma source. b) and d) Corresponding horizontal profiles. The horizontal lines mark 10% and 90% of the maximum intensity. Distances refer to distances on the object.

aperture of 5 mm in front of the crystals was used.

For a 5 μm pinhole these aberrations add up to two tails perpendicular to each other and several times larger than the pinhole (Fig. 2.6). The halfwidth (FWHM) of the image is a little widened (1.5 - 2×) compared to the original pinhole size and the sharpness of the pinhole edge is gone. The edge, defined as the length over which the measured intensity drops from 90% to 10% of its peak value, is about $5 - 10$ μm.

For larger pinholes the tails vanish. The pinhole size (its FWHM) is roughly preserved and the edges are ~ 10 μm. These features are relatively independent of the actual pinhole size and the focusing of the crystal, as ray-tracing studies for a 30 μm pinhole and imaging tests with a 100 μm pinhole (Fig. 2.7,a and b) showed. Only when the imaging crystal is defocused $\gtrsim 300$ μm the edges broaden to ~ 20 μm.

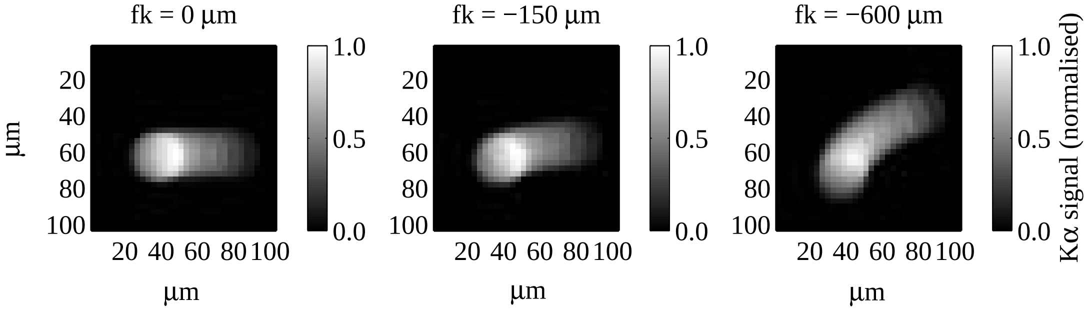

Figure 2.8: X-ray images of a 30 μm pinhole for different defocus distances of the crystal, f_k, calculated with ray tracing. The magnification is 7 and the azimuth angle is 0.9° as it was in the experiment for frontside imaging. Distances refer to distances on the object.

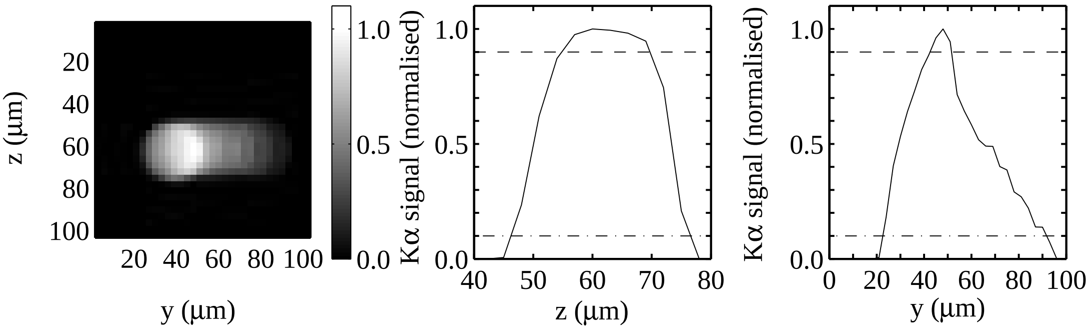

Figure 2.9: X-ray image of a 30 μm pinhole for a magnification of 7 and an azimuth angle of 0.9°, calculated with ray tracing. The horizontal lines mark 10% and 90% of the maximum intensity.

The azimuth angles of the imaging crystals were optically adjusted. After the experiments the adjustment of the crystals was checked at a Ti x-ray tube and for the frontside crystal an azimuth angle of 0.9° was found. Therefore the influence of such an azimuth angle on the x-ray image was also examined. Fig. 2.7,b) shows the image of the same 100 μm pinhole as in Fig. 2.7,a) but with an azimuth angle of 0.8°. On three sides the edge size is still $\approx$ 10 μm and the vertical FWHM is preserved. But in the direction of the aberrations (parallel to the dispersion plane towards higher Bragg angles) a curved tail with high intensity appears which is as large as the pinhole itself.

This curvature of the tail is due to a defocused crystal. In the optimal focal distance, f_k, the tail stays straight horizontally (Fig. 2.8). For a defocusing of $f_k = -150$ μm the curvature appears. And for a defocusing of $f_k = -600$ μm the image has turned into the diagonal direction. Defocusing the crystal into the other direction ($f_k > 0$) turns the image into the opposite diagonal.

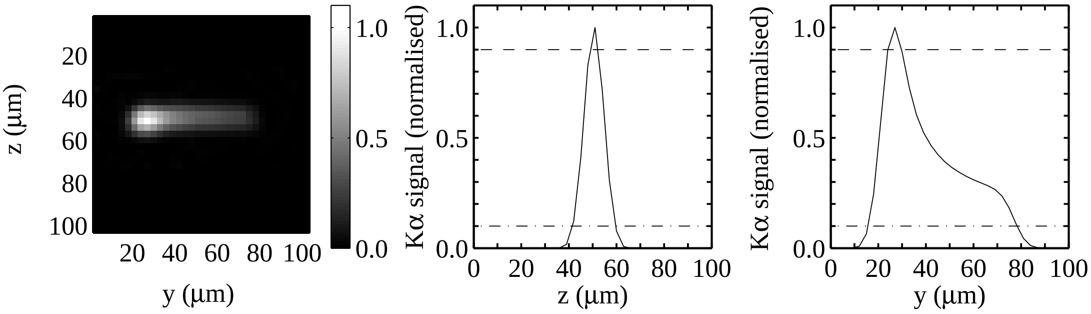

Figure 2.10: Image of a Ti Kα source with a Gaussian shape and a FWHM of 10 μm, calculated with ray tracing. The magnification is 7 and the azimuth angle is 0.9°.

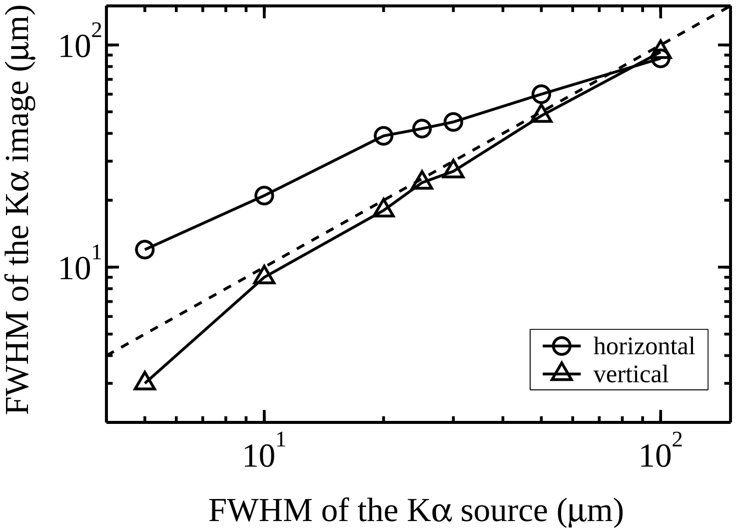

Figure 2.11: Halfwidth (FWHM) of the image of a Kα source with a Gaussian shape, calculated with ray tracing. For the dotted line the halfwidths of the source and the image are equal. Due to aberrations the halfwidth of the image in the horizontal direction is significantly broadened compared to that of the Kα source. The vertical halfwidth of the image is similar to that of the source. The magnification is 7 and the azimuth angle is 0.9°.

For the optimum crystal position f_k (Fig. 2.9) the vertical profile of the x-ray image is little changed by the presence of a non-zero azimuth angle but in the horizontal direction any resemblance to a pinhole has vanished. Instead a cone-like structure with large asymmetrical edges is seen.

The experimental Kα emission does not have a sharp edge, but the intensity decreases continuously towards the borders. To study the influence of aberrations in this case, a number of ray-tracing calculations (including an azimuth angle of 0.9°) were performed for an x-ray source with a Gaussian shape. It was found that the vertical profiles of the

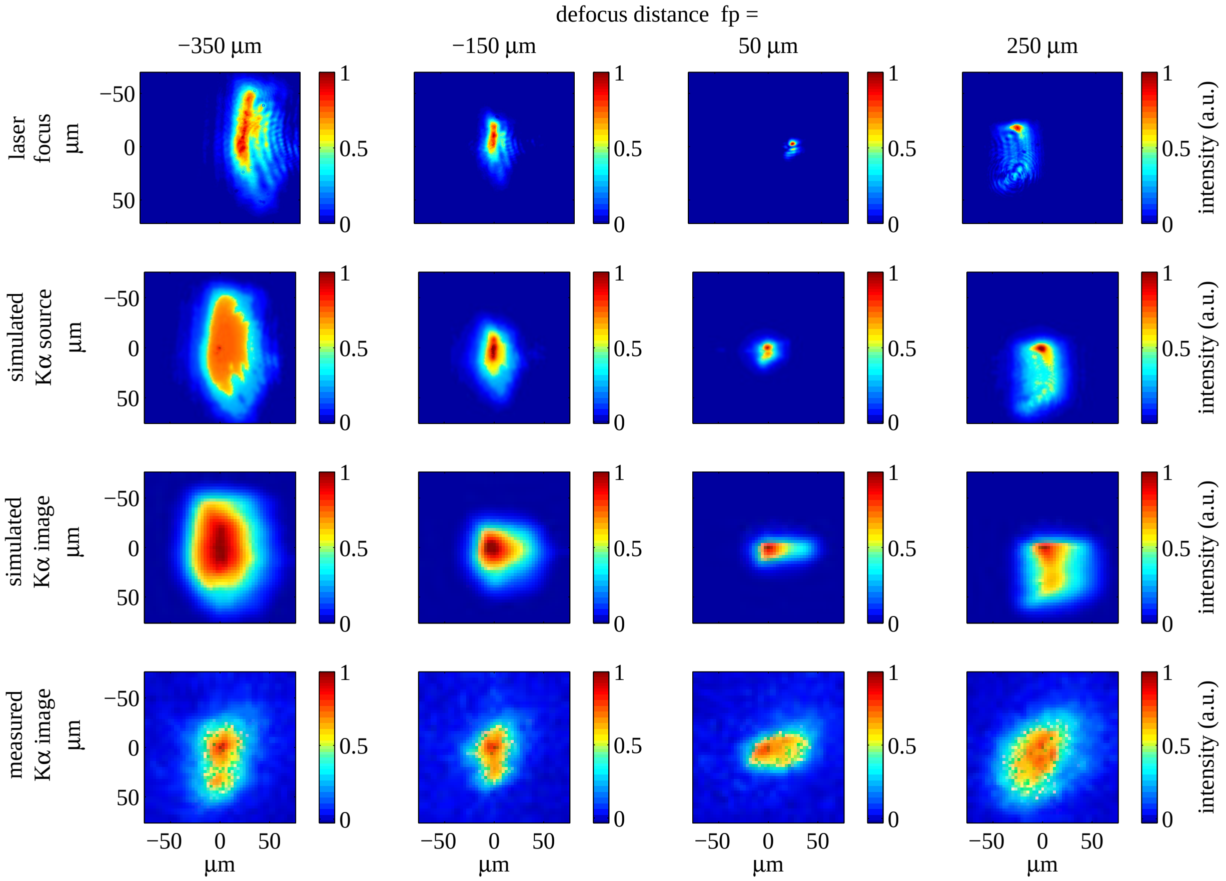

Figure 2.12: Influence of aberrations on the measured Kα images for different distances f_p of the target from the best laser focus. For small Kα sources ($f_p = 50\ \mu$m) the horizontal orientation of the image is largely due to aberrations and not a property of the Kα source itself. For large defocus distances ($f_p = -350/+250\ \mu$m) the vertical orientation of the laser focus is reproduced in the Kα images.

image and the source are very similar (Fig. 2.10). But in the horizontal direction there is again a tail which appears in the profile as a shoulder beside the main peak. Due to this shoulder the image of a small Gaussian Kα source is considerably broadened horizontally (Fig. 2.11). With increasing source size the relative size of the shoulder decreases and for Gaussian sources larger than $\sim 60\ \mu$m also the horizontal profile of the image is similar to that of the source.

In the experiment the Kα emission from the laser-irradiated Ti was imaged for different defocus distances, f_p, implying different sizes of the Kα source. In Fig. 2.12 four measured images from such a defocus series are given and the derivation of the corresponding simulated images (Section 1.4) is illustrated: From the experimental laser profiles (Section 2.3) first, the intensity distribution of the Kα source is calculated with the PIC-MC model and than via ray-tracing that of the image, assuming ideal source-to-crystal and crystal-to-object distances. The experimental images of the series were taken at 200 μm steps in defocus distance, the measured laser beam profiles, and thus the simulated Kα emissions, were 50 μm apart from each other. The best overall agreement between simulation and experiment is found when the experimental 'best focus position' is identified with a defocus distance $f_p = +50$ μm, and the other images accordingly with distances $f_p = -350$ μm, -150 μm and +250 μm. For this assumption the corresponding images of the experimental and the numerical series are shown in the figure.

The measured change in the shape of the Kα intensity distribution, when the laser is defocused, is well reproduced by the simulations. The influence of aberrations on the images can be identified by comparing the calculated intensity distributions before and after the imaging process, i.e. the calculated Kα *source* with the calculated Kα *image*. As was found in the ray-tracing calculations for Gaussian sources, the horizontal orientation of the image for a small Kα source ($f_p = 50$ μm) is largely due to aberrations and not a property of the source itself. On the other hand, the aberrations have little influence on the vertical extension of the image. For larger defocus distances ($f_p = -350/+250$ μm) the vertical orientation of the laser focus is reproduced in the Kα images.

In summary, the careful determination of the crystal adjustment and the laser parameters, in particular its two-dimensional intensity distribution, makes it possible to reproduce the experimental processes by the numerical calculations. Close to best focus, the applied imaging technique reaches its limit in measuring the horizontal extension of the Kα emission because the aberrations become much larger than the emission itself.

In the following chapter the total yield of the Kα emission will be discussed before we return to the spatial structure of the emission in Chapter 4.

Chapter 3

Optimization of Kα Yield

This chapter discusses how the Kα yield from a laser plasma source can be maximized simply by optimizing the laser intensity. The intensity of a laser beam I on the target surface is given by

$$I = \frac{E_{laser}}{\tau_l\, A}\,, \tag{3.1}$$

where E_{laser} is the energy delivered on the target, A is the irradiated area and τ_l is the duration of the laser pulse. Increasing the laser energy gives an equal increase of the laser intensity and, if we assume that the fraction of laser energy transfered into hot electrons is independent of the laser intensity,[1] also an equal increase of hot electron energy. The increase in hot electron energy is partly due to a higher number of electrons being accelerated by the laser and partly due to the electrons acquiring higher energies, which means a higher 'temperature' of the hot electron distribution. Thus, more hot electrons have energies above the K-shell ionization energy of the solid and more Kα photons are produced. Increasing the laser energy gives an increase in Kα yield.[2] On the other hand, increasing either the irradiated target area (by defocusing the laser) or the pulse duration (by changing the compressor grating separation) reduces the laser intensity without changing the energy on the target and thus, leaves the hot electron energy constant.[3] Both actions reduce together with the laser intensity the hot electron temperature but they also increase the number of hot electrons due to a greater irradiated target area or to a longer interaction time of the laser with the plasma. The total hot electron energy remains the same, the energy distribution changes. The consequence is that the Kα yield *can* increase when the laser is defocused or prolonged. This complex situation is analyzed in the following

---

[1] PIC simulations give a roughly constant energy conversion into hot electrons between 40% for $I = 10^{15}$ W/cm^2 and 60% for $I = 10^{19}$ W/cm^2.

[2] A conclusion which is confirmed by own experience and many other experimentalists. See for example [47, 98, 101]. Anyway, it does *not* imply that the yield *per energy* also increases with increasing laser energy.

[3] The assumption of a constant energy conversion into hot electrons holds only for laser pulse durations for which a constant plasma density gradient can be assumed [79].

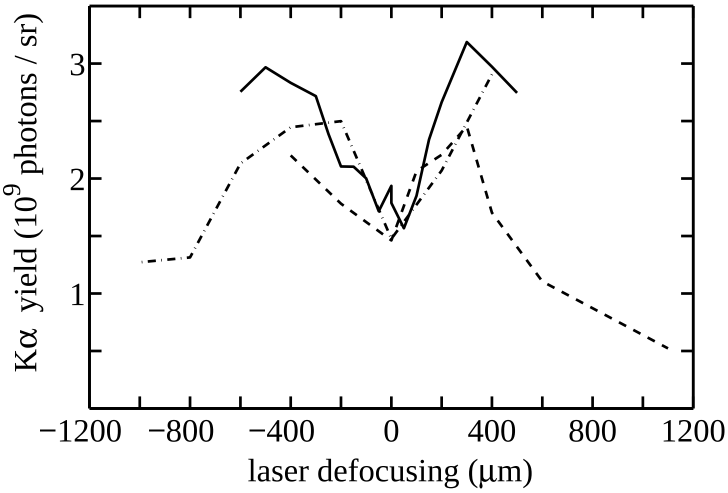

Figure 3.1: Total Kα yield from the frontside of Ti targets. Defocusing the laser by ~ 400 μm increases the Kα yield by a factor of ~ 2. The three curves correspond to measurements on different days.

sections.

3.1 Experimental Results

The effect of defocusing the laser to a lower intensity was investigated experimentally for Ti as target material (Fig. 3.1). The experimental details were given in Chapter 2. The Kα yield from the target frontside increases ~ 2 times when the laser is defocused several hundred microns. With more defocusing the yield decreases again. Using Fig. 2.4 to find the laser intensities which correspond to the defocus distances in Fig. 3.1 we see that the increase in Kα yield corresponds to a decrease of the laser intensity by two orders of magnitude from 7×10^{18} to $\sim 5 \times 10^{16}$ W/cm^2.

In the literature a number of further experiments can be found where the Kα yield was measured as a function of laser intensity. They are summarized in Fig. 3.2 where the yields are normalised to steradiant and a laser energy of 100 mJ. The measurement by Eder et al. [25] and another one by Morak et al. [60] (on Si, not shown in the figure) were also defocusing experiments. They both give a maximum in Kα yield for a laser intensity defocused more than an order of magnitude from its peak value. The original yield data of the measurements show in both cases a structure similar to Fig. 3.1 with symmetrical maxima for defocus positions of several hundred microns. In a measurement by Guo

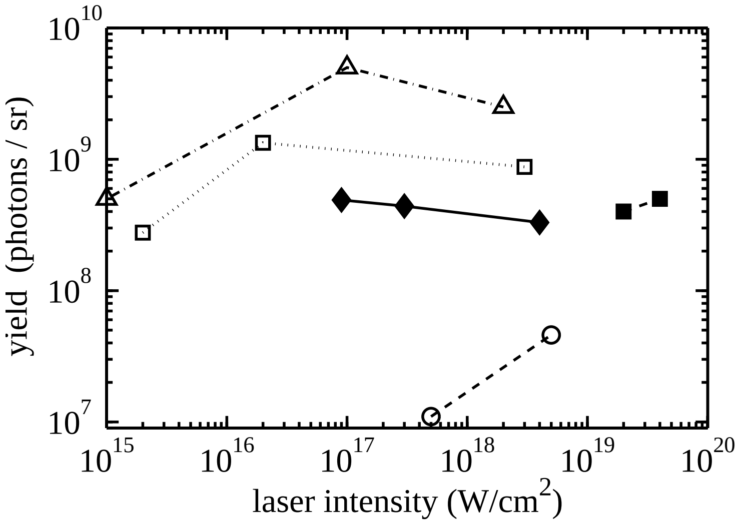

Figure 3.2: Experimental Kα yields for a laser energy of 100 mJ: ◆: Al, Jiang et al. [47]; □: Ti, the present work; △: Cu, Eder et al. [25]; ■: Mo, Wharton et al. [98]; ○: Ag, Yu et al. [101].

et al. [41] (not shown in the figure) the laser intensity was reduced from a maximum of 10^{18} W/cm^2 by increasing the pulse duration. The result was also an increase in Cu Kα yield . In the other experiments the laser intensity was varied by changing the laser energy or by changing both the energy and the focus. Fig. 3.2 shows that the findings for Ti can only partly be generalized: For the lighter elements (Al, Si, Ti and Cu) the Kα yields are higher for lower (or medium) laser intensities, but for the heavier ones (Mo and Ag) higher Kα yields are related to higher laser intensities.

It should be pointed out that the decrease of Kα yield with increasing laser intensity in the experiment by Jiang et al. [47] is only due to normalizing the yield to a constant laser energy. In the experiment itself the intensity was increased by increasing the laser energy. Thus, the graph given in the original paper shows a monotonic increase of absolute Kα photon number with increasing laser intensity – in agreement with the introduction of this Chapter.

The absolute photon numbers in Fig. 3.2 should be regarded with care. Table 3.1 gives an overview over experimental Kα yields found in the literature. The values are again normalised to steradiant and a laser energy of 100 mJ. The table shows how strongly the measured Kα yields can vary even for apparently similar experimental conditions. Among the reasons are: substitution of the intensity distribution in the laser focus by a nominal

Target	$E_{K\alpha}$ (keV)	I $\left(\frac{\text{W}}{\text{cm}^2}\right)$	Kα yield $\left(\frac{10^9\,\text{ph}}{100\text{ mJ sr}}\right)$	Reference
Al	1.5	3×10^{16}	1.7	Rousse et al. [74]
		9×10^{16}	0.5	Jiang et al. [47]
		3×10^{17}	0.4	”
		2×10^{18}	0.4	”
		4×10^{18}	0.3	”
Si	1.7	4×10^{15}	1.2	Soom et al. [87]
		3×10^{17}	0.2	Feurer et al. [31]
		5×10^{17}	4.2	Ziener et al. [103]
SiO_2	1.7	4×10^{16}	0.4	Schlegel et al. [79]
		4×10^{16}	2.5	”
Ca	3.7	3×10^{16}	1.0	Rousse et al. [74]
Ti	4.5	5×10^{15}	1.4	Wharton et al. [97]
		3×10^{16}	2.7	Rousse et al. [75]
		5×10^{17}	1.3	Ziener et al. [103]
		2×10^{16}	1.3	the present work
		3×10^{18}	0.9	”
Fe	6.4	3×10^{16}	0.5	Rousse et al. [74]
Co	6.9	5×10^{17}	0.5	Ziener et al. [103]
Ni	7.5	2×10^{18}	8.0	Pretzler et al. [66]
Cu	8.4	1×10^{15}	0.5	Eder et al. [25]
		1×10^{17}	5.0	”
		2×10^{18}	2.5	”
		1×10^{18}	8.0	Guo et al. [41]
Mo	17.5	2×10^{19}	0.4	Wharton et al. [98]
		4×10^{19}	0.5	”
Ag	22.2	5×10^{17}	0.01	Yu et al. [101]
		5×10^{18}	0.05	”
Sn	25.3	4×10^{17}	0.004	Anderson et al. [3]
Ta	57.5	4×10^{17}	0.008	Anderson et al. [3]

Table 3.1: Experimental Kα photon yields as given in the literature. The yields are normalised for a laser energy of 100 mJ.

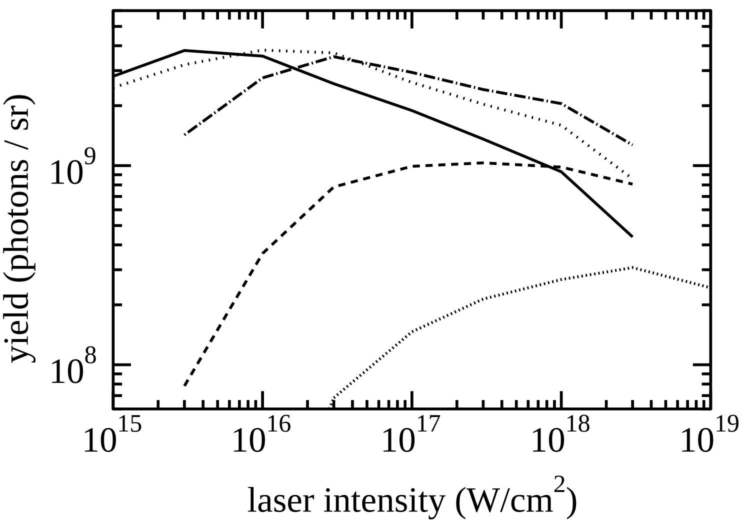

Figure 3.3: Simulated Kα yields from bulk targets for a laser energy of 100 mJ: Si (solid), Ti (wide dots), Cu (dash-dotted), Ag (dashed) and Ta (narrow dots).

value, difficulties in calibrating the Kα signal and the influence of experimental details like the laser incidence angle and the plasma density profile. For example, SCHLEGEL et al. [79] achieved a sixfold increase in Kα yield only by variation of the density scale length.

3.2 Numerical Results

Inspection of Fig. 3.2 leaves two questions open: 1) Is there also an optimal laser intensity for Kα production for other target elements? and 2) Where is it? To answer these questions combined PIC-MC calculations were performed for laser intensities varying over four orders of magnitude and target elements ranging from Si ($Z = 14$) to Ta ($Z = 73$). In these simulations, the laser energy was kept constant (at 100 mJ), which corresponds to the situation in a defocusing experiment. For simplicity, it was assumed that the focal spot was homogeneously irradiated at a single laser intensity. Thus, the irradiated target area was reciprocal to the laser intensity, $A \propto I^{-1}$. The laser pulse duration τ_l was chosen as 60 fs, the incidence angle of the laser as 45°, the plasma scale length L/λ as 0.3 and the maximum electron density $n_e(max)$ in the PIC simulations as ten times the critical density n_c.

The simulated Kα yields are shown in Fig. 3.3. They are mainly in the range 0.2–4 (in units of 10^9 photons per steradiant and 100 mJ laser energy). Except for the high

Z elements Ag, Sn and Ta, the measured Kα yields (table 3.1) from all target materials and under all the different experimental conditions are between 0.2 and 8. Thus, the simulations are in reasonable agreement with the experimental findings.[4]

Now turning to the questions posed at the beginning of the section, we find three striking features in Fig. 3.3:

1. For each element there is a laser intensity I_{opt} which gives maximum Kα yield (in agreement with the experimental observations).
2. The higher the atomic number of the target, the higher is the optimal laser intensity.
3. The curves cross each other! At lower laser intensities the Kα yield from the lighter elements is higher, while at higher intensities, it is higher from the heavier ones.

It was the last point that inspired the following analysis. How can it be that a given distribution of hot electrons produces more Kα photons in targets with higher Z? In these elements the cross section for ionization of the K shell is smaller than in lighter ones [15, 46] *and* the electron path length is shorter because of the higher stopping power. So the number of generated Kα photons decreases with increasing atomic number.

In the following section an analyical model for the generation of Kα radiation is presented and the explanation for the existence of the yield maximum, its Z-dependence and the crossing of the yield curves is given.

---

[4] Though the Monte Carlo code underestimates Kα yields from high Z elements (Section 1.2.7) the experimental yields are even lower than the calculated ones.

3.3 The Analytical Model

3.3.1 Analytical Model for Kα Yield

Analytically, the Kα yield from a hot electron distribution penetrating into a solid can be expressed as an energy integral over the properties of monoenergetic electrons

$$N(I,Z) = \int n_{hot}(I)\, f_{hot}(I,E)\, N_{gen}(E,Z)\, f_{em}(E,Z)\, dE, \tag{3.2}$$

where

- $N(I,Z)$ is the number of emitted Kα photons when a target element of atomic number Z is irradiated at a laser intensity I,
- $n_{hot}(I)$ is the total number of generated hot electrons and
- $f_{hot}(I,E)$ is their energy distribution;
- $N_{gen}(E,Z)$ is the number of Kα photons generated by a single electron of incidence energy E in the element Z, and
- $f_{em}(E,Z)$ is the fraction of these photons that escape from the solid — the '*emission factor*'.

The evaluation of the integral was performed in three steps:

1. PIC and Monte Carlo simulations were performed to derive a data base.
2. The simulation results were parametrized to achieve analytical expressions for $n_{hot}(I)$, $f_{hot}(I,E)$ and $N_{gen}(E,Z)$.
3. The analysis of the emission factor, which is deferred to Section 3.3.2. It will be shown that f_{em} only enters the final expression by defining the upper integration limit.

For $n_{hot}(I)$ and $f_{hot}(I,E)$ analytical expressions were derived from fits to the results of PIC simulations for a range of laser intensities using the parameters given in Section 1.3. We found that f_{hot} is best fitted with a one-dimensional Maxwellian energy distribution [56]

$$f(E)\, dE = \frac{1}{\sqrt{E\, kT}} \exp\left(-\frac{E}{kT}\right) dE, \tag{3.3}$$

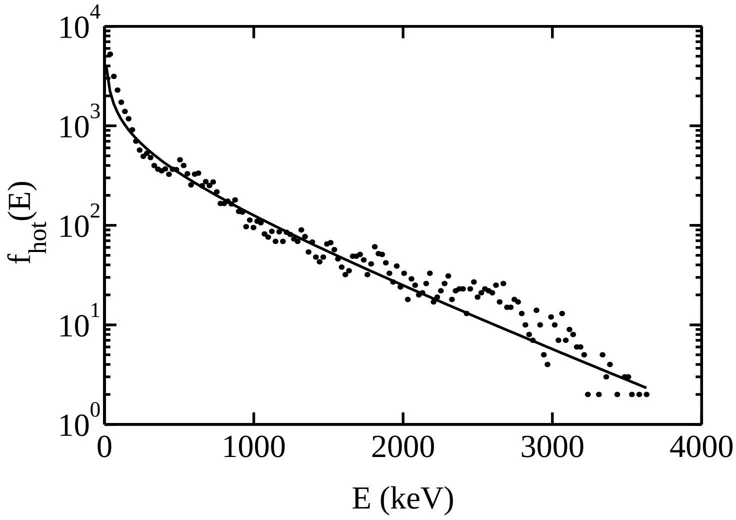

Figure 3.4: Energy distribution $f_{hot}(E)$ of the hot electrons from a PIC simulation for a laser intensity of 3×10^{18} W/cm^2. The solid line is a fit of the distribution according to Eq. (3.3) with an electron temperature of $kT = 780$ keV.

which is illustrated in Fig. 3.4 for the hot electrons from a PIC simulation with a laser intensity of 3×10^{18} W/cm^2.[5]

From the PIC results we find a temperature scaling with laser intensity I as

$$kT \approx 130\,\mathrm{keV}\,\sqrt{\frac{I}{10^{17}\,\mathrm{Wcm^{-2}}}}, \tag{3.4}$$

while the number of generated electrons scales as

$$n_{hot}(I) \approx 4.8 \times 10^{19}\, I^{-1/2}. \tag{3.5}$$

This expression takes into account the decrease of irradiated surface area $\propto I^{-1}$ with increasing laser intensity when the laser energy is kept constant. The total energy of the hot electrons is given by $\int n_{hot}\, f_{hot}(E)\, E\, dE$ with (3.4) for the hot electron temperature. This integral is *independent* of the laser intensity, consistent with the PIC simulations

---

[5] Hot electron distributions similar to that in Fig. 3.4 were found in PIC simulations and experiments by other groups. Often they are described as 'bi-Maxwellian', i.e. consisting of two distributions $f_{hot} \propto \exp(-E/kT)$ with two different temperatures kT for the high- and the low-energy electrons [26, 53, 54, 66]. Eq. (3.3) was chosen to describe f_{hot} because it comprises both parts of the electron spectrum. This choice is purely heuristical. From theory, there is not even an intrinsic reason why the electron distribution should be Maxwellian.

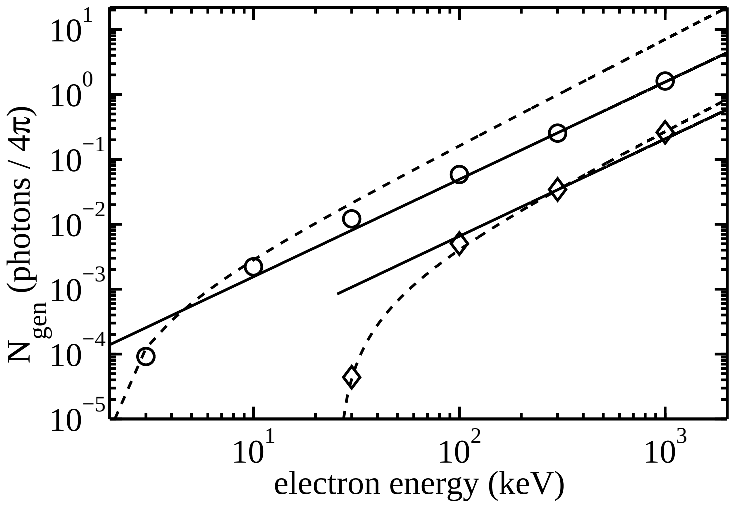

Figure 3.5: Number of generated Kα photons: Comparison of Eq. (3.6) used in the present work (solid) and Eq. (3.7) given by Green and Cosslett [39] (dashed) with the results from Monte Carlo simulations for Si (◯) and Ag (◇).

which give a roughly constant (40 – 60%) energy conversion into hot electrons over the range considered here.[6]

An analytical expression was derived for $N_{gen}(E, Z)$ from fits to the results of Monte Carlo simulations using monoenergetic electrons:

$$N_{gen}(E, Z) = 4 \times 10^{-3}\, Z^{-5/3}\, E^{3/2}. \tag{3.6}$$

This expression was chosen to achieve an analytical solution of the integral in Eq. (3.2). Obviously, the formula given in the classical paper by Green and Cosslett [39] is not suitable for this purpose:

$$\begin{aligned} N_{gen} &= K_0\,(E - E_K)^{1.63} \quad \text{with} \\ K_0 &= 10^{-3.444-0.0426Z}. \end{aligned} \tag{3.7}$$

Fig. 3.5 gives a comparison of both formulas with the results of Monte Carlo simulations for Si ($Z = 14$) and Ag ($Z = 47$), which define the edges of the range of target elements investigated by Green and Cosslett. In general, Eq. (3.6) gives satisfactory agreement

---

[6] These results are in agreement with the literature which gives a temperature scaling $kT \propto I^\alpha$ with $\alpha = \frac{1}{3} \cdots \frac{1}{2}$, found theoretically and in experiments [37]. For the energy conversion into hot electrons values between 0.1 % and 50 % are found experimentally [30].

with the simulation data, though it drastically overestimates Kα generation at low energies.[7] This is the energy range originally investigated by Green and Cosslett ($E \leq 50$ keV) and here their formula agrees excellently with the data.[8]

Inserting (3.3)–(3.6) into Eq. (3.2) and including a factor $1/4\pi$ gives

$$N(I, Z) = \int 3.0 \times 10^{20} \frac{Z^{-5/3}}{I^{3/4}} E \exp\left(-\frac{E}{kT}\right) f_{em}(E, Z)\, dE. \tag{3.8}$$

for the number of Kα photons emitted per steradian. In the following section, the emission factor f_{em} is analyzed and the integral is solved.

3.3.2 Self Similarity of Kα Reabsorption

Monte Carlo simulations using monoenergetic electrons demonstrate that the electron penetration into the solid shows a *universal behaviour* with respect to the incident electron energy normalised to the K-shell ionization energy of the target

$$U = \frac{E}{E_K}. \tag{3.9}$$

At $U = 20$, the mean depth of Kα generation in the target is comparable to the absorption length for self-emitted Kα radiation (Fig. 3.6), so that for $U < 20$ most of the generated photons can escape from the target. For $U > 20$, the electron penetration depth and reabsorption both increase, so that f_{em} falls off rapidly.

This behaviour of the emission factor (Fig. 3.7) is similar to the typical response of a low-pass filter and can be analytically described by

$$f_{em} = \frac{1}{1 + \left(\frac{U}{U_0}\right)^z}. \tag{3.10}$$

A fit to the data of the six target elements shown in Fig. 3.7 gives $U_0 \approx 17$ and $z = 1.67 = 5/3$. At $U = 20$, one has $f_{em} \approx 0.4$.

To facilitate the integration of Eq. (3.2), in the following analysis the emission factor was approximated by a step function

$$f_{em} = \begin{cases} 1 & : \quad U \leq 20 \\ 0 & : \quad U > 20. \end{cases} \tag{3.11}$$

---

[7] The influence of this inaccuracy is discussed together with Fig. 3.8.

[8] The 'deviation at high energies' at Si was already noticed by Green and Cosslett.

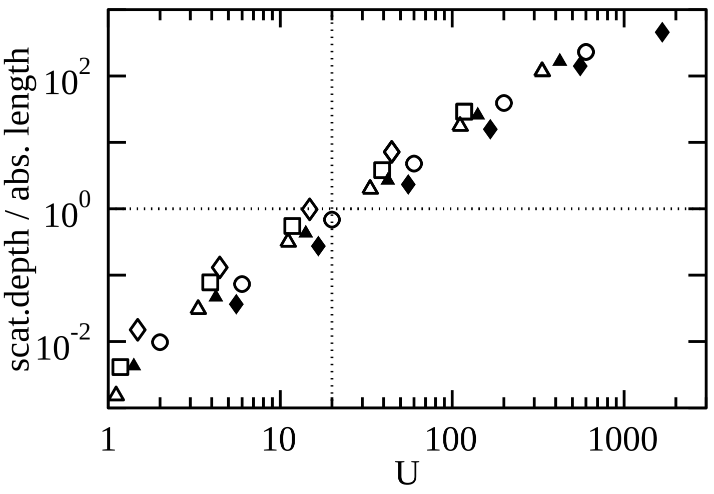

Figure 3.6: Self similarity of electron penetration into solids: Ratio of mean depth of Kα generation to absorption length versus $U = E/E_K$. ♦: Si; ◯: Ti; ▲: Fe; △: Cu; □: Ag; ◇: Ta. For $U = 20$, the mean generation depth has the same order of magnitude as the absorption length for own Kα radiation (dotted lines).

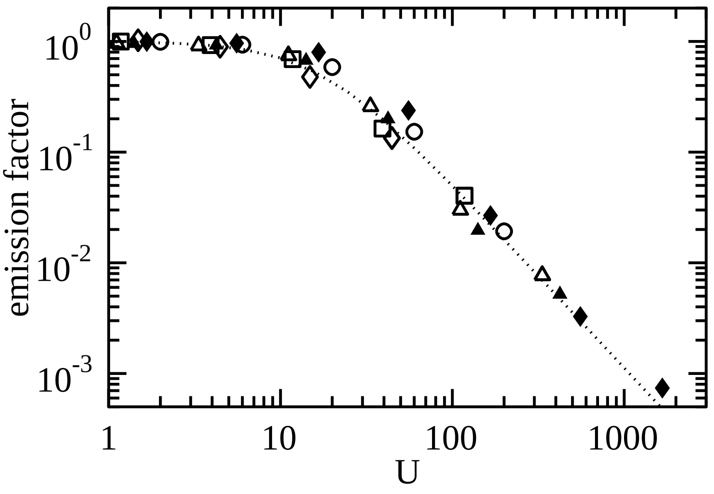

Figure 3.7: The emission factor f_{em} of monoenergetic electrons versus $U = E/E_K$. ♦: Si; ◯: Ti; ▲: Fe; △: Cu; □: Ag; ◇: Ta. Dotted line: the fit according to Eq. (3.10).

The ionization energies were fitted with[9]

$$E_K \approx 0.0054\, Z^{2.2}. \tag{3.12}$$

With (3.12) and (3.9) to substitute E and dE and applying (3.4) for kT Eq. (3.8) finally

---

[9] Eq. (3.12) is slightly different from Eq. (A.7) given by Casnati et al. [15].

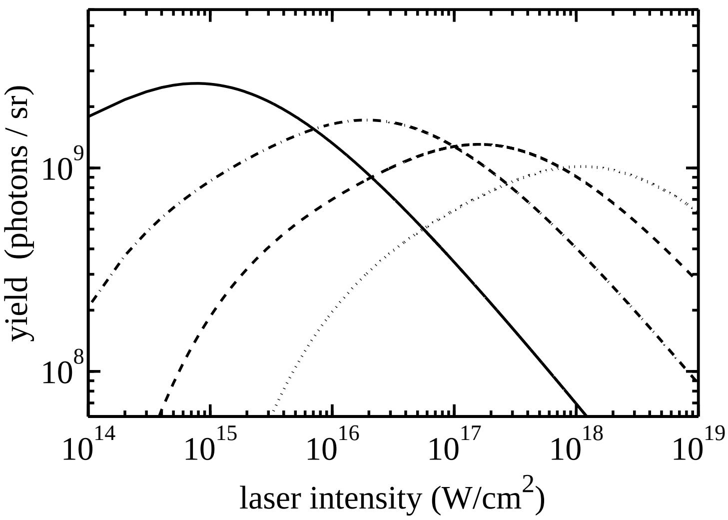

Figure 3.8: Kα yields according to Eq. 3.14: Si (solid), Cu (dash-dotted), Ag (dashed) and Ta (narrow dots).

becomes

$$N(I,Z) = 8.7 \times 10^{15}\,\frac{Z^{2.73}}{I^{3/4}} \int_{1}^{20} U \,\exp\left(-\frac{1.3\times 10^4\, Z^{2.2}}{I^{1/2}}\, U\right) dU \tag{3.13}$$

with the lower integration limit $U = 1$, because the electron energy must be at least E_K to generate Kα radiation. Solving the integral gives a simple expression for the Kα yield:

$$N(I,Z) = \\ 5.0\times 10^{7}\,\frac{I^{1/4}}{Z^{1.67}}\left[-\left(\frac{1.3\times 10^4\, Z^{2.2}}{I^{1/2}}\, U + 1\right)\exp\left(-\frac{1.3\times 10^4\, Z^{2.2}}{I^{1/2}}\, U\right)\right]_{U=1}^{20} \tag{3.14}$$

Fig. 3.8 illustrates this equation for a number of target elements. The simulated Kα yields in Fig. 3.3 are well reproduced.[10] Especially, the three major features are retained: the existence of a yield maximum for each element, the shift of the maximum with Z and the crossing of the yield curves.

The explanation of these features is the emission factor f_{em}. In calculations with reabsorption numerically 'switched off' the yield maximum vanishes: the Kα yield increases

---

[10] Nevertheless, the simplifications in the analytical model produce some minor differences compared to the simulations: 1) The Kα yields at high laser intensities are lower because of the neglect of electrons with $U > 20$. 2) The yields from Ta are a factor ~3 higher because Eq. 3.6 is particularly inaccurate for this element at low energies (Fig. 3.5). 3) The yield maximum is a little shifted towards lower intensities.

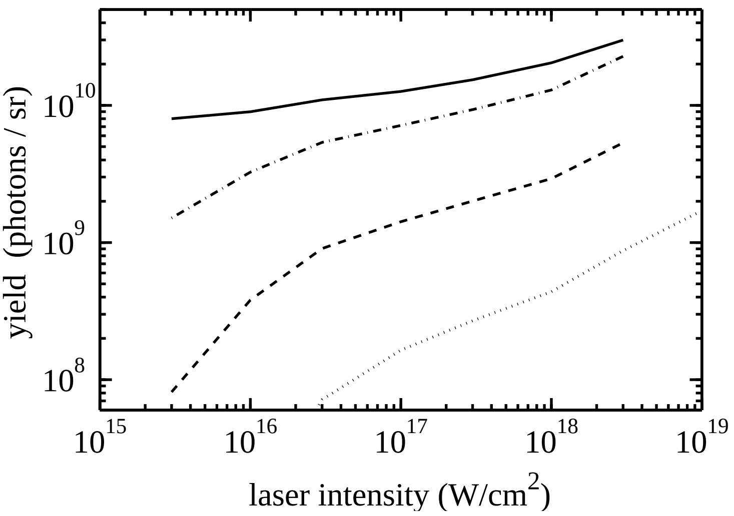

Figure 3.9: Simulated Kα yields with reabsorption numerically 'switched off': Si (solid), Cu (dash-dotted), Ag (dashed) and Ta (narrow dots).

monotonically with higher laser intensities (Fig. 3.9). Also, lighter elements always give higher Kα yields than heavier ones for the same laser intensity. In the analytical model, 'switching off' absorption corresponds to setting the upper integration limit in Eq. (3.14) to infinite, which means that the emission factor is set to $f_{em} = 1$ for all electrons.

3.3.3 Optimal Hot Electron Temperature

The laser intensity I_{opt} with maximum Kα yield for a given target material Z is found by setting the first derivative of Eq. (3.14) to zero, $\partial N/\partial I = 0$. Omitting the lengthy equation, one finds the dependency:

$$I_{opt} = 7 \times 10^9 \; Z^{4.4}. \tag{3.15}$$

This mysterious relation between laser intensity and atomic number can be understood physically by looking at the temperature of the hot electrons, which we normalise again by the K-shell ionization energy:

$$U_{kT} = \frac{kT}{E_K} = 7.6 \times 10^{-5} \frac{\sqrt{I}}{Z^{2.2}}. \tag{3.16}$$

For a given normalised electron temperature U_{kT} Eq. (3.16) implies a fixed ratio $I/Z^{4.4}$. The existence of an optimal laser intensity means in fact that there is an optimal temperature of the hot electrons which produces the most Kα emission. It is found by inserting (3.15)

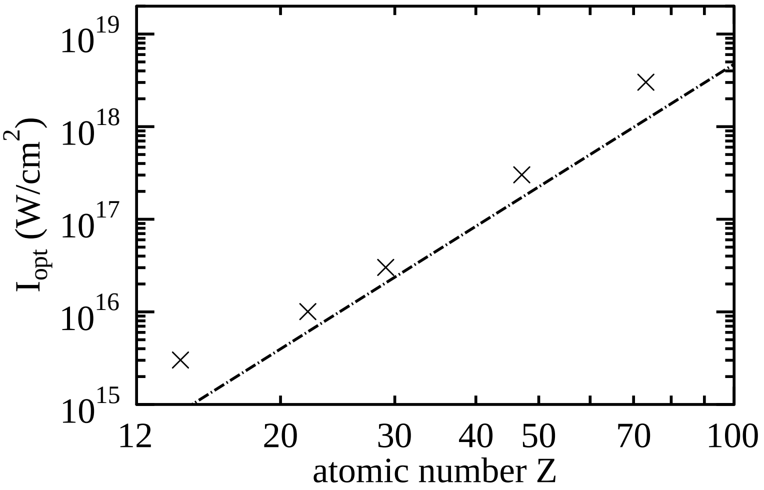

Figure 3.10: Dependence of the optimum laser intensity on the target element. Points are from simulations (Fig. 3.3), the line is from the analytical model – Eq. (3.15).

into (3.16):

$$kT_{opt} = 6.4\,E_K. \tag{3.17}$$

The existence of an optimal electron temperature is explained by the emission factor which limits the Kα emission from high energy electrons. Thus, only hot electrons from a certain energy range contribute to the emission of Kα radiation: electrons with lower energies cannot ionize the K shell of the target atoms while those with higher energies produce the Kα photons too deep inside the target. It was shown in Section 3.3.2 that not only the lower limit of this energy range is related to the K shell's ionization energy but also the upper limit:

$$1 < U \lesssim 20. \tag{3.18}$$

The hot electron distribution with temperature U_{opt} is the distribution with the highest total electron energy in this interval. It also produces the highest Kα emission.[11]

The scaling of the optimal laser intensity, $I_{opt} \propto Z^{4.4}$, results from the combination of two scaling laws. The reference value for Kα production *and* reabsorption is the ionization energy of the K-shell, which gives a scaling of the appropriate hot electron temperature as $kT_{opt} \propto Z^{2.2}$. The laser intensity scales with the hot electron temperature as $I \propto (kT)^2$, giving $I_{opt} \propto Z^{4.4}$. A weaker temperature scaling, e.g. $kT \propto (I\lambda^2)^{1/3}$, would lead to a

---

[11] Section 5.3 will exploit the fact that U_{opt} is also the single electron energy at which the most Kα photons are produced.

correspondingly stronger scaling of I_{opt} with Z.

According to Eq. (3.15), the optimal laser intensity increases with the atomic number of the target material. Fig. 3.10 gives a comparison of the values of I_{opt} from the numerical calculations and Eq. (3.15). The numerical results follow the predicted $Z^{4.4}$ dependence. Their systematic deviation from Eq. (3.15) is explained by the approximations in Eq. (3.6) which, in fact, gives too high yields for low energy electrons and Eq. (3.11) which cuts off the influence of high energy electrons. Both approximations lead to a relative overweighting of low energy electrons and an intensity I_{opt} slightly too low.

The 'crossing of the yield curves' can also be easily understood: Eq. 3.15 gives the relation between laser intensity and target element for which the Kα yield is maximum. Thus, for a given laser intensity I the element with atomic number

$$Z_{max} = 5.4 \times 10^{-3} \, I^{\,0.23} \tag{3.19}$$

gives the highest Kα yield, because the hot electron temperature is optimal for this element. Eq. 3.19 implies a shift of this 'optimal' target element from light elements to heavier ones when the laser intensity is increased. This is the 'crossing of the yield curves'.

Chapter 4

The Spatial Structure of the Kα Emission

This chapter is dedicated to the spatial distribution of the Kα radiation emitted from fs-laser irradiated solids. It starts with the results of the first systematic experimental study of the Kα emission with two-dimensional spatial resolution. As is usually found in the literature, the experiment gives significant deviations from calculated Kα emissions. The differences can be qualitatively explained by an estimate of the self-generated magnetic and electric fields in the experiment. To estimate the penetration depth of the hot electrons related to the frontside Kα emissions the radiation from the target side was also measured.

4.1 Measured Structure of the Kα Emission

In the experiment described in Chapter 2 image series of the Kα emission from the frontside of a Ti target were taken in which the laser was focused and defocused. In the following, it is shown how the distance of the target from the best focus position influences

- the Kα peak emission,
- the halfwidth of the source,
- the total extension of the emission and
- details of the total Kα yield.

The measured features are compared with those from Kα images simulated for the experimental parameters.

When the target is moved from a defocused position towards the best laser focus a number of changes in the emitted Kα radiation occur. The most striking one is that the peak Kα emission drops. In the defocus series in Fig. 4.1 the peak emission within about

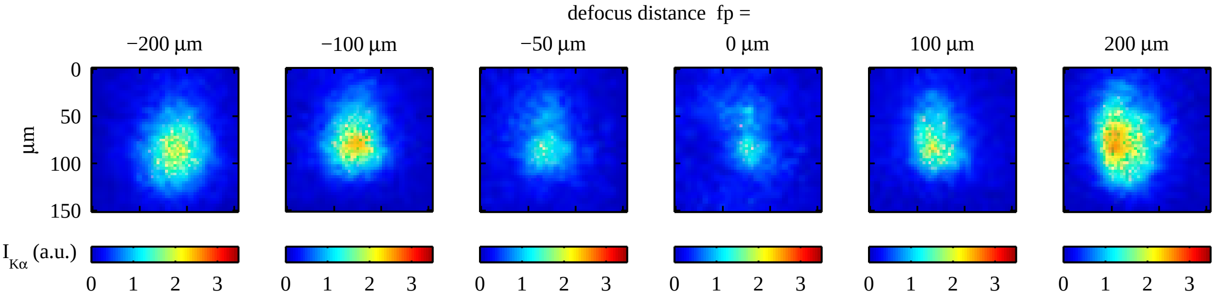

Figure 4.1: Defocus series of the frontside Kα emission. The colour coding is the same for all images. At best focus, $f_p = 0$ μm, the Kα intensity has a local minimum. The image size corresponds to 150×150 μm on the target.

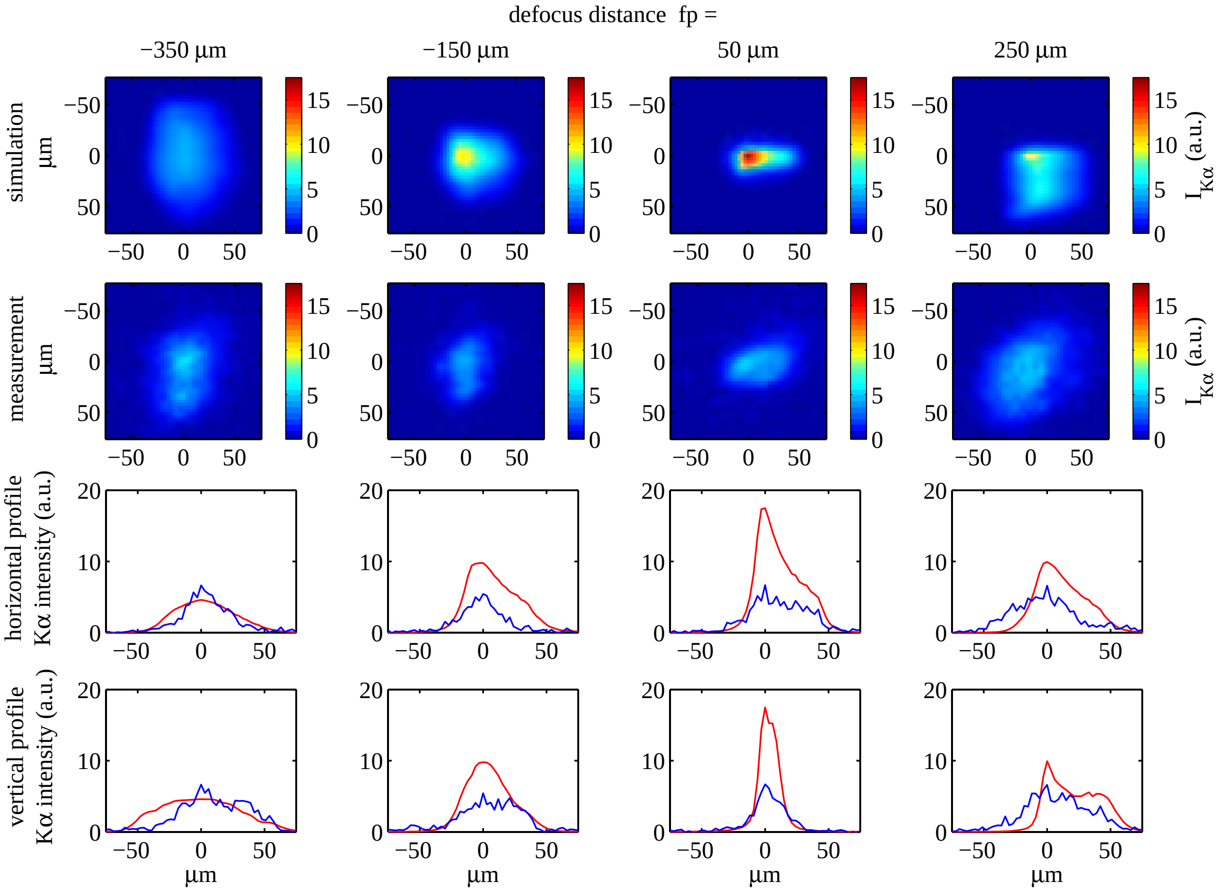

Figure 4.2: Comparison of measured and simulated Kα images for four different defocus distances f_p. The blue profiles correspond to the measured images, the red ones to the simulated ones. The intensities of the simulated images are so normalised that the total Kα yields of the two images at $f_p = -350$ μm are equal.

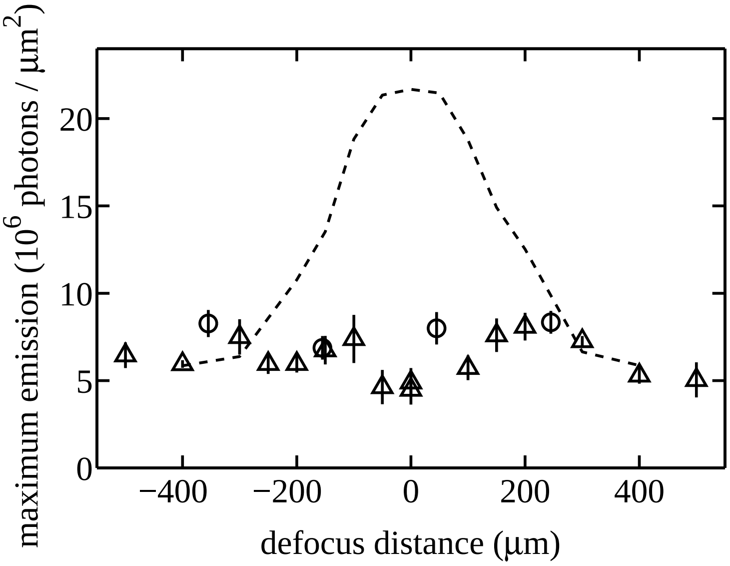

Figure 4.3: Dependence of the peak Kα emission on defocus distance. The symbols correspond to the measured images in Figs. 4.1 (△) and 4.2 (◯). The dashed line gives the simulated values.

75 μm from the best focus is a factor of ~ 2 lower compared to that at a defocus distance of 200 μm.

This behaviour is in strong contrast to simulated Kα images. Fig. 4.2 shows a comparison between a measured defocus series and one that was derived by the four-step simulation procedure described in Section 1.4.[1] In the simulated images the peak Kα emission does not drop when the laser is stronger focused but increases by a factor of 3. The situation is summarized in Fig. 4.3 giving the measured and simulated Kα peak intensities depending on the defocus distance.

In contrast to the Kα *peak* emission being much *lower* than predicted by the simulations the *total* Kα emission at the best focus is even $\sim 60\%$ *higher* than calculated (Fig. 4.4). Thus, a large portion of the Kα emission must be generated outside the central area of the emission.

---

[1] The images are the same as in Fig. 2.12, but with a single normalization for all simulated images. The calculated total Kα yields are about 40% smaller than the measured ones, which means reasonable agreement (see the discussion of Table 3.1). They are so normalised that the images at $f_p = -350$ μm have the same total Kα yield. At this defocus distance the laser intensity is below 10^{16} W/m^2 (Fig. 2.4) where PIC-MC simulations usually show good agreement with experiments (Section 4.2).

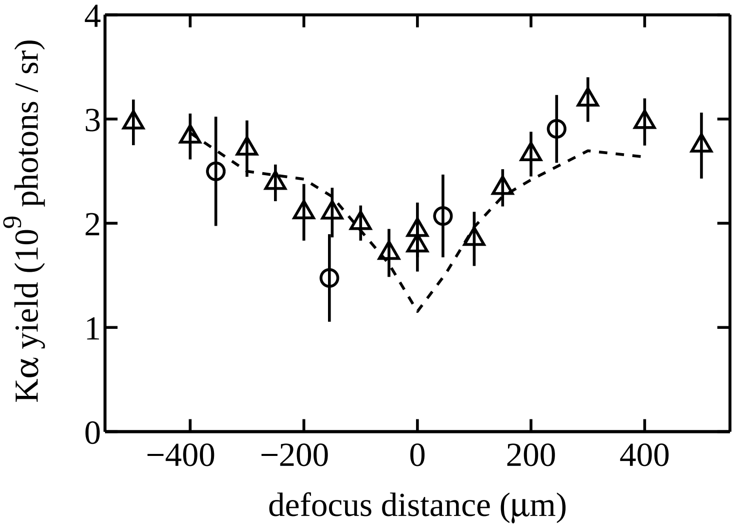

Figure 4.4: Dependence of the total Kα yield on defocus distance. The symbols correspond to the measured images in Figs. 4.1 (△) and 4.2 (◯). The dashed line gives the simulated values.

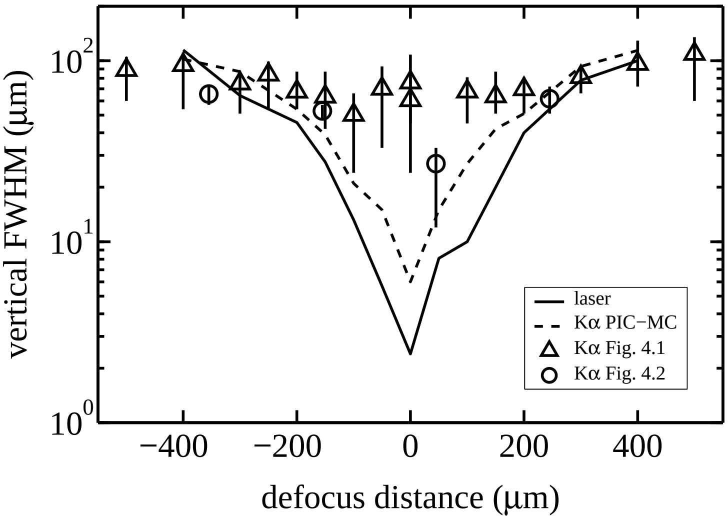

Figure 4.5: Vertical halfwidths of the laser focus, the measured and the simulated Kα emission.

Fig. 4.5 shows the halfwidths of the laser focus and of the experimental Kα emissions together with the calculated values. The figure gives the vertical halfwidths which are practically uninfluenced by aberrations and similar to those of the Kα emission itself (Fig 2.11). At best focus the measured halfwidth is difficult to be estimated because of the strong noise in the images. It is in the range $\sim 25 - 110$ μm with the mean value being ~ 70 μm. This is a factor 28 larger than the vertical halfwidth of the laser focus and a factor 12 larger than calculated. Even for the lower limit of the estimated range the measured halfwidth at

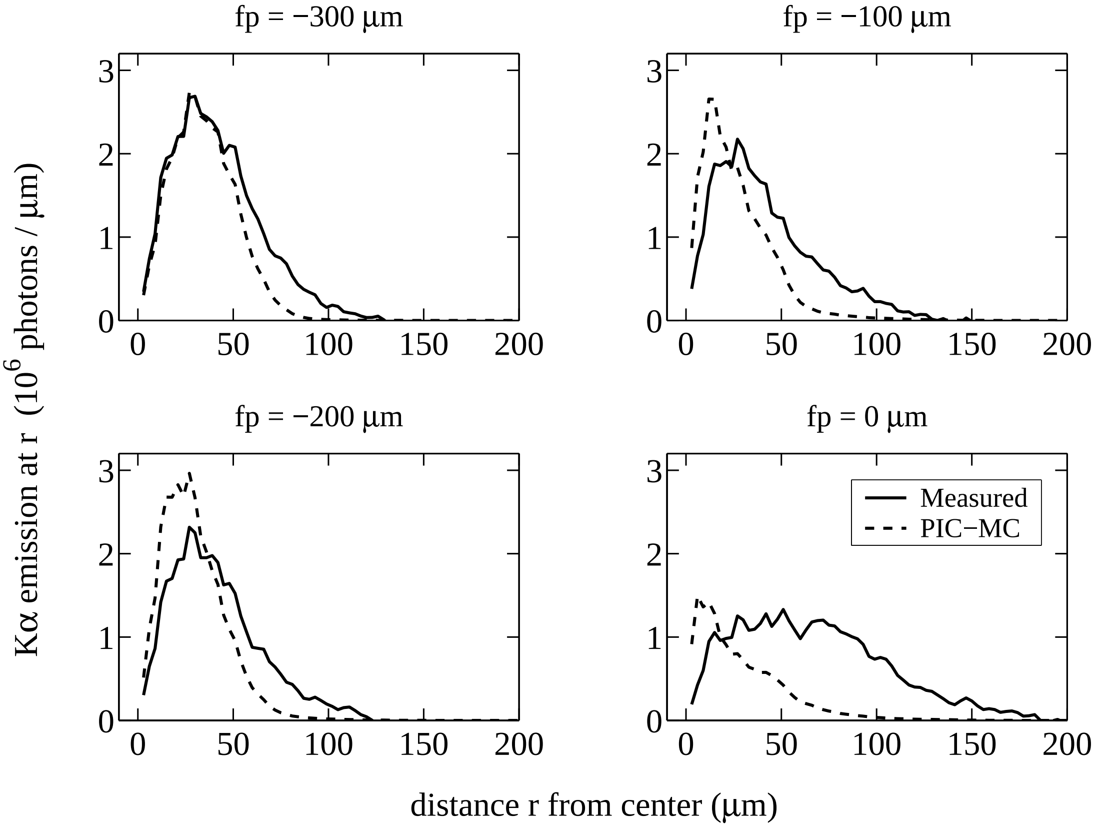

Figure 4.6: Dependence of the Kα emission on the distance r from the focus center for different defocus distances f_p. See text for details.

best focus is a factor 4 larger than calculated. When the laser is defocused, the mesaured halfwidth only increases little. At a defocus distance of 300 μm the halfwidths of the laser focus, the measured and the calculated Kα emission are comparable, for larger defocus distances up to $\sim$ 1 mm the measured size of the Kα emission remains practically constant and is smaller than that of both the laser focus and the calculated emission.[2]

A more comprehensive analysis of *where* the Kα emission comes from is given in Fig. 4.6. It shows how much Kα radiation is emitted at a given distance from the center of the emission, i.e. each value in the figure represents an angular integration over the Kα emission at a fixed radius.[3] For defocus distances of -300/+200 μm the calculated and measured Kα distributions are similar. Closer to the best focus position the distributions become increasingly different. While the calculated emission decreases and shifts towards the

---

[2] For defocus distances greater than 400 μm the laser beam profile was approximated by a Gaussian with a halfwidth of 3 μm at best focus (Section 2.3).

[3] Strictly speaking, the data points in the figure give the integrated Kα emission from concentric rings with thickness $dr = 6$ μm, normalised to a thickness of 1 μm.

center, the measured Kα emission decreases at the center, increases at larger distances and extends more and more outward, reaching a diameter of 400 μm!

The derivation of the Kα halfwidth from the commonly applied knife-edge measurements assumes a Gaussian shape of the Kα emission [87]. For defocus distances $\geq$ 100 μm, the emission profiles related to the experimental data[4] in Fig. 4.6 in fact have a Gaussian shape over a distance of $\sim$ 130 μm. At best focus only the central part of the emission profile can be described by a Gaussian, while farther from the emission center, $r > 60$ μm, it is much higher. In a one-dimensional spatial integration of the Kα emission, as it happens in a knife-edge measurement, this 'super-Gaussian' emission adds a wide low intensity pedestal to the resulting Kα profile but the main peak of the profile is still Gaussian and its halfwidth is practically unchanged. Thus, a knife-edge experiment would give the same halfwidths as shown in Fig. 4.5, but the specification of the halfwidth only gives limited information on the spatial extent of the Kα source: at best focus half of the emission originates from outside a radius of 60 μm around the center (Fig. 4.6) — twice the halfwidth.

From the examination of the imaging properties of the applied bent crystals (Section 2.4.2) it can be ruled out that the wide halo of weak Kα emission is an artefact of the imaging optics because it does not occur in any of the measured or simulated images of known Ti Kα sources. However, it cannot be ruled out that a low intensity pedestal of the laser makes a noticeable contribution to the halo. At best focus, the laser intensity could only be measured down to 3×10^{16} W/cm^2 (Fig. 2.4) with 15% of the laser energy being outside a 50 μm diameter (Section 2.3). PIC-MC simulations show that this energy is sufficient to produce a weak Kα emission of the halo size.

4.2 Source Sizes in the Literature

The observed relative broadening of the Kα source is in agreement with the experimental findings of other authors (Fig. 4.7, Table 4.1), where 'broadening' means the ratio of the halfwidth of the Kα emission to that of the laser focus. Especially Eder et al. [25] found similar halfwidths as in the present work for comparable conditions and the same failure

---

[4] The data of Fig. 4.6, which are angularly integrated Kα emissions, were divided by the integration area of each data point, $2\pi r dr$, thus giving an emission profile with high intensity resolution.

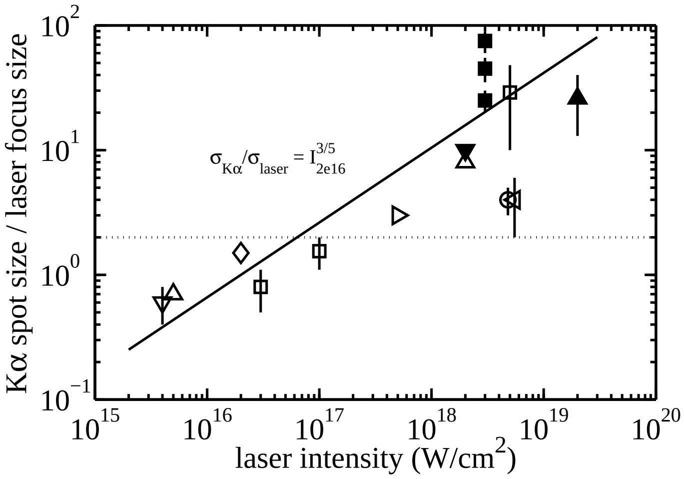

Figure 4.7: Ratio of measured Kα spot sizes to the size of the laser focii. The applied target materials and focus sizes are given in Table 4.1. The dotted line indicates the maximum source broadening which can be explained with electron scattering in the solid (Fig. 4.8). The Kα emission sizes indicated by black triangles were explained by the authors with the hot electron beams having half-cone angles of 15° (Pretzler et al. [66], ▼) or 30° and 90° (Wharton et al. [98], ▲). Zhidkov et al. [102] (■) attribute their millimeter Kα spot sizes to the fountain effect. The other symbols belong to: the present work (□), Eder et al. [25] (△), Soom et al. [87] (▽), Rousse et al. [74] (◇), Feurer et al. [29] (▷), Guo et al. [41] (◯), Yu et al. [101] (◁). The straight solid line is a guide to the eye to illustrate the general tendency of the relative Kα spot sizes.

of a PIC-MC model to explain the source size. In contrast to the present work, where the halfwidth remains constant even for a defocus distance of ~ 1 mm, Eder et al. found that it increases slowly when the laser is defocused. Agreement with their findings also exists for the total Kα yield having a local minimum at best focus — as already discussed in the previous chapter (Section 3.1).

Concerning the existence of a wide, weak halo of the Kα emission and the fact that the measured maximum Kα intensity remains relatively constant when the laser is stronger focused, no publication was found which mentions these points. For the maximum Kα intensity this is due to the fact that the knife-edge technique, which was used in practically all experiments, integrates the Kα intensity over one spatial dimension. Then, only a hypothetical maximum intensity could be reconstructed, assuming some spatial structure of the Kα emission like radial symmetry.

I	Target	Measure	Focal spot	Kα source size	Enlargement	Reference	Symbol in
$\left(\frac{\mathrm{W}}{\mathrm{cm}^2}\right)$			μm	μm			Fig. 4.7
4×10^{15}	SiO_2	1/e	12×24	10	0.4 – 0.8	SOOM et al. [87]	▽
5×10^{15}	Cu	FWHM	90	50 – 70	0.6 – 0.8	EDER et al. [25]	△
2×10^{16}	Al	FWHM	7	11	1.5	ROUSSE et al. [74]	◊
3×10^{16}	Ti	FWHM	20×105	95	0.5 – 1.1	the present work	□
1×10^{17}	Ti	FWHM	12×45	70	1.1 – 2	”	
5×10^{17}	Fe	FWHM	12	35	3	FEURER et al. [29]	▷
2×10^{18}	Cu	FWHM	5	40	8	EDER et al. [25]	△
2×10^{18}	Cu	FWHM	5	50	10	PRETZLER et al. [66]	▼
3×10^{18}	Al	$1/e^2$	20 – 30	1800	60 – 90	ZHIDKOV et al. [102]	■
	Ca	$1/e^2$	20 – 30	1100	35 – 55	”	
	Cu	$1/e^2$	20 – 30	1000	20 – 30	”	
5×10^{18}	Cu	$1/e^2$	4×8	20×25	3 – 5	GUO et al. [41]	○
5×10^{18}	Mo	FWHM	3	12 ± 5	2 – 6	YU et al. [101]	◁
7×10^{18}	Ti	FWHM	4.1×2.3	70	10 – 48	the present work	□
2×10^{19}	CH	FWHM	15	200 – 600	13 – 40	WHARTON et al. [98]	▲

Table 4.1: Experimental Kα source sizes.

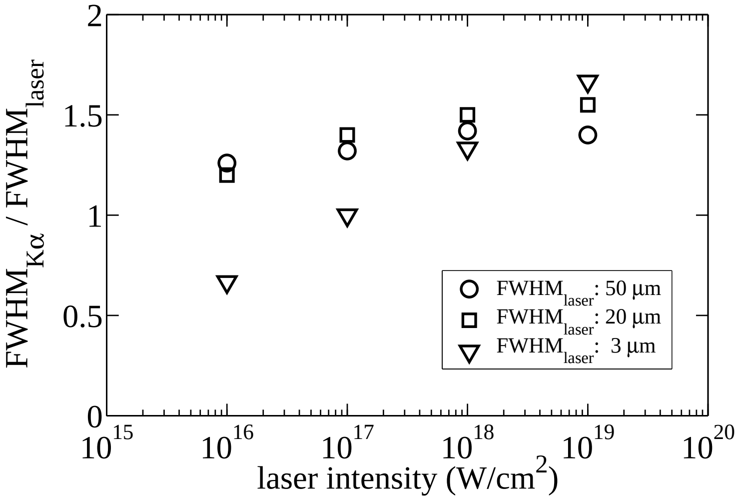

Figure 4.8: Kα source broadening due to electron scattering in the solid: size of the Kα emission from a Ti target according to the PIC-MC model compared to the size of the irradiating laser. The ratio of the halfwidths ($\mathrm{FWHM}_{K\alpha}/\mathrm{FWHM}_{laser}$) is given for laser focii with a Gaussian shape. Similar source broadenings were calculated for a Cu target.

The measured spatial Kα distributions contradict the theoretical predictions from the commonly used two-process description of Kα generation in laser plasmas, which only takes into account the generation of hot electrons at the critical density and their scattering in the solid. In this simplified description each hot electron is assumed to move straight from the point of laser absorption into the target, so that the shape of the Kα emission will reproduce the general shape of the laser focus. Due to the lateral scattering of the electrons in the solid the Kα emission will be broadened compared to the laser focus. PIC-MC calculations show that in practice the broadening caused by this scattering is limited to a factor < 2 (Fig. 4.8). For low laser intensities ($\sim 10^{16}$ W/cm^2) and small focii ($\sim 3\ \mu$m) the Kα source is even smaller than the laser focus.[5] With increasing laser intensity the source broadening also increases due to the longer stopping paths of the hot electrons.

The experimentally observed Kα source broadenings (Fig. 4.7) agree with these predictions only for laser intensities lower than 10^{17} W/cm^2. To explain the much larger

---

[5] The reason is, that below 10^{16} W/cm^2, additionally to the short scattering paths of the electrons, the Kα yield increases superlinear with the laser intensity. Thus, an intensity in the laser wing with half of the peak intensity produces *less* than half of the peak Kα intensity (which would be necessary to reproduce the FWHM of the laser).

observed source broadenings for higher laser intensities two explanations are suggested in the literature.

The first suggestion [25, 102] is to extend the classical picture by assuming a more complex movement of the hot electrons between their generation and their entrance into the solid. Such a process was studied 20 years ago for solid targets irradiated by the laser systems at that time ($I = 10^{14} - 10^{16}$ W/cm^2 and pulse durations of several 10 to 100 ps). In the expanding plasma created by a picosecond laser pulse, strong electric and magnetic fields develop [20] with the magnetic field forming a toroid parallel to the target surface and a peak value of several megagauss [68]. This field is situated well *outside* the critical density and redirects the electrons *emitted* from the plasma along the target surface so that they reenter as far as 1 mm from the laser spot [28, 32]. Due to the complexity of their trajectories in the combined magnetic and electric fields, the electrons can spend up to several hundred picoseconds in these orbits [96]. Because of the shape of the electron trajectories, going outward at the center and coming back at some distance, the effect is sometimes called the 'fountain effect'. Before this thesis no experimental or theoretical study of this effect for laser pulses with high intensities and femtosecond durations existed.

The other suggestion is that the hot electrons do not enter the solid unidirectionally but with some angular spread. Authors who studied the size of the Kα emission from fluorescence layers buried behind another material [66, 98] found that the measured Kα emission sizes and their dependence on target depth can be reproduced by assuming that the hot electron beams have half-cone angles of 15° [66], 30° [98] and 90° [41, 98]. In the study by Wharton et al. [98] the lower energy electrons ($E < 200$ keV) enter the target isotropically while the higher energetic ones form a narrow beam. A similar observation was made by Gremillet et al. [40].

4.3 Influence of Self-Generated Fields in the Experiment

In this section we make an estimate of the self-induced magnetic and electric fields for the best focus position in the experiment and how they influence the trajectories of the hot electrons and the Kα emission. Including the thermo-electric magnetic field arising from the plasma expansion, the electrostatic field of the space charges at the critical density and the ponderomotive force of the laser beam, this estimate gives a *qualitative* explanation for the observed source broadening, the low Kα peak emission and the enhanced yield.

In the expanding plasma a thermo-electric B-field is generated due to the non-collinear gradients of the electron temperature and density [88]:

$$\frac{\partial B}{\partial t} = \frac{\nabla T_e \times \nabla n_e}{e\, n_e}. \tag{4.1}$$

This field was determined by calculating the temperature and density development arising from the first experimental prepulse (7×10^{14} W/cm^2 at 4 ps before the main pulse, Section 2.3) with the hydrodynamic code MEDUSA [17, 24]. To derive two-dimensional distributions from the one-dimensional simulations, the plasma expansion normal to the solid's surface was calculated for a number of irradiated points at different distances from the focus center, where the experimental laser profile was approximated by a Gaussian with a halfwidth of 3 μm. Integration of Eq. 4.1 then gives the generated magnetic field. In a simpler modelling the MEDUSA simulations were substituted by the isothermal expansion model by Crow [20] with the plasma temperatures calculated according to the paper by Rosen [72].

When the main laser pulse hits the plasma, it expels a great number of electrons from the critical density and a large space charge field develops. This field was taken from PIC simulations of the plasma interaction with the main pulse. The PIC simulations take the electron currents self-consistently into account which partly compensate the space charge field. A two-dimensional field distribution was approximated in the same way as for the magnetic field.

Inside the laser beam an electron follows the oscillating electric field. Due to the spatial gradient of the laser intensity the field amplitude varies when the electron moves, so that a net acceleration of the electron results. This acceleration can be described by a 'ponderomotive field' of the laser, E_{pond}, which is proportional to the gradient of the intensity:

$$\boldsymbol{E}_{pond} = -\frac{1}{2\,n_c\,c}\nabla I. \tag{4.2}$$

In the modelling the ponderomotive field of the experimental main pulse with a peak intensity of 7×10^{18} W/cm^2 was included. Because of the rotational symmetry of the model normal incidence was assumed. Then, the lateral component of the ponderomotive field is due to the spatial profile of the laser beam, which was again approximated by a Gaussian with a halfwidth of 3 μm. The ponderomotive force in the direction of propagation results from the temporal shape of the laser pulse for which a Gaussian with a halfwidth of 90 fs was used.

The inital position of the critical plasma density where the main pulse is absorbed and the hot electrons are created was taken from the MEDUSA simulations. When the main pulse hits the plasma the density profile is steepened and the position of the critical density is pushed inward. This inward move is given by the PIC simulations and was included in the modelling.

The trajectories of the hot electrons in the fields were found by integrating the equations of motion (Eq. 1.25– 1.27), with the electrons starting at the critical density.

The effect of the self-generated fields on the electron trajectories is much simpler than in the picosecond fountain effect and can be summed up in two sentences: The magnetic field turns the hot electrons around so that they move outward, while the electric field either pushes them back into the magnetic field or kicks them away sidewards.

Fig. 4.9 gives an illustration of the magnetic field, together with the trajectories of two hot electrons. For our laser conditions the magnetic field is situated right in front of the solid, i.e. *behind* the critical density, and forms a toroid parallel to the solid with the maximum value 2 μm from the center of the laser focus. The peak strength is about 150 MG. The Larmor radius of a 100 keV electron in such a field is < 0.1 μm, so that this electron cannot penetrate into the target but is turned around. Away from the solid the field decays on a length scale similar to the Larmor radius so that the electron does not perform a closed circular orbit but leaves the magnetic field immediately. This holds for electron energies above 10 keV. The magnetic field vanishes towards the center. At a radius of 4.5 μm it has decayed by an order of magnitude. Thus, electrons within the

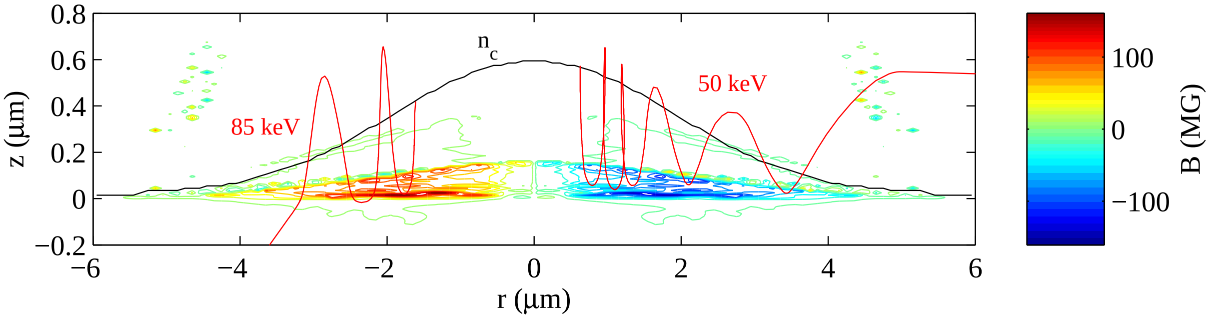

Figure 4.9: Thermo-electric magnetic field in the Ti plasma derived from hydrodynamic simulations. The original position of the solid is at $z \leq 0$ and the plasma expands towards $z > 0$. The position of the critical density n_c before the arrival of the main pulse is indicated by the black line. The red lines show the trajectories of two hot electrons which are generated at the critical density 75 fs before the peak of the main pulse reaches the target.

energy range most suitable to generate Ti Kα radiation[6] cannot penetrate into the target in a 2 ± 1 μm ring around the focal center. Electrons whose energy and generation point allow them to overcome the magnetic field perform a circular arc and enter the solid with a shallow angle.

The electric field of the space charges and the *lateral* ponderomotive field have a similar strength with maximum values of 2×10^{12} V/m. This field strength is sufficient to invert the direction of a 100 keV electron moving against the field within the space charge zone of a few microns. (The component of the ponderomotive force towards the target is one order of magnitude smaller.) During the laser pulse the magnitude and the direction of the electric field change because the laser pulse moves towards the target and the space charges first develop and then vanish again. As long as the space charge field is high it reflects the outgoing hot electrons inwards which then oscillate between the magnetic and the electric field. The oscillation either ends when an electron comes to a point where the magnetic field is weak enough to be penetrated or when the electron leaves the area with the fields outward. In this case usually the lateral ponderomotive force is dominant so that the electron moves sidewards with a shallow angle. Towards the end of the laser pulse

---

[6] This optimal energy range is $E_K - 20E_K$ (Section 3.3.3), with the K-shell ionization energy of Ti being $E_K = 5$ keV .

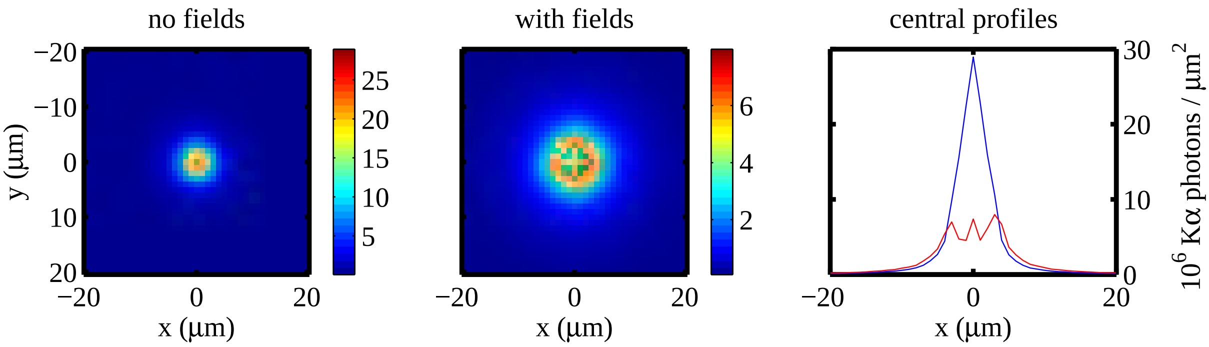

Figure 4.10: Simulated Kα emission with (red profile) and without electric and self-induced magnetic fields (blue profile).[7]

when both the space charge and the ponderomotive field are weak, electrons also escape close to the target normal.

To estimate the consequences of these electron orbits for the Kα emission about 900 sample trajectories were calculated for different generation points and times and different electron energies. These trajectories were then weighted according to the hot electron distributions from the PIC simulations and the resulting Kα emission was calculated with the Monte Carlo code.

The calculations *qualitatively* reproduce the three main experimental observations:

1. For the investigated laser focus the maximum Kα emission is a factor of 4–5 lower than predicted by a PIC-MC calculation without the fields (Fig. 4.10), because the magnetic shielding reduces the number of hot electrons penetrating at the center. Thus, the investigated mechanism has the potential to explain the measurement, which shows that the peak Kα emission is by a factor of ~ 5 lower compared to the PIC-MC simulations without fields (Fig. 4.3). When the laser is stronger focused the magnetic field strength increases (see below) and a greater fraction of hot electrons is reflected by the field. This could explain the observed decrease of the maximum Kα emission close to best focus (Fig. 4.1 for $f_p < 100\ \mu$m).

2. Close to best focus the total Kα yield is higher than predicted by the PIC-MC calculations because the hot electrons gain additional energy in the electric field. In particular, the energy of the 'escaping' electrons is 3.5 times higher than their initial

---

[7] The escaping 10% of the hot electrons were neglected in this simulation.

energy, mainly due to the push by the lateral ponderomotive force. Together with the shallower penetration angles which reduce the influence of Kα reabsorption, this results in a 15% increase of the total Kα yield compared to the modelling without fields. Experimentally, a 60% higher yield was found (Fig. 4.4).

3. The mechanism can possibly also explain large source sizes. These could originate from the hot electrons kicked at shallow angles along the target surface. In the present modelling these electrons are about 10% of all hot electrons, which is insufficient to generate the high Kα emissions measured at large distances from the laser focus (Fig. 4.6). Thus, the fraction of escaping electrons is probably larger than modeled. From the other 90% of the hot electrons, which enter the solid within or close to the laser focus, many with shallow angles, a relatively small additional broadening results: the calculated halfwidth of the emission increases from 4.6 μm to 11 μm when the self-induced fields are included (Fig. 4.10) — compared to $\sim$ 70 μm in the experiment (Fig. 4.5).

Due to the deflection in the magnetic field the hot electrons enter the solid with an angular distribution. Electrons with energies below 200 keV enter isotropically while the higher energetic ones form a beam with a half-cone angle of 20 – 40°. This behaviour is in agreement with the electron entrance angles estimated by Wharton et al. [98] and Pretzler et al. [66].

The crucial point for the presented effects is the presence of a magnetic field, generated by the prepulse, which reflects a large portion of the hot electrons, so that these electrons can be spread over a wide area by other fields further away from the solid. To estimate for which laser parameters the thermo-electric B-field can occur, a scaling law can be derived from the isothermal plasma expansion model. In this description the temperature gradient is only radial and the density gradient only axial. The density profile is exponential [20], so that $\nabla n_e / n_e$ is the reciprocal of the density scale length, L. The temporal development of the scale length and the electron temperature, T_e, is given by [20, 72]

$$L \propto I^{2/9} t^{8/9}, \tag{4.3}$$

$$T_e \propto I^{4/9} t^{-2/9}. \tag{4.4}$$

Applying (4.3) and (4.4) for a Gaussian laser profile, the magnetic field is

$$B = \int \frac{dT_e}{dr} \times \frac{dn_e}{e\, n_e\, dz}\, dt \quad \propto \quad \left[I \exp\left(-\left(\frac{r}{\sigma}\right)^2 \right) \right]^{4/9} \left(\frac{r}{\sigma}\right) \times \left[I \exp\left(-\left(\frac{r}{\sigma}\right)^2 \right) \right]^{-2/9}, \tag{4.5}$$

where I is the central laser intensity and σ the halfwidth of the focus. Setting $\partial B/\partial r = 0$ yields the location of the maximum field strength, $r_{Bmax} = \sigma/\sqrt{2}$. Using the values of the presented simulation, where a hot electron experiences a typical magnetic field of $\sim$ 80 MG, the field scales as

$$B_{max} \approx \left(\frac{I_{prepulse}}{10^{14}\,\mathrm{W/cm^2}} \right)^{2/9} \left(\frac{\sigma}{\mu\mathrm{m}} \right)^{-1} \quad 150\ \mathrm{MG}. \tag{4.6}$$

A set of MEDUSA simulations suggests a similar scaling, but with $B_{max} \propto I^{1/2}$. A similar value of the field strength as from Eq. 4.6 is found by a rough estimate according to the paper by Bell et al. [7]. The relatively high magnetic field is mainly due to the steep density profile with a scale length $\leq 0.01\ \mu$m and the plasma temperature of $\sim$ 4 keV during the field generation. Haines [42] has shown that dissipative and convective processes lead to a saturation of the generated B-field. For our case, his estimate predicts a maximum field of several tens of megagauss, so that the magnetic field will be several times lower than modeled.

The maximum lateral ponderomotive field, E_r, for a fixed ratio r/σ scales as

$$E_r \approx \left(\frac{I_{main}}{10^{18}\,\mathrm{W/cm^2}} \right) \left(\frac{\sigma}{\mu\mathrm{m}} \right)^{-1} \quad 2 \times 10^{12}\ \frac{\mathrm{V}}{\mathrm{m}}. \tag{4.7}$$

The scalings in Eqs. 4.6 and 4.7 imply that the investigated effect only occurs at high laser intensities and strong focusing. In the experiment, the influence of the fountain effect is found for defocus distances up to 150–250 μm (Figs. 4.3–4.5). This can be explained by the second prepulse (7×10^{15} W/cm^2 at 600 fs before the main pulse) which was neglected in the present modelling. As the thermo-electric field develops within 500 fs this pulse alone can generate for a defocus distance of 150 μm a magnetic field which is only one order of magnitude weaker than the modeled one — sufficient to reflect a noticeable portion of the hot electrons.

The fact that the modelling gives a much smaller Kα source size than measured points to its deficiencies. For example, normal incidence was assumed, multi-dimensional effects like pinching of the expanding plasma by the magnetic field [12] are neglected and the space charge field will be overestimated due to the stronger Coulomb law in 1D. Also, a number of processes which generate additional magnetic fields are not included. One of these fields is generated by the hot electron current. About 65% of these electrons enter the solid without being reflected at the magnetic field. Assuming them to form a constant homogeneous current within a 10 μm cylinder these electrons would generate a magnetic field of 55 MG at the cylinder surface. This field will be superimposed on the thermo-electric field with opposite sign.[8] Further magnetic fields can be generated due to the space and time dependence of the ponderomotive force [91] and by the surface plasma electrons acquiring a net lateral momentum due to the oblique incidence of the laser beam [14]. Both fields are localized within a fraction of the laser wavelength around the critical density. While the laser intensity in the experiment was probably too low to give a significant contribution from the first mechanism[9] the PIC simulations suggest a field of 30–130 MG due to the second one. Thus, a modelling which includes all of these processes self-consistently would be needed to explain the observed spatial structure of the Kα emission.

The estimated electron trajectories imply a prolongation of the Kα pulse duration due to the time which the hot electrons spent in front of the target. Taking into account the measured source sizes, an estimate of the pulse prolongation can be made, which will be included in the following chapter about the temporal shape of the Kα pulses (page 85).

---

[8] The other 25% of the hot electrons rapidly change their direction of movement between the space charge and the magnetic field, so that they will only produce a small net field.

[9] The maximum B-field from this mechanism is similar to the laser oscillating magnetic field, which was in our case ≈ 2.5 MG.

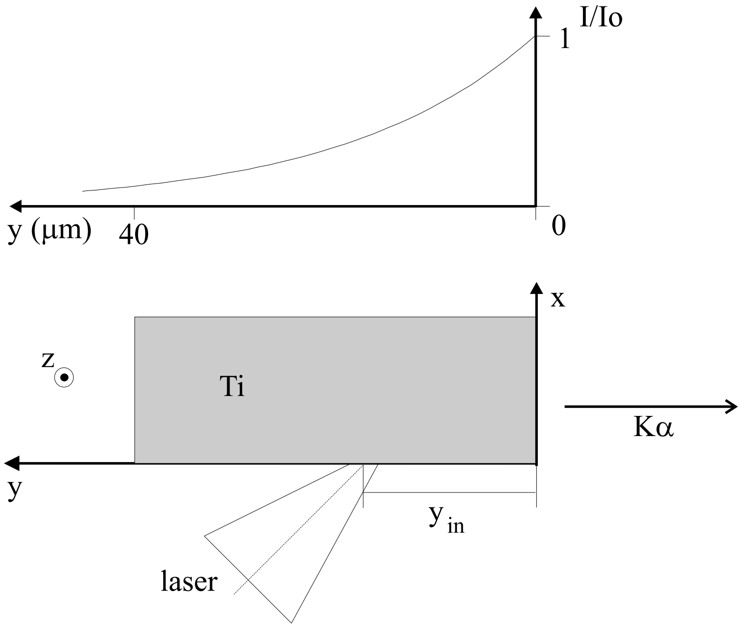

Figure 4.11: The experimental situation for the observation of the Kα emission from the target side (x-z-plane). The upper curve shows the emitted fraction I/I_0 of the Kα radiation which is generated at a distance y from the observed target surface.

4.4 Kα Emission from the Target Side

The proposed mechanism to explain the measured Kα emission from the target frontside suggests, that for a strongly focused laser, a portion of the hot electrons does not penetrate into the target as deeply as predicted by the PIC-MC model but stays close to the target surface. The penetration depth of the hot electrons in the experiment was measured by taking two-dimensional images of the Kα emission from the target side. The experimental situation is illustrated in Fig. 4.11. The laser was focused onto the target at a distance y_{in} from the target edge which was similar to the absorption length of the Kα radiation, $\lambda_{abs} \approx 20\ \mu$m, so that the target was optically thin in these measurements.

Fig. 4.12 gives in the top row two experimental images of the Kα emission from the target side taken at different defocus distances. One image was taken close to best focus ($I \approx 3 \times 10^{18}$ W/cm^2) and the other $\Delta f_p = +250\ \mu$m away from the first one ($I \approx 5 \times 10^{16}$ W/cm^2). The distance from the target edge, $y_{in} \leq 30\ \mu$m, was the same for both images. In the images the edge is clearly seen, running vertically at $x = 0$. The target extends to its right and the laser comes from the left. The second row of the figure gives the corresponding images from PIC-MC simulations for the experimental parameters. As

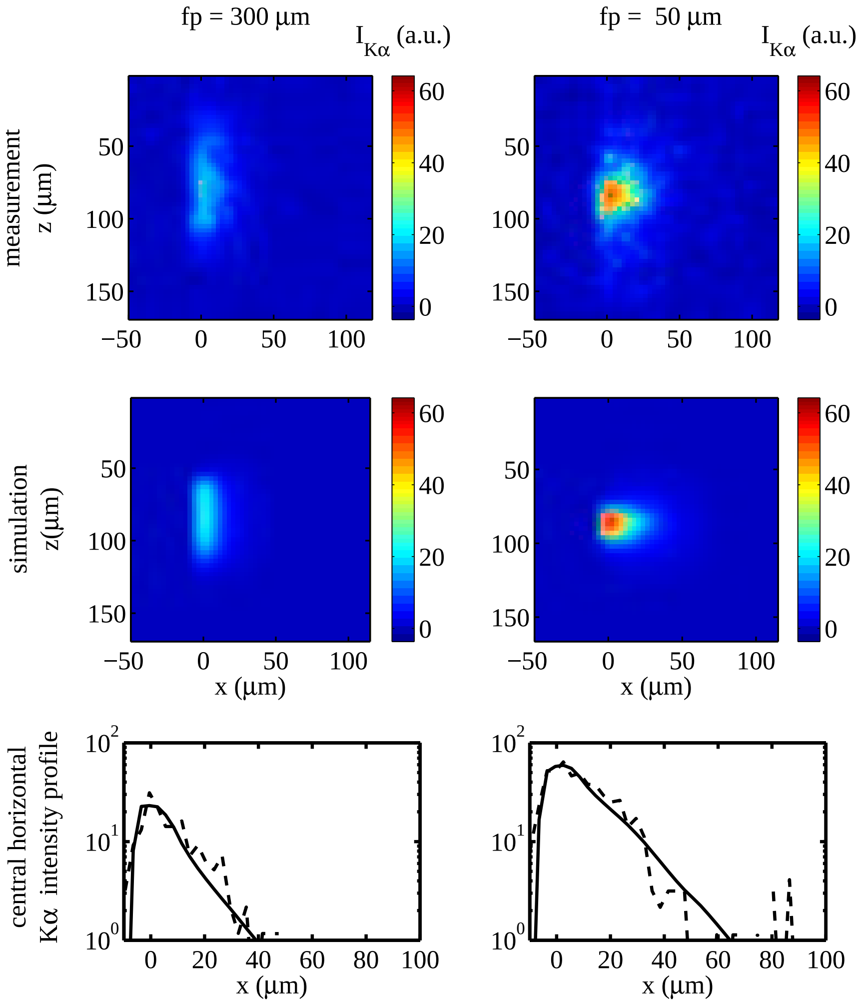

Figure 4.12: Measured and simulated images of the Kα emission from the target side for two defocus distances f_p. The central intensity profiles of the experimental (dashed) and the calculated (solid) images are shown in the bottom row.

these parameters are only determined within certain limits ($\Delta f_p = \pm 50$ μm, $\Delta y_{in} = \pm 10$ μm) a set of simulations was performed for this parameter range. It was found that the experimental images are best reproduced assumig a distance of the peak laser intensity from the target edge $y_{in} = 25$ μm and defocus distances of $f_p = 50$ μm and 300 μm, respectively. Then, especially the intensity profiles at the center of the Kα emission show good agreement over more than one order of magnitude (Fig. 4.12, bottom row).[10]

In the images in Fig. 4.12 the influence of the aberrations of the imaging technique (Section 2.4.2) can be seen: the sharp target edge is smeared ~ 10 μm towards the vacuum

---

[10] The simulated Kα intensities were normalised to those of the measured image at $f_p = 300$ μm.

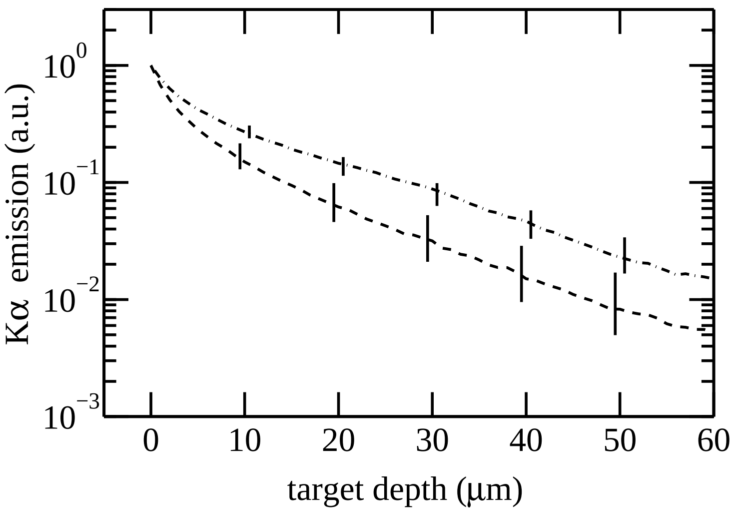

Figure 4.13: Simulated depthprofiles of the Kα emission from the target side correspondig to the images in Fig. 4.12. The dash-dotted line is for a defocus distance of $f_p = 50\ \mu$m, the dashed line for $f_p = 300\ \mu$m. The error bars indicate the range which is in agreement with the depth profiles of the measured images.

side, $x < 0$, while towards the target side, $x > 0$, an exponential intensity decay appears. The general relation between source size and image size for Kα sources with a Gaussian intensity profile, which was studied in Section 2.4.2 (Fig. 2.11), suggests that the Kα emission from the target itself has a halfwidth in the order of a few microns for both images. Thus, the Kα signal on the images consists mainly of aberrations.

The depth profiles of the Kα emission itself (Fig. 4.13) can be estimated from the simulated emissions before ray-tracing was applied. The PIC-MC calculated emission profiles in Fig. 4.13 show a dependence of the Kα emission, $I_{K\alpha}$, on target depth, x, according to

$$I_{K\alpha}(x) \propto e^{-\left(\frac{x}{x_0}\right)^{2/3}}. \tag{4.8}$$

A range of emission profiles, which reproduce the measured image in the ray-tracing, can be found by variation of the parameter x_0 in Eq. 4.8. These ranges of emission profiles, which are in agreement with the measurement, are indicated by the error bars in Fig. 4.13. For the PIC-MC calculated profiles, x_0 is 5 μm for $f_p = 300\ \mu$m and 7 μm for $f_p = 50\ \mu$m. The error bars show that the two emission profiles can be well distinguished from each other.

The possible emission profiles for each of the two laser focusings are within a rather narrow range around the simulated ones. Thus, the Kα images from the target side give no confirmation of a reduced hot electron penetration depth compared to that given by the PIC-MC simulations.[11] This might be due to a reduction or modification of the self-generated fields close to the target edge. Such a modification is indicated by the images from the target frontside taken at the same laser shots as the images in Fig. 4.12. The frontside image at $f_p = 50$ μm shows a 15% lower total Kα yield but a 15% *higher* peak Kα emission compared to an image taken 1 mm away from the edge. According to the estimate of the self-induced fields given in the previous section an increase of the peak Kα emission would indicate a reduction of the magnetic field, so that more hot electrons can pass through the field and generate Kα radiation at the focus center. In a reduced B-field the penetrating hot electrons are less deflected, so that their penetration behaviour is similar to that given by the PIC-MC model. Despite a possible reduction of the self-generated magnetic field for laser shots close to the target edge, both the images from the front and the side of the target for these shots show a wide weak Kα emission with a total vertical extension of ~ 250 μm for $f_p = 50$ μm, suggesting that there is still a magnetic field present.

---

[11] Taking the sharp drop of the Kα signal in the measured profile at $x \approx 30$ μm for $f_p = 50$ μm (Fig. 4.12), which is not reproduced by the PIC-MC simulations, as an indicator of such a reduction, remains speculative, as there is also a Kα emission higher than calculated at greater target depths, $x > 80$ μm, so that these differences can also be due to statistical fluctuations of the measured signal.

Chapter 5

Achieving Efficient fs X-Ray Pulses

The temporal structure of the Kα emission from a laser plasma source is a convolution of the laser pulse shape with the stopping times of the generated hot electrons.[1] The Kα emission starts shortly after the laser pulse hits the plasma, when the first hot electrons are generated and enter the solid. After the laser pulse has gone, it continues until the energy of the last hot electron in the solid has dropped below the K-shell ionization energy. The total duration of the x-ray emission is thus the sum of the durations of the laser pulse τ_l and of the 'afterglow' emission τ_a:

$$\tau_x \approx \tau_l + \tau_a. \tag{5.1}$$

For a single Kα photon, the emission time is the sum of the generation time of the photon and the time it takes the photon to reach the target surface. The situation is illustrated in Fig. 5.1 for a monoenergetic electron beam in a Si target with incidence energy E = 100 keV. In the Monte Carlo simulations, on which the figure is based, all electrons enter the target at the same time. Then, the kinetic energy of all electrons drops below the ionization energy of the Si K-shell at the same time (except for the electrons that left the target before). No more Kα photons can be produced and the simulation stops. This happens after 600 fs: the number of generated photons per unit time (dashed line in Fig. 5.1,a) drops to zero.[2] At the same time, the mean depth of the electrons inside the target (Fig. 5.1,b) is no longer calculated.

Due to the time which it takes a photon to get from the point where it is generated to the target surface, the total afterglow duration is another 200 fs longer (dash-dotted line in Fig. 5.1,a). This is consistent with a *mean* depth of the electrons of ~30 μm at the end of

---

[1] The influence of self-induced magnetic and electric fields (Section 4.3) on the Kα pulse shape will be discussed on page 85.

[2] By chance, the number of generated photons per time in this example is roughly constant because the decrease of the electron's speed, ds/dt, with time is compensated by an increase of the Casnati cross section for the ionization of the K-shell, σ_K, so that the rate of produced K-shell vacancies, $\sigma_K ds/dt$, is constant.

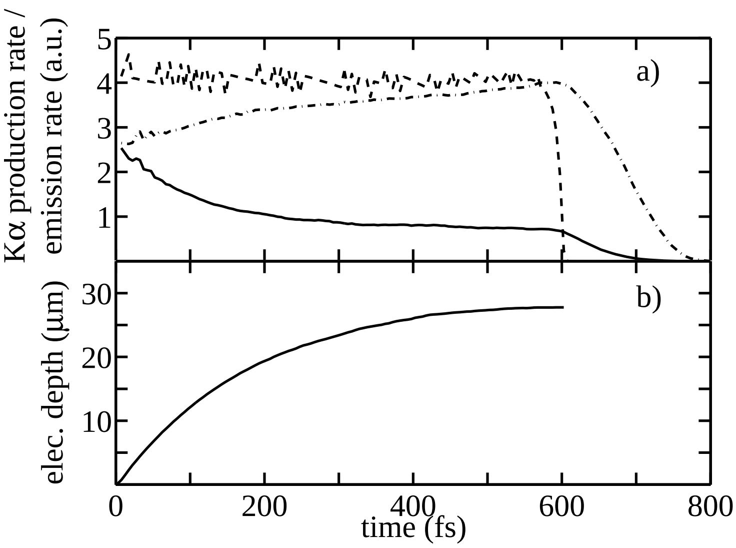

Figure 5.1: Temporal development of Kα production in bulk Si for a monoenergetic electron beam ($E = 100$ keV) entering the target at $t = 0$ fs. a) Temporal development of Kα photon numbers per unit time. Dashed line: number of generated photons, solid line: number of detected photons, dash-dotted line: detected photons if there would be no reabsorption in the target. b) Mean depth of the electrons inside the target.

the simulation. Taking into account the speed of light, $c = 0.3$ μm/fs, a photon generated in this depth is observed 100 fs later. The (relatively few) electrons twice as deep produce the observed 200 fs prolongation.

As photon reabsorption inside the target is not included, the total number of photons is the same in both simulations (Fig. 5.1,a, the integrals over the dashed and the dash-dotted line are the same). In the beginning, all electrons move into the target, so that the time which it takes the generated Kα photons to get to the target surface is permanently increasing. The rate of photon emission is lower than the rate of photon production. Together with the high speed of the incident electrons (which is half the speed of light or 0.15 μm/fs) this shifts a considerable part of the emission to later times. After some time, the electron movement becomes isotropic and the rates of produced photons and photons emitted from the target surface become similar. After all electrons have stopped, the Kα emission continues until the last photon has reached the target surface.

The fact that most Kα photons are generated in a target depth that is greater than the absorption length, $\lambda_{abs} \approx 12$ μm, causes a great fraction of them to be reabsorbed on their way to the target surface. The rate of observed photons when reabsorption is taken into account, and thus the measureable Kα emission, is shown by the solid line in Fig. 5.1,a. As the mean generation depth of the photons increases with time, the influence of reabsorption also increases. The result is that the Kα emission is highest right in the beginning, when the electrons are close to the surface. After 150 fs, it has already dropped to less than half of its initial value. Also, the very last part of the emission is very low, because it comes from the electrons which are deepest in the target.

Of course, the details of the picture given above depend very much on the combination of target material and incident electron energy. But the main features of the Kα emission, 1) being highest in the beginning and 2) going on weakly for up to several 100 fs after the last electron stopped, are always the same.

5.1 Pulse Duration from Bulk Targets

Now turning to the Kα emission produced by a femtosecond laser pulse, the situation becomes rather complex. During the interaction of the laser pulse hot electrons with different energies are generated with the most energetic electrons being produced when the instantaneous laser intensity is close to its peak value. According to their energies, the electrons have different thermalisation times and different penetration depths, thus producing afterglow emissions with different time structures.

In the following, the pulse shape will be discussed for a Si target. In this element, electrons with energies of a few hundreds of keV have thermalisation times in the picosecond range (Fig. 5.2,a). The total duration of the Kα emission from a femtosecond laser pulse will be comparable to that. Nevertheless, the 'effective pulse duration', i.e. the time scale which can be resolved in an experimental application of the x-ray source, is much shorter. The higher energetic electrons penetrate deeply beyond the Kα absorption length and then only give a small contribution to the emitted radiation: from a depth twice the Kα absorption length, λ_{abs}, only 10% of the generated photons reach the target surface. In Si a depth of $2\lambda_{abs}$ is comparable to the stopping range of a 50 keV electron (Fig. 5.2,b). Such an electron does not actually penetrate to that depth due to the lateral deflections on its path, but for 75 keV already one third of the electrons reach the depth of $2\lambda_{abs}$ and

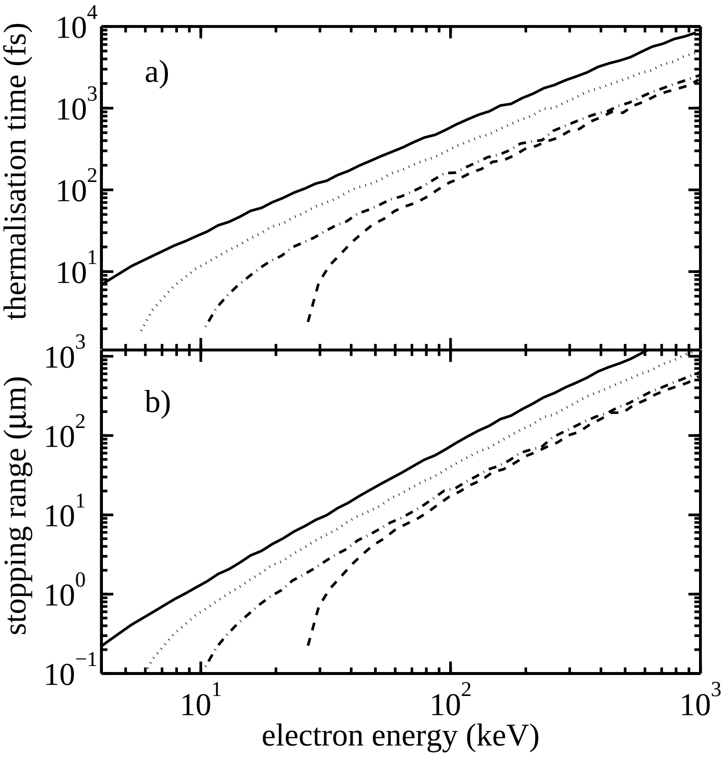

Figure 5.2: Stopping of electrons in Si (solid), Ti (dotted), Cu (dash-dotted) and Ag (dashed). a) Thermalisation times of the electrons. b) Electron stopping ranges.[3]

thermalize beyond it.

Fig. 5.3 shows the temporal shape of Si Kα pulses produced by a 60 fs laser pulse. For both intensities in the figure (3×10^{15} and 3×10^{16} W/cm^2) the rise of the Kα signal is closely related to the intensity rise of the laser pulse. At $I = 3 \times 10^{15}$ W/cm^2, which is the optimal laser intensity for this element,[4] most of the hot electrons stay close to the target surface and the falling-off of the Kα signal after the laser pulse is gone[5] is mainly given by the thermalisation of the electrons. As discussed in Chapter 3, reabsorption of Kα photons inside the target only plays a minor role at this intensity. When the laser intensity is increased (Fig. 5.3, right column) the Kα pulse shape becomes dominated by the inward movement of the hot electrons. Compared to the optimal intensity, both the total Kα yield and the Kα peak emission are reduced because the hot electrons penetrate

---

[3] The data were calculated with the PIC-MC model. Similar values were given by BERGER and SELTZER [9] and KANAYA and OKAYAMA [49] for the stopping ranges, and by ROUSSE [73] for the thermalisation times in Al, Cr and Ag for electron energies below 50 keV.

[4] Eq. 3.15 and Fig. 3.10.

[5] A FWHM of 60 fs corresponds to total laser pulse duration of ~110 fs.

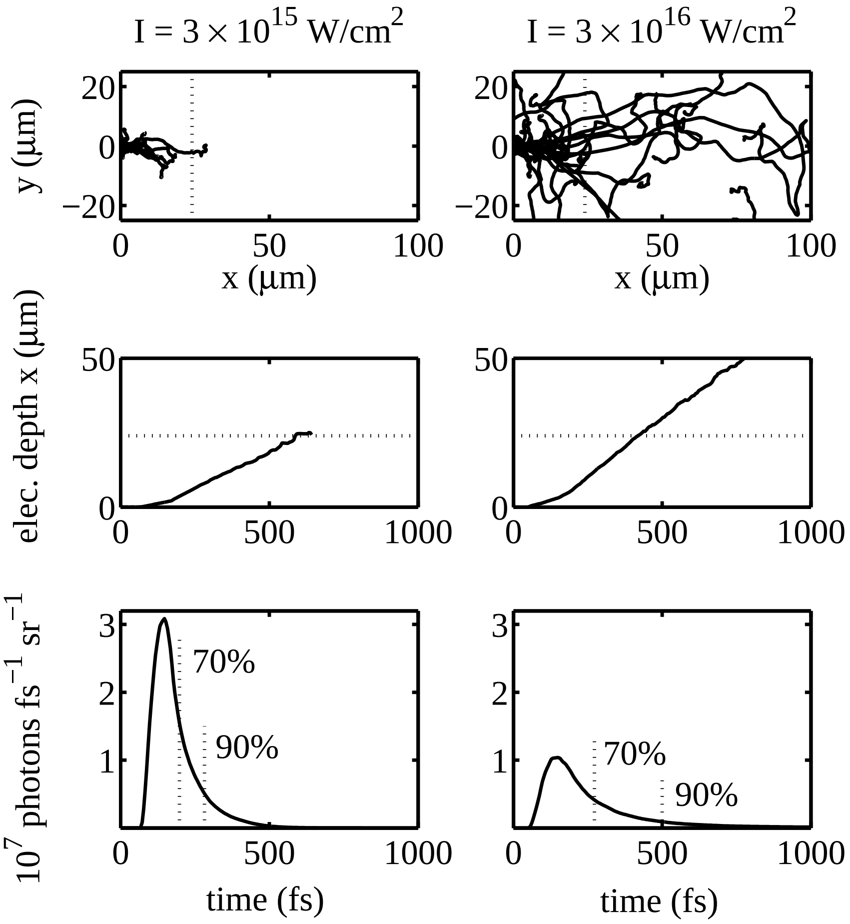

Figure 5.3: Simulated electron penetration into bulk Si irradiated for 60 fs at two different laser intensities I and development of the correspondig Kα emission . The top graphs show 150 electron scattering paths for each intensity. The central and bottom graphs give the temporal development of the mean electron depth inside the target and that of the Kα emission. The dotted lines (top and center) indicate the target depth for which 90% of the generated photons are reabsorbed, $x \approx 2\lambda_{abs} \approx 24$ μm. The dotted lines in the bottom graphs indicate the percentage of the total Kα emission which is over at that time.

faster and the Kα photons are generated deeper inside the target.[6] The total duration of the Kα emission increases from 750 fs to 2.8 ps.

To characterise the effective pulse duration usually the full width at half maximum (FWHM) is used. In the examples given in Fig. 5.3 it is 100 fs and 180 fs respectively. As Fig. 5.3 shows, about 30% of the emission occur at a later time, creating a background signal in diagnostic applications when the investigated configuration changes within that

---

[6] As in Chapter 3, the simulations assume a constant laser energy of 100 mJ and the total kinetic energy in the hot electrons remains roughly constant, but is differently distributed over the electrons.

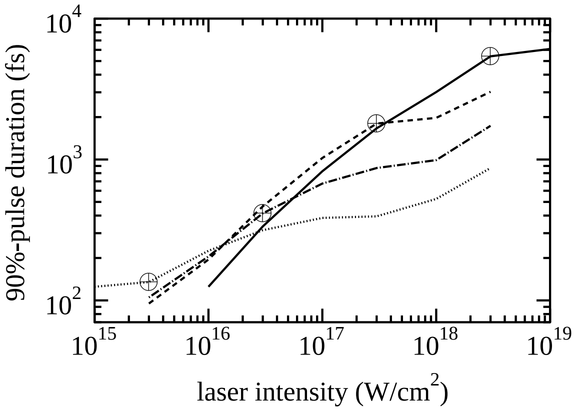

Figure 5.4: Simulated 90% Kα pulse durations from bulk targets for a 60 fs laser pulse: Ti (dotted), Cu (dash-dotted), Ag (dashed) and Ta (solid). The crosses mark the optimal laser intensities for each element (Eq. 3.15 and Fig. 3.3).

time. With increasing laser intensity this 'shoulder' of the Kα emission is stretched in time. Therefore, in the following, the time of the first 90% of emission instead of the halfwidth will be used to characterise the pulse duration. The subsequent low-intensity emission from the 'tail' will have a negligible influence on most observations. At the optimum laser intensity 90% of the Si Kα emission occur within the first 210 fs.

Fig. 5.4 gives an overview over the 90%-pulse durations calculated with the PIC-MC model. With increasing laser intensity, the pulse duration first increases (because the thermalisation times of the hot electrons increase), but then tends to saturate when the hot electrons penetrate deeper into the target. Because the absorption length is smaller and the electrons penetrate deeper in lighter elements the restriction of the pulse duration occurs earlier and is stronger in these elements than in heavier ones, i.e. the pulse duration is shorter in lighter elements (Fig. 5.4, for the same, high laser intensity). At low intensities, the 90%-pulse duration is longer for lighter elements because both the stopping power and the K-shell ionization energy, E_K, are lower, so that it takes longer before the electrons' energies have fallen below E_K. For laser intensities above 10^{16} W/cm^2 the 90%-pulse duration is much longer than the halfwidth of the Kα emission which is about $100 - 180$ fs for target elements from Si to Cu.

As Fig. 5.4 shows, the optimal laser intensities needed for high Kα yield will make it difficult, except for the lightest elements, to generate from bulk targets the efficient 100 fs Kα pulses desired for ultrafast diagnostic applications. To overcome these limits, in

Section 5.3 the design of foil targets is discussed to produce hard x-ray pulses with high yield and a specific duration.

In the preceding chapter an estimate was made how electric and magnetic fields in the plasma can modify the orbits of the hot electrons before they enter the solid (Section 4.3). The estimate also implies a modification of the expected Kα pulse shape at laser intensities above 10^{18} W/cm^2. In the fields present in the experiments with picosecond lasers, performed twenty years ago, the electrons could spent many picoseconds due to the shape and the duration of these fields [96]. In contrast, the electrons typically leave the fields discussed in Section 4.3 within less than 50 fs, either entering the solid or being kicked away laterally. Consequently, the halfwidth of the Kα emission from a Ti target irradiated for 90 fs at 7×10^{18} W/cm^2, for which the fields were calculated, broadens from 165 to 200 fs. When the magnetic field is calculated with the isothermal expansion model instead of the hydrodynamic simulation code the electrons stay longer in the fields but less than 100 fs. Also, the inclusion of magnetic fields generated by other mechanisms (page 72) will not result in complex electron orbits lasting longer than the laser pulse because these fields only persist during the laser irradiation.

About 10% of the electrons in the calculations in Section 4.3 leave the electric and magnetic fields along the target surface, directed away from it at shallow angles. These electrons will no longer perform ‘complex orbits’ but ballistic trajectories. As the exact forces which pull these electrons back into the target are not known, we estimate their time of flight from the measured extension of the Kα source for which we take a radius of 100 μm as a mean value (Fig. 4.6). Due to the sideward push from the ponderomotive force 50% of these electrons have lateral energies higher than 80 keV and 37% energies higher than 100 keV. Assuming a constant lateral velocity of the electrons most of them have times of flight of 500 – 700 fs. Adding these electrons into the MC simulation prolongs the tail of the calculated Ti Kα pulse, so that the first 75% of the emission occur within 550 fs instead of 400 fs. Though a fraction of the electrons has times of flight of several picoseconds, and in spite of the approximations in the field etimate, the estimated 90%-pulse duration is below 1 ps anyway.

5.2 Comparison with Experiment

Experimentally the duration of the x-ray pulses is either measured with an x-ray streak camera [4, 50, 100] or by cross-correlating the x-ray pulse with the laser beam which creates the plasma and the Kα radiation [31, 77, 86].

The idea of a cross-correlation or 'pump-probe' measurement is to put a 'fast' x-ray switch between the Kα source and a time-integrating detector. It usually consists of a Bragg-reflecting crystal which is irradiated by a small fraction of the laser beam, the 'pump pulse' which 'destroys' the x-ray reflectivity of the crystal. Thus, all the Kα photons on the detector must have reached the crystal before the pump pulse. By varying the delay time, Δt, between the pump pulse and the Kα creating laser pulse, it is possible to measure the temporal development of the x-ray pulse. The method is called 'pump-probe' because it can be also used to probe the structural changes of the pumped crystal with the x-ray pulse.

In practice, the fluence of the pump pulse is chosen to excite rapidly a large number of electron-hole pairs so that the chemical bonds in the crystal break up and the atoms start to move. This deranges the lattice order within a fraction of the Kα penetration depth and reduces its x-ray reflectivity on a time scale of several 100 fs [89]. The result of the measurement, $I_{detector}(\Delta t)$, is the convolution of the x-ray pulse from the plasma source, $I_{K\alpha}(t)$, with the reflectivity of the crystal, $R(t)$:[7]

$$I_{detector}(\Delta t) = \int_{-\infty}^{\infty} I_{K\alpha}(t - \Delta t)\, R(t)\; dt. \tag{5.2}$$

As both the x-ray pulse and the disordering of the crystal happen on similar timescales, each pump-probe experiment measures both processes simultaneously and their contributions cannot be seperated. Thus, the delay time Δt, after which no further change in Kα signal is seen, only gives an upper limit for the durations of both processes. Due to the velocity of the atomic movement this upper limit cannot be smaller than a few 100 fs which defines the temporal resolution of the method.

In an experiment at the IOQ Jena the duration of laser-produced Si Kα pulses was measured by T. Feurer, A. Morak and I. Uschmann with a cross-correlation technique and

---

[7] The x-ray optics to focus the Kα burst onto the pumped crystal additionally broadens the x-ray pulse several femtoseconds [57].

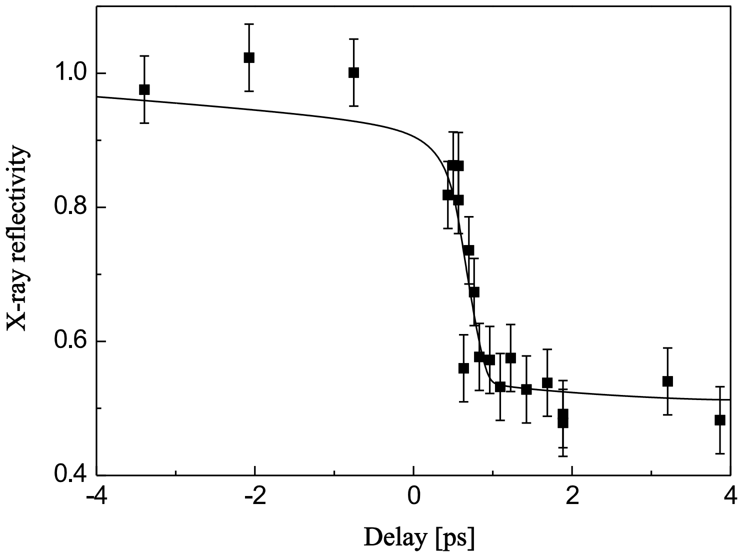

Figure 5.5: Measured reflected x-ray intensity as a function of the delay time between the optical pump and the x-ray pulse (squares). Negative delay times mean that the x-ray pulse is before the optical pump. The solid line is the best fit using the calculated pulse shape. (From Feurer et al. [31].)

compared with calculations based on the present work [31]. A 320 nm CdTe layer was used as the reflecting crystal. The Kα creating laser intensity was 10^{17} W/cm^2 with a pulse duration of 100 fs. The setup and the data analysis are described extensively in Feurer et al. [30]. Fig. 5.5 shows the dependence of the measured Kα signal on the delay time Δt between the Kα creating pulse and the pump pulse. The solid line in the figure is a fit to the experimental data assuming the x-ray pulse shape calculated with the PIC-MC model and a linear decay of the crystal reflectivity after laser irradiation. The calculated Kα halfwidth is 180 fs and the reflectivity decay time which gives the best agreement is 540 fs (from 90% to 10%). With these assumptions the drop of the measured signal within 640 ± 50 fs is well reproduced.

As mentioned above, other interpretations of the experimental data are also possible. To visualize the combinations of pulse duration and reflectivity decay time which give good agreement with the measured data, Fig. 5.6 shows the quadratic deviation between calculated and measured signals. The calculated data use Gaussian Kα pulses with different halfwidths and assume linearily decaying x-ray reflectivities. Black indicates the greatest agreement with the experiment. The two extreme interpretations are to assume either a

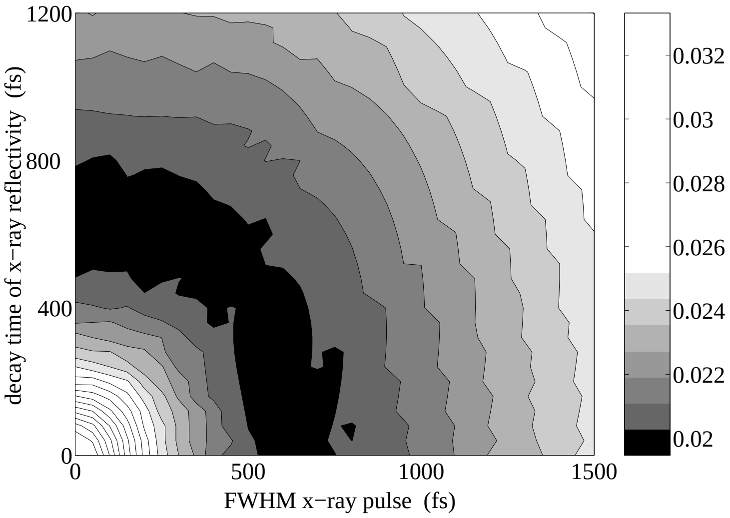

Figure 5.6: Quadratic deviation of theoretical correlations from the experimental data in Fig. 5.5. The theoretical values are the convolution of a Gaussian x-ray pulse with a linearly decaying x-ray reflectivity ('decay time' = 90% to 10%). (From Feurer et al. [31].)

δ-like x-ray pulse (FWHM = 0 fs) or an instantaneous disordering of the crystal (decay time = 0 fs). The latter assumption attributes the whole change of the observed Kα signal to the time structure of the x-ray burst and implies a halfwidth of the pulse of 640 ± 50 fs. Between the two extremes a range of other combinations are also possible which cover the Kα halfwidth of 180 fs predicted by the simulation model in combination with decay times between 500 fs and 800 fs. These decay times are physically reasonable. Numerical modelling [2] predicts a decay time of 480 fs assuming the same atomic displacement velocity for the irradiated CdTe as in GaAs [31].

Experiments which probe the structural change of laser-pumped crystals with Kα pulses from laser-produced plasmas also give an upper limit for the duration of the x-ray pulse in the experiment. In several of these experiments the Kα generating laser pulse had an intensity of 10^{16} – 10^{18} W/cm^2 and a halfwidth of 120 fs, the target materials were Si and Ti (Table 5.1). For these conditions the calculations predict pulse durations of several hundred femtoseconds (Fig. 5.4) — in agreement with the experiments. Sokolowski-Tinten et al. [86] estimate the upper limit of the duration of their Ti Kα bursts with $\tau_x \leq 300$ fs. For Si Kα pulses time constants of the measured signal $\tau_x + \tau_{decay} = 600$ fs [70] and 350 fs [77] were found.[8]

---

[8] Rischel et al. [70] used Langmuir-Blodgett-multilayers while Rousse et al. [77] worked with an InSb

Target	τ_l (fs)	I_l (W/cm^2)	τ_x (fs)	Method	Reference
Si	80	1×10^{17}	$200 - 640$	pump-probe	Feurer et al. [31]
Si	130	—	< 600	pump-probe	Rischel et al. [70]
Si	120	—	< 350	pump-probe	Rousse et al. [77]
Ti	120	—	≤ 300	pump-probe	S.-T. et al. [86]
Al	130	5×10^{17}	3300 ± 500	streak camera	Andiel et al. [4]
Al	400	1×10^{18}	$1500 - 2300$	streak camera	Kieffer et al. [50]
V	”	”	3000	”	”
Cu	42	$(0.3–2) \times 10^{17}$	6100	streak camera	Yoshida et al. [100]

Table 5.1: Experimentally observed Kα pulse durations τ_x from bulk targets. I_l and τ_l are the intensity and the duration of the plasma-creating laser pulse.

Beside the good agreement of the pump-probe experiments with the simulations concerning the effective pulse duration, some of them contradict the simulated pulse structure. In the preceding section it was discussed that the Kα emission is expected to have a long lasting tail of weak intensity for higher laser intensities. The numerical calculations predict such a weak tail also for the Kα pulses in the discussed experiments. In a cross-correlation measurement the ‘x-ray switch’ excludes a fraction of the last part of the Kα pulse from reaching the detector. The sign of the delay time is usually so defined that with increasing Δt an increasing part from the end of the pulse is excluded. When the delay time becomes so great that the end of the main Kα peak is reflected at a disturbed crystal a steep drop of the experimental Kα signal occurs. This delay time is usually defined as ‘$\Delta t = 0$’ (Fig. 5.5). Thus, when the Kα emission has a weak tail, this emission already hits a disturbed crystal for $\Delta t < 0$, so that for negative delay times a slow decrease of the detector signal is expected, as the solid line in Fig. 5.5 shows. This slow decrease was not found in any pump-probe experiment but only the data given by Rousse et al. [77] and Sokolowski-Tinten et al. [86] exclude its existence. This might be due to lower laser intensities in the experiments which give shorter afterglow emission. Anyway, an ex-

---

film as the pumped material.

perimental investigation dedicated to the structural details of the Kα pulse shape remains desirable.

In contrast to the good agreement between the calculated pulse durations and those from pump-probe experiments all streak camera measurements so far available gave much longer Kα pulse durations of several picoseconds (Table 5.1). In a streak camera photoelectrons generated by the x-ray pulse are swept across the detection screen by a time dependent electric field. The time resolution of the cameras in the experiments given in Table 5.1 were between 0.9 and 2 ps. Thus, all measured Kα pulse durations, except for the lowest value given by Kieffer et al. [50], are well above the time resolution in the corresponding experiment.

5.3 Achieving 100 fs Pulses

As was shown in Section 5.1, it will be difficult to generate efficient 100 fs Kα pulses from bulk targets. To achieve such a pulse duration foil targets can be used, which are quickly traversed by the higher energetic electrons, limiting the time they can produce x rays. On the other hand, using a thin foil target cuts off the last part of the Kα emission which does not only give the desired reduction in pulse duration but also reduces the yield of the x-ray source (Fig. 5.7). Analysing the relations between foil thickness, electron energy, emission time and Kα yield, results in design formulas to make efficient Kα bursts of a desired duration [69].

To calculate the optimal foil thickness and laser intensity needed we first look for the electron energy E_{max} which gives maximum Kα emission for a given afterglow duration τ_a. τ_a is the difference of the desired x-ray pulse duration τ_x and the laser pulse duration τ_l:

$$\tau_a \approx \tau_x - \tau_l. \tag{5.3}$$

Subsequently we assume that, as in the bulk case, the *optimal* laser intensity generates a hot electron temperature equal to E_{max}.

The number of photons which an electron can produce depends on the time it spends inside the target. Fig. 5.7 illustrates the situation for monoenergetic electrons impinging on Cu foils of different thicknesses. With increasing incidence energy, the excursion time in the foil initially increases, since faster electrons need more scattering events to lose

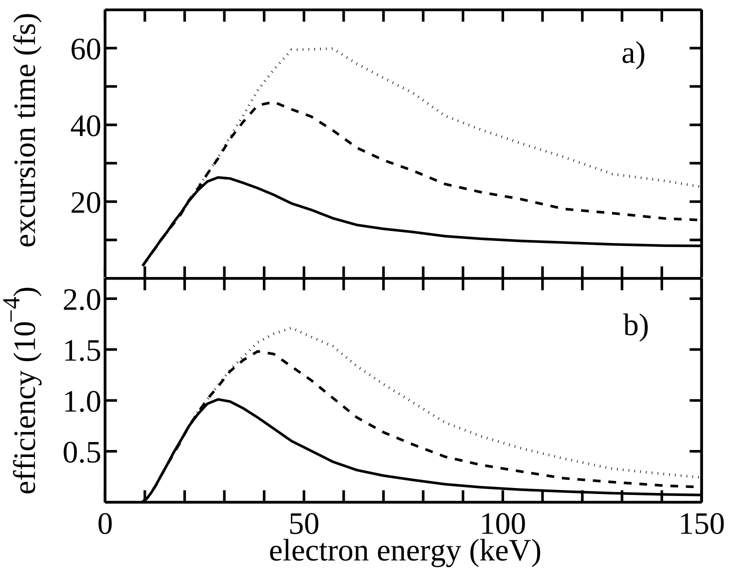

Figure 5.7: Scattering of monoenergetic electron beams in Cu foils of different thicknesses: 1 μm (solid), 2 μm (dashed), 3 μm (dotted). a) Mean time that the electrons spend inside the foil. b) Conversion efficiency of incidence electron energy into energy of observed Kα photons.

their energy. When the electrons are energetic enough to traverse the foil, the *mean* time spent inside the target decreases again with increasing energy. Thus, there is an optimal electron energy E_{max} which gives maximum mean excursion time inside the target τ_{max}, and therefore maximum number of Kα photons per incidence electron energy. With increasing target thickness both the mean excursion time and the number of generated Kα photons increase.

To determine how E_{max} and τ_{max} depend on target material and target thickness l, numerical simulations using monoenergetic electrons were performed for foil targets with a thickness between 1 and 5 μm and target elements from Ti ($Z = 22$) to Ta ($Z = 73$). The results were fitted by

$$E_{max} \approx 1.1\ Z^{0.95}\, l^{0.5}, \tag{5.4}$$

$$\tau_{max} \approx 100\ Z^{-0.4}\, l^{0.8}, \tag{5.5}$$

where the units are fs, μm and keV. The electrons with $E = E_{max}$ give an afterglow emission with duration $\tau_a \sim \tau_{max}$.

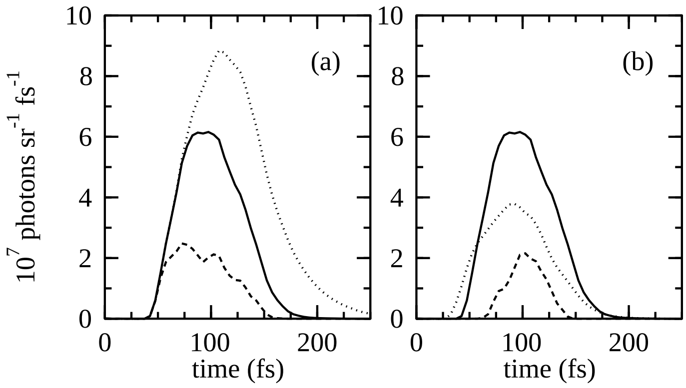

Figure 5.8: Kα emission from Cu foils: (a) Irradiated at $I = 7 \times 10^{15}$ W/cm^2, for thicknesses: 0.5 μm (dashed), 1.7 μm (solid), and 5 μm (dotted). (b) For constant thickness: 1.7 μm, irradiated 10^{15} W/cm^2 (dashed), 7×10^{15} W/cm^2 (solid), and 3×10^{16} W/cm^2 (dotted).

From Eq. (5.5) follows an optimal foil thickness for a given τ_a

$$l = 0.0032\ Z^{0.5}\ (\tau_x - \tau_l)^{1.25}. \tag{5.6}$$

Inserting (5.6) into (5.4) gives the desired energy of the electrons, which in turn is inserted into Eq. (3.4) to give the optimal laser intensity for the desired Kα pulse duration

$$I_{opt} = 2.3 \times 10^{11}\ Z^{2.4}\, (\tau_x - \tau_l)^{1.25} \quad \mathrm{W/cm}^2. \tag{5.7}$$

Table 5.2 gives an overview over the parameters predicted by (5.6) and (5.7) for a desired x-ray pulse duration of 100 fs, taking into account a 60 fs-laser pulse.

Simulations using realistic hot electron distributions from the PIC code together with parameters calculated from Eqs. (5.6) and (5.7), yield 90%-pulse durations a little lower than 100 fs (Table 5.2). With increasing foil thickness, both the Kα yield and the pulse duration increase, though the duration does not depend critcally on the thickness (Fig. 5.8,a). For the foil thickness giving just a pulse duration of 100 fs, the Kα yield does in fact show a distinct maximum at the calculated laser intensity. Again the pulse duration increases only slowly with increasing laser intensity (Fig. 5.8,b). The combination of fewer scattering events in foil targets and the reduced optimal laser intensity, producing fewer electrons with $U > 1$, implies a loss in Kα yield compared to bulk targets of a factor of ~ 2 for Ti and up to ~ 15 for Ta.

Element	Z	l (μm)	I_{opt} (W/cm^2)	τ_x (fs)	yield (photons / sr)
Ti	22	1.5	4×10^{15}	90	1.3×10^9
Cu	29	1.7	7×10^{15}	90	1.3×10^9
Ag	47	2.2	3×10^{16}	95	1.5×10^8
Ta	73	2.8	7×10^{16}	95	1.8×10^7

Table 5.2: Parameters of foil targets for the generation of 100 fs Kα pulses: foil thickness l and laser intensity I_{opt} according to Eqs.(5.6) and (5.7), simulated Kα pulse duration τ_x (first 90% of emission) and Kα yield for calculated l and I_{opt}.

The MC simulations show that under these conditions more than 30% of the hot electrons pass through the target, implying the creation of a space charge, which would cause a considerable number of electrons to return into the target and produce radiation again. This effect can be reduced by a second massive layer of conducting material behind the Kα producing foil to supply a return current, compensating the current of the impinging hot electrons and thus keeping the foil electrically neutral. Simulations using carbon as the ‘neutralizing material’ show that this target design stretches the 90%-pulse duration to 95 fs for Ti and 140 fs for Ta due to electrons backscattered from the carbon layer.

Summary

In the present thesis three features of femtosecond laser-plasma sources for Kα radiation were studied: the total Kα yield of the source, the source size and the pulse duration — using a newly developed numerical simulation model and by taking two-dimensional images of the Kα emission from two target sides.

For the numerical studies, a new Monte Carlo simulation code for the scattering of an electron beam in a solid and the generation of Kα radiation during this process was developed. The code allows the temporal development and the spatial distribution of the Kα emission from any target side to be simulated for the first time. It was combined with an existing $1\frac{1}{2}$D Particle-In-Cell code for the simulation of the laser-plasma interaction, which delivered the energy and time distribution of the accelerated plasma electrons.

Experimentally, two-dimensional magnified images of the Kα emission from Ti targets were taken with toroidally bent Si(311) crystals as the imaging optics. The influence of aberrations for the experimental conditions (magnification: 7, resolution: 6 μm, azimuth angle: 0.9°) was studied at an x-ray tube, at the plasma source and via ray-tracing. It was found that a sharp edge of the x-ray source is broadened to ~ 10 μm in the image. A Gaussian Kα source experiences a broadening in the direction of the dispersion plane which depends on its size while its halfwidth in the perpendicular direction is preserved. A halfwidth of the Kα emission of a few tens of microns in the direction of the dispersion plane cannot be resolved by the imaging anymore because the apparent extension in that direction is mainly due to aberrations.

The temporal structure of the laser pulse was measured with a third-order multishot autocorrelator and the two-dimensional beam profile was determined with a dynamic range of 10^3. Together with the knowledge of the imaging properties of the crystals, these data made it possible to calculate Kα images for parameters close to the experimental conditions.

The experimental observation that the Kα yield is maximal for a defocused laser, i.e. a laser intensity lower than the maximum achievable one, was reproduced by the simulations. An analytical model of the Kα yield was derived, which showed that the existence of an optimal laser intensity is due to the reabsorption of Kα photons inside the target. With increasing laser intensity the hot electrons penetrate deeper into the target and the portion of generated Kα photons which reaches the target surface and is emitted

decreases. This fraction shows a universal behaviour with respect to the incident electron energy normalised to the K-shell ionization energy of the target, E_K, implying a universal optimal hot electron temperature for energy conversion from hot electrons into emitted Kα radiation: $kT_{opt} = 6.4\,E_K$. From that, a surprisingly simple scaling of the optimal laser intensity with the atomic number of the target element results, namely: $I_{opt} \propto Z^{4.4}$ [69].

At best focus ($I \approx 7 \times 10^{18}$ W/cm^2) the measured vertical halfwidth of the Kα emission is ~ 70 μm — a factor of 28 larger than the vertical halfwidth of the laser focus. By electron scattering in the solid only a broadening by a factor $\lesssim 2$ can be explained. Around the main peak a weak Kα halo with a diameter of 400 μm occurs. More than half of the Kα emission originates from this halo. When the laser is defocused the halfwidth of the emission remains relatively constant, even for defocus distances up to 1 mm. When the laser is stronger focused an increase of the peak Kα emission is expected from the simulation model. Instead, the measured peak emission remains roughly constant and even decreases by a factor of ~ 2 close to the best focus. At the same time, the total Kα yield, which is well described by the numerical model for larger defocus distances, is 60% higher than simulated.

An estimate of self-induced fields in the experiment suggests that at the highest laser intensity, the intrinsic prepulses of the laser system generate a magnetic field which reflects a large portion of the hot electrons, which then are partly spread over a wide area by the ponderomotive field of the main pulse and further magnetic fields. These effects offer a qualitative explanation for the spatial characteristics of the Kα emission found in the experiment.

The penetration depth of the hot electrons into the target was concluded from the Kα emission from the target side. In contrast to the measurements of the emission from the target frontside, no deviations from the predictions by the numerical model could be verified. This might be due to the fact that the laser had to be focused close to the target edge to have an optically thin target, possibly resulting in a reduction of self-induced fields.

In a numerical study the temporal shape of the Kα emission was investigated. At laser intensities below 10^{16} W/cm^2 the pulse duration is determined by the thermalisation of the hot electrons. At higher laser intensities the hot electrons penetrate deeper and reabsorption of generated Kα photons limits the effective pulse duration. Then, the halfwidth of the Kα emission from target elements from Si to Cu, irradiated by a 60 fs laser pulse, is in the range of 100 – 180 fs. Due to the long stopping times of the hottest electrons, the first 90% of the emission occur on a longer time scale of several hundreds of femtoseconds to several picoseconds. The estimate of self-induced fields mentioned above suggests a prolongation of the Kα pulse of less than 100 fs due to complex electron orbits in the fields and a prolongation of less than 1 ps due to ballistic trajectories spreading escaping electrons over a surface area of the measured size.

The calculated halfwidths of the Kα pulses agree well with those found in cross-correlation measurements, but are significantly shorter than the picosecond durations from streak camera experiments. The measured decrease of the Kα signal found by another group at Jena University in a cross-correlation experiment is well reproduced by the simulations [31].

Because the study of the Kα emission from bulk targets revealed that it will be difficult to generate efficient 100 fs pulses from such targets, except for the lightest elements, foil targets were investigated, which are quickly traversed by the hottest electrons. Design formulas were developed which give the optimal combination of foil thickness and laser intensity for making high yield Kα pulses with a selectable duration [69]. Taking into account the recent advances in laser technology making available high-intensity femtosecond lasers with high repetition rates it appears realistic that laser-plasma Kα sources with high flux and pulse durations $\leq$ 100 fs will be available within the near future.

Bibliography

[1] Alaterre, P. et al. (1984). *Opt. Commun.* **49**, 140.

[2] Allen, R. E. et al. (2001). *Proc. SPIE* **4280**, 123.

[3] Anderson, E. et al. (2001). *J. Appl. Phys.* **90**, 3048–3056.

[4] Andiel, U. et al. (2002). *Appl. Phys. Lett.* **80**, 198–200.

[5] Bastiani, S. et al. (1997). *Phys. Rev. E* **56**, 7179–7185.

[6] Beg, F. N. et al. (1997). *Phys. Plasmas* **4**, 447.

[7] Bell, A. R. et al. (1993). *Phys. Rev. E* **48**, 2087–2093.

[8] Bell, A. R. et al. (1997). *Plasma Phys. Control. Fusion* **39**, 653–659.

[9] Berger, M. J. and Seltzer, S. M. (1964). *Nuclear Science Series Report* **39**, 205–268.

[10] Birdsall, C. and Langdon, A. (1985). Plasma Physics via Computer Simulation. McGraw-Hill, New York.

[11] Bonnaud, G. (1986). Description du code particulaire 1d 1/2 euterpe. Technical report, Commissariat a l'Energie Atomique.

[12] Borghesi, M. et al. (1998). *Phys. Rev. Lett.* **80**, 5137–5140.

[13] Brunel, F. (1987). *Phys. Rev. Lett.* **59**, 52–55.

[14] Brunel, F. (1988). *Phys. Fluids* **31**, 2714–2719.

[15] Casnati, E. et al. (1982). *J. Phys. B* **15**, 155–167.

[16] Chen, H. et al. (1993). *Phys. Rev. Lett.* **70**, 3431–3434.

[17] Christiansen, J. P. et al. (1974). *Computer Phys. Comm.* **7**, 271–287.

[18] Chukhovskii, F. N. et al. (2000). *Laser Part. Beams* **18**, 49–57.

[19] Clark, E. L. et al. (2000). *Phys. Rev. Lett.* **85**, 1654–1657.

[20] Crow, J. E. (1975). *J. Plasma Physics* **14**, 65–76.

[21] Dick, C. E. et al. (1973). *J. Appl. Phys.* **44**, 815–826.

[22] Dirksmöller, M. (1996). Einzel- und Doppelkristallanordnungen zur hochauflösenden röntgenoptischen Abbildung. Ph.D. thesis, Friedrich Schiller Universität Jena.

[23] Dirksmöller, M. et al. (1995). *Optics Comm.* **118**, 379–387.

[24] Djaoui, A. (). A user guide fro the laser-plasma simulation code: MED103. Central Laser Facility, Rutherford Appleton Laboratory.

[25] Eder, D. C. et al. (2000). *Appl. Phys. B* **70**, 211–217.

[26] Estabrook, K. and Kruer, W. L. (1978). *Phys. Rev. Lett.* **40**, 42–45.

[27] Everhart, T. E. and Hoff, P. H. (1971). *J. Appl. Phys.* **42**, 5837–5846.

[28] Fabbro, R. and Mora, P. (1982). *Phys. Lett.* **90A**, 48–50.

[29] Feurer, T. et al. (1999). In Applications of high field and short wavelength sources VIII, pp. 108–110. OSA, Washington DC.

[30] Feurer, T. et al. (2001). *Appl. Phys. B* **72**, 15–20.

[31] Feurer, T. et al. (2002). *Phys. Rev. E* **65**, 016412.

[32] Forslund, D. W. and Brackbill, J. U. (1982). *Phys. Rev. Lett.* **48**, 1614–1616.

[33] Förster, E. et al. (1991). *Laser Part. Beams* **9**, 135–148.

[34] Franzen, S. et al. (1995). *Biochemistry* **34**, 1224–1237.

[35] Gai, F. et al. (1998). *Science* **279**, 1886–1891.

[36] Gibbon, P. and Bell, A. R. (1992). *Phys. Rev. Lett.* **68**, 1535–1538.

[37] Gibbon, P. and Förster, E. (1996). *Plasma Phys. Control. Fusion* **38**, 769–793.

[38] Gibbon, P. et al. (1999). *Phys. Plasmas* **6**, 947–953.

[39] Green, M. and Cosslett, V. (1968). *J. Phys. D* **1**, 425–436.

[40] Gremillet, L. et al. (1999). *Phys. Rev. Lett.* **83**, 5015–5018.

[41] Guo, T. et al. (2001). *Rev. Sci. Instrum.* **72**, 41–47.

[42] Haines, M. G. (1997). *Phys. Rev. Lett.* **78**, 254–257.

[43] Halbleib, J. A. and Mehlhorn, T. A. (1986). *Nucl. Sci. Eng.* **92**, 338.

[44] Harrach, R. J. and Kidder, R. E. (1981). *Phys. Rev. A* **23**, 887–896.

[45] Hockney, R. and Eastwood, J. (1981). Computer Simulation Using Particles. McGraw-Hill, New York.

[46] Hombourger, C. (1998). *J. Phys. B: At. Mol. Opt. Phys.* **31**, 3693–3702.

[47] Jiang, Z. et al. (1995). *Phys. Plasmas* **2**, 1702–1711.

[48] Joy, D. C. (1995). Monte Carlo Modeling for Electron Microscopy and Microanalysis. Oxford Univ. Press, Oxford.

[49] Kanaya, K. and Okayama, S. (1972). *J. Phys. D: Appl. Phys.* **5**, 43–58.

[50] Kieffer, J. et al. (1996). *J. Opt. Soc. Am B* **13**, 132–137.

[51] Kruer, W. L. (1988). The Physics of Laser Plasma Interactions. Addison-Wesley, New York.

[52] Larsson, J. (2001). *Meas. Sci. Technol.* **12**, 1835–1840.

[53] Li, Y. T. et al. (2001). *Phys. Rev. E* **66**, 046407.

[54] Malka, G. et al. (1997). *Phys. Rev. Lett.* **79**, 2053–2056.

[55] Mason, R. J. and Tabak, M. (1998). *Phys. Rev. Lett.* **80**, 524–527.

[56] McCall, G. H. (1982). *J. Phys. D: Appl. Phys.* **15**, 823–831.

[57] Missalla, T. et al. (1999). *Rev. Sci. Instrum.* **70**, 1288–1299.

[58] Moore, C. I. et al. (1997). *Phys. Rev. Lett.* **79**, 3909–3912.

[59] Mora, P. and T. M. Antonsen, J. (1996). *Phys. Rev. E* **53**, R2068–R2071.

[60] Morak, A. et al. (2002). *Appl. Phys. B* Submitted.

[61] Murnane, M. M. et al. (1991). *Science* **251**, 531–536.

[62] NIST (1996). Tables of x-ray mass attenuation coefficients and mass energy-absorption coefficients. Technical report, National Insitute of Standards and Technology, http://physics.nist.gov/PhysRefData/XrayMassCoef/cover.html.

[63] Norreys, P. A. et al. (1996). *Phys. Rev. Lett.* **76**, 1832–1835.

[64] Perman, B. et al. (1998). *Science* **279**, 1946–1950.

[65] Pisani, F. et al. (2000). *Phys. Rev. E* **62**, 5927–5930.

[66] Pretzler, G. et al. (2000). *Phys. Rev. E* **62**, 5618–5623.

[67] Pukhov, A. and Meyer-ter-Vehn, J. (1997). *Phys. Rev. Lett.* **79**, 2686–2689.

[68] Raven, A. et al. (1978). *Phys. Rev. Lett.* **41**, 554–557.

[69] Reich, C. et al. (2000). *Phys. Rev. Lett.* **84**, 4846–4849.

[70] Rischel, C. et al. (1997). *Nature* **390**, 490–492.

[71] Röntgen, W. C. (1898). *Ann. d. Phys. u. Chem.* **N. F. 64**, 1–37.

[72] Rosen, M. D. (1990). In E. M. Campbell, editor, Femtosecond to Nanosecond High-Intensity Lasers and Applications, volume 1229, pp. 160–170.

[73] Rousse, A. (1994). Géneration d'électrons rapides et émission X dans l'interaction d'une impusion laser sub-picoseonde et intense avec une cible solide. Ph.D. thesis, Université Paris XI Orsay.

[74] Rousse, A. et al. (1994). *Phys. Rev. E* **50**, 2200–2207.

[75] Rousse, A. et al. (1994). *J. Phys. B: At. Mol. Phys.* **27**, L697–L701.

[76] Rousse, A. et al. (2001). *Rev. Mod. Phys.* **73**, 17–31.

[77] Rousse, A. et al. (2001). *Nature* **410**, 65–68.

[78] Salvat, F. and Parellada, J. (1984). *J. Phys. D: Appl. Phys.* **17**, 1545–1561.

[79] Schlegel, T. et al. (1999). *Phys. Rev. E* **60**, 2209–2217.

[80] Schwoerer, H. et al. (2001). *Phys. Rev. Lett.* **86**, 2317–2320.

[81] Seltzer, S. M. (1991). *Appl. Radiat. Isot.* **42**, 917.

[82] Sentoku, Y. et al. (1999). *Phys. Plasmas* **6**, 2855–2861.

[83] Sheng, Z.-M. et al. (2000). *Phys. Rev. Lett.* **85**, 5340–5243.

[84] Sokoloff, J. P. et al. (1988). *Phys. Rev. B* **38**, 597–605.

[85] Sokolowski-Tinten, K. et al. (1995). *Phys. Rev. B* **51**, 14186–14198.

[86] Sokolowski-Tinten, K. et al. (2001). *Phys. Rev. Lett.* **87**, 225701.

[87] Soom, B. et al. (1993). *J. Appl. Phys.* **74**, 5372–5377.

[88] Stamper, J. A. et al. (1971). *Phys. Rev. Lett* **26**, 1012–1015.

[89] Stampfli, P. and Bennemann, K. H. (1994). *Phys. Rev. B* **49**, 7299–7305.

[90] Strickland, D. and Mourou, G. (1985). *Opt. Comm.* **56**, 219–221.

[91] Sudan, R. (1993). *Phys. Rev. Lett* **70**, 3075–3078.

[92] Teubner, U. et al. (1996). *Phys. Rev. E* **54**, 4167–4177.

[93] Uschmann, I. et al. (1999). *Laser and Part. Beams* **17**, 671–680.

[94] Šrajer, V. et al. (1996). *Science* **274**, 1726.

[95] Wagner, R. et al. (1997). *Phys. Rev. Lett.* **78**, 3125–3128.

[96] Wallace, J. M. (1985). *Phys. Rev. Lett.* **55**, 707–710.

[97] Wharton, K. et al. (2001). *Phys. Rev. E* **64**.

[98] Wharton, K. B. et al. (1998). *Phys. Rev. Lett.* **81**, 822–825.

[99] Wilks, S. C. et al. (1992). *Phys. Rev. Lett.* **69**, 1383–1386.

[100] Yoshida, M. et al. (1998). *Phys. Plasmas* **73**, 2393–2395.

[101] Yu, J. et al. (1999). *Phys. Plasmas* **6**, 1318–1322.

[102] Zhidkov, A. G. et al. (2001). *Phys. Plasmas* **8**, 3718–3723.

[103] Ziener, C. et al. (2002). *Phys. Rev. E* **65**, 066411.

[104] Zschornack, G. (1989). Atomdaten für die Röntgenspektralanalyse. Deutscher Verlag für Grundstoffindustrie, Leipzig.

Appendix A

Cross Section for K-Shell Ionization

The electron cross section for the ionisation of the K shell, σ_K, was taken from Casnati et al. [15]:

$$\sigma_K = n_K\, a_0^2\, R \left(\frac{E_0}{E_K}\right)^2 \Phi\, \varphi\, \frac{\ln U}{U}, \tag{A.1}$$

with

$$R = \frac{1+2J}{U+2J}\,\frac{U+J}{1+J}\,\frac{(1+U)(U+2J)(1+J)^2}{J^2(1+2J)+U(U+2)(1+J)^2}, \tag{A.2}$$

$$\Phi = \left(\frac{E_K}{E_0}\right)^{-0.0318+0.3160/U-0.1135/U^2}, \tag{A.3}$$

$$\varphi = 10.57\ \exp\left(-\frac{1.736}{U}+\frac{0.317}{U^2}\right). \tag{A.4}$$

$n_k = 2$ is the number of electrons in the K shell, and $a_0 = 5.292 \cdot 10^{-11}$ m is the first Bohr radius. R is the relativstic correction with the kinetic energy of the electron U and its rest energy J being normalised to the ionisation energy of the K-shell E_K:

$$U = \frac{E}{E_K}, \tag{A.5}$$

$$J = \frac{mc^2}{E_K}. \tag{A.6}$$

The ionisation energy is related to the Rydberg energy $E_0 = 0.013606$ keV by

$$\begin{aligned} E_K &= 0.4240\, E_0\, Z^{2.1822} \\ &= 0.0057918\, Z^{2.1822} \quad \text{keV}. \end{aligned} \tag{A.7}$$

Appendix B

Bethe Stopping Power

The energy loss of an electron per unit pathlength dE/ds was calculated according to Bethe's stopping power theory, using the formulation by Berger and Seltzer [9]:

$$-\frac{dE}{ds} = \frac{2\pi r_0^2 mc^2}{\beta^2}\,\frac{N_A \rho}{A}\,Z\left\{\ln\left[\frac{\tau^2(\tau+2)}{2(J/mc^2)^2}\right] + F(\tau)\right\}, \tag{B.1}$$

$$F(\tau) = 1-\beta^2+\frac{\tau^2/8-(2\tau+1)\ln(2)}{(\tau+1)^2}\,. \tag{B.2}$$

The symbols have the following meanings:

Electron properties:

mc^2 : rest energy = 510.976 keV

τ : kinetic energy in units of mc^2

β : $\sqrt{\tau(\tau+2)}/(\tau+1) = velocity/c$

Properties of the medium:

Z : atomic number

A : atomic weight

ρ : mass density

J : mean excitation potential

Other parameters:

N_A : Avogadro's number = 6.02486×10^{23} mole^{-1}

r_0^2 : $(e^2/mc^2)^2 = 7.94030 \times 10^{-26}$ cm^2

The mean excitation potential J is given by the empirical relation

$$J = (\,9.76\,Z + 58.8\,Z^{-0.19}\,)\,\mathrm{eV}. \tag{B.3}$$

Appendix C

Calculating Mean Values for Compound Targets

The mean atomic density $\langle n_A \rangle$ of a compound is given by

$$\langle n_A \rangle = \frac{\rho_C \, N_A}{\sum f_i \, m_i} \, , \tag{C.1}$$

where ρ_C is the mass density of the compound, m_i are the atomic masses of its constituents i and f_i are their stoichiometric fractions in the compound. N_A is Avogadro's number. The mean atomic number $\langle Z \rangle$ is

$$\begin{aligned} \langle Z \rangle &= \sum \frac{n_i}{\langle n_A \rangle} \, Z_i \\ &= \sum f_i \, Z_i, \end{aligned} \tag{C.2}$$

where n_i are the atomic densities of the constituents in the compound. $n_i / \langle n_A \rangle$ is given by the stoichiometric fraction f_i. The mean ionization potential J of the compound is derived via

$$\begin{aligned} \ln\langle J \rangle &= \frac{1}{\langle Z \rangle} \sum \frac{n_i}{\langle n_A \rangle} \, Z_i \ln J_i \\ &= \frac{1}{\langle Z \rangle} \sum f_i \, Z_i \ln J_i, \end{aligned} \tag{C.3}$$

and its absorption coefficient $\langle \mu \rangle$ for own Kα radiation is

$$\langle \mu_{abs} \rangle = \frac{\sum f_i \, m_i \, \mu_i}{\sum f_i \, m_i}. \tag{C.4}$$

Danksagung

Ich möchte mich bei allen bedanken, ohne deren Beiträge diese Arbeit nicht entstanden wäre. Insbesondere gilt mein Dank:

Prof. Eckhart Förster für die interessante Themenstellung und die Betreuung der Arbeit. Sodann Prof. Roland Sauerbrey für die Möglichkeit, die Experimente im Laserlabor des IOQ durchzuführen.

Paul Gibbon dafür, daß er sich jederzeit in Diskussionen verwickeln ließ, die stets in gute Ideen mündeten, Ingo Uschmann für die praktische Unterstützung bei den Abbildungsexperimenten und beiden zusammen für ihre zahlreichen Verbesserungsvorschläge zum Manuskript.

Ortrud Wehrhan für ihr Engagement bei der Beschaffung scharfkantiger Titantargets und für ihren Optimismus. Wolfgang Becker für das Herstellen der Kontakte zum Materiallabor an der Humboldt-Uni und Adelheid Saupe für ihre Bemühungen bei der Targetpräparation.

Thomas Haertling für seine engagierte Teilnahme am nächtelangen Aufbau des Experiments, Friederike Ewald und Stefan Düsterer für die kleinen Laserfokii und ihre Vermessung, sowie Laszlo Veisz für die Unterstützung beim Gebrauch des Medusa-Simulationscodes.

Schließlich Gerd Wedler, Andrea Lübcke und Andreas Morak für die kritische Durchsicht von Teilen des Manuskripts und die daraus entstandenen Anregungen.

Und natürlich allen anderen Mitarbeitern des Instituts für die zahllosen Hilfen in Detailfragen und für die angenehme und produktive Atmosphäre, in der diese Arbeit entstanden ist.

Curriculum Vitae

Name: Christian Reich
Date and place of birth: 22nd April, 1968, Berlin
Citizenship: german
Marital Status: single
Address: Ernst-Haeckel-Platz 1
07745 Jena

School education

1974 - 1980	Johannes Tews Grundschule, Berlin
1980 - 1987	Werner von Siemens Gymnasium, Berlin

University education

1987 - 1990	Electrical engineering, Technische Universität Berlin September 1989: Vordiplom
1990 - 1992	Physics, Technische Universität Berlin February 1992: Vordiplom
1992	Erasmus-fellowship at Rijksuniversiteit Groningen (NL)
1992 - 1996	Physics, Freie Universität Berlin December 1996: Diplom

Employment

1989/1990	Cataloguing of the technical equipment of the Hahn-Meitner-Institut, Berlin
1997	Wissenschaftlicher Mitarbeiter (research assistent) at the physics department of the FU Berlin
1997 - 1998	Wissenschaftlicher Mitarbeiter in the DFG-programme "Bewegungssysteme" (locomotion systems) at the biology department of the Friedrich Schiller University Jena
since 1.1.1999	Ph.D. position at the Institute for Optics and Quantum Electronics of the FSU Jena in the DFG-programme "Wechselwirkung intensiver Laserfelder mit Materie" (interaction of intense laser fields with matter)

Ehrenwörtliche Erklärung

Ich erkläre hiermit ehrenwörtlich, daß ich die vorliegende Arbeit selbständig, ohne unzulässige Hilfe Dritter und ohne Benutzung anderer als der angegebenen Hilfsmittel und Literatur angefertigt habe. Die aus anderen Quellen direkt oder indirekt übernommenen Daten und Konzepte sind unter Angabe der Quelle gekennzeichnet.

Weitere Personen waren an der inhaltlich-materiellen Erstellung der Arbeit nicht beteiligt. Insbesondere habe ich nicht die Hilfe von Vermittlungs- bzw. von Beratungsdiensten (Promotionsberater oder andere Personen) in Anspruch genommen. Niemand hat von mir unmittelbar oder mittelbar geldwerte Leistungen erhalten, die im Zusammenhang mit dem Inhalt der vorgelegten Dissertation stehen.

Die Arbeit wurde bisher weder im In- noch im Ausland in gleicher oder ähnlicher Form einer anderen Prüfungsbehörde vorgelegt.

Die geltende Promotionsordnung der Physikalisch-Astronomischen Fakultät ist mir bekannt.

Ich versichere ehrenwörtlich, daß ich nach bestem Wissen die reine Wahrheit gesagt und nichts verschwiegen habe.

Jena, den 31. Januar 2003